Doctoral theses at NTNU, 2020:80

Ola Gjønnes Grendal

In situ X-ray diffraction studies during hydrothermal synthesis of ferroelectric materials

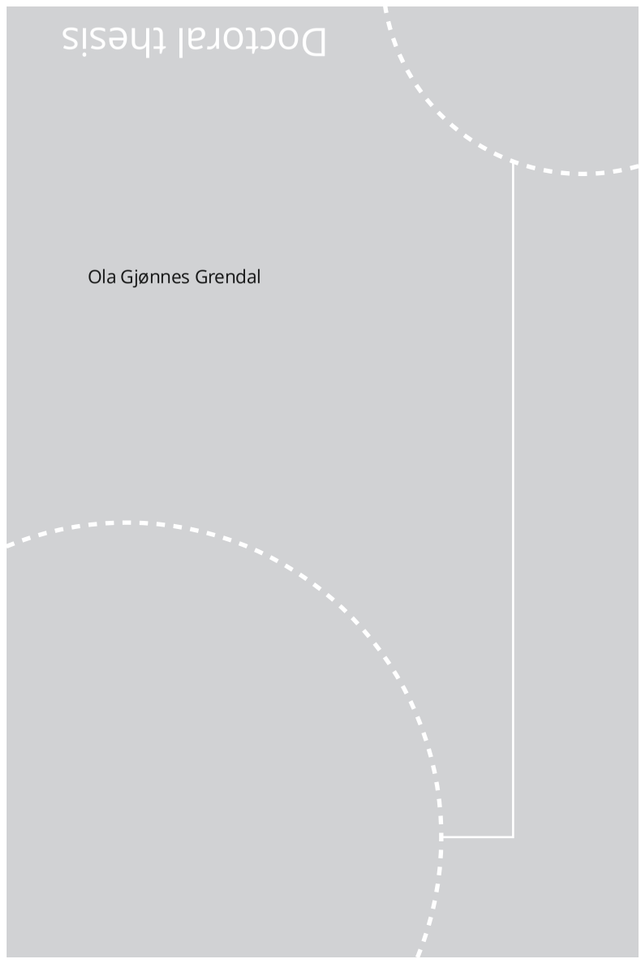

ISBN 978-82-326-4512-1 (printed ver.)
ISBN 978-82-326-4513-8 (electronic ver.)
ISSN 1503-8181

NTNU
Norwegian University of
Science and Technology

NTNU
Norwegian University of Science and Technology
Thesis for the Degree of
Philosophiae Doctor
Faculty of Natural Sciences
Department of Materials Science and Engineering

Doctoral theses at NTNU, 2020:80

NTNU

Ola Gjønnes Grendal

In situ X-ray diffraction studies during hydrothermal synthesis of ferroelectric materials

Thesis for the Degree of Philosophiae Doctor

Trondheim, March 2020

Norwegian University of Science and Technology
Faculty of Natural Sciences
Department of Materials Science and Engineering

NTNU
Norwegian University of
Science and Technology

NTNU
Norwegian University of Science and Technology

Thesis for the Degree of Philosophiae Doctor

Faculty of Natural Sciences
Department of Materials Science and Engineering

ISBN 978-82-326-4512-1 (printed ver.)
ISBN 978-82-326-4513-8 (electronic ver.)
ISSN 1503-8181

Doctoral theses at NTNU, 2020:80

Printed by NTNU Grafisk senter

Preface

This thesis has been submitted to the Norwegian University of Science and Technology (NTNU) in partial fulfillment of the requirement for the academic degree *Philosophiae Doctor*.

The doctoral studies were performed predominantly in the Functional Materials and Materials Chemistry Research Group (FACET) at the Department of Materials Science and Engineering (IMA) at NTNU in Trondheim under the supervision of Prof. Mari-Ann Einarsrud, Prof. Tor Grande and Prof. Sverre Magnus Selbach. This work has been funded by NTNU and the Research Council of Norway through the Toppforsk program "From aqueous solutions to oxide thin films and hierarchical structures" (grant number 250403). Seven months were spent at International Center for Materials Nanoarchitectonis (MANA) at National Institute for Materials Science (NIMS) in Tsukuba, Japan, under the supervision of Dr. Satoshi Tominaka. This was funded by International Cooperative Graduate Program scholarship, NIMS. The majority of the experimental data for this thesis has been collected at synchrotron facilities, namely the Swiss Norwegian Beamlines (SNBL, BM01) at the European Synchrotron Radiation Facility (ESRF) in Grenoble, France and beam line BL08W at the Super Photon ring-8 GeV (SPring-8) in Koto, Japan.

The work in this thesis has been published, or is ready for publishing. The author of this thesis has been the main contributor. This includes planning and performing the experiments, analysis and discussion of results and writing of the drafts. The exceptions are operation of the TEM, performed partly by Dr. Ragnhild Sæterli (Department of Physics, NTNU) and M.Sc. Inger-Emma Nylund (IMA, NTNU) and the determination of one of the secondary phases as a pyrochlore-type phase in the work on $Sr_xBa_{1-x}Nb_2O_6$, done by Dr. Anders Bank Blichfeld (IMA, NTNU). In addition, M.Sc. Inger-Emma Nylund calculated the relative tilt between two particles investigated by TEM based on the intensity profiles across the particles obtained by HAADF-STEM images.

Trondheim, January 2020

Ola Gjønnes Grendal

Papers and manuscripts included in this thesis

1. **Grendal, O.G.***, Blichfeld, A. B., Skjærvø, S. L., van Beek, W., Selbach, S. M., Grande, T., Einarsrud, M.-A., Facile low temperature hydrothermal synthesis of $BaTiO_3$ nanoparticles studied by *in situ* X-ray diffraction, *Crystals* **8**, 253-264 (2018).

   * Contributions: Carried out the experiments, analyzed the data and wrote the first draft of the manuscript.

2. **Grendal, O.G.***, Blichfeld, A. B., Vu, T. D., van Beek, W., Selbach, S. M., Grande, T., Einarsrud, M.-A., Composition and morphology tuning during hydrothermal synthesis of $Sr_xBa_{1-x}Nb_2O_6$ tetragonal tungsten bronzes studied by *in situ* X-ray diffraction, *CrystEngComm* **21**, 5922-5930 (2019).

   * Contributions: Carried out the experiments, analyzed the data and wrote the first draft of the manuscript. Participated on the preliminary TEM characterization, which was performed by Dr. Ragnhild Sæterli.

3. **Grendal, O.G.***, Nylund, I.-E., Blichfeld, A. B., Tominaka, S., Ohara, K., Selbach, S. M., Grande, T., Einarsrud, M.-A., Designed growth of $Sr_xBa_{1-x}Nb_2O_6$ hopper- and cube-shaped nanostructures by hydrothermal synthesis, submitted to *Chemistry: A European Journal* (January 2020).

   * Contributions: Carried out the experiments, analyzed the data and wrote the first draft of the manuscript. Participated on the TEM characterization, which was performed by M.Sc. Inger-Emma Nylund.

Papers and manuscripts omitted from this thesis

1. Dalod, A. R. M., **Grendal, O.G.***, Skjærvø, S. L., Inzani, K., Selbach, S. M., Henriksen, L., van Beek, W., Grande, T., Einarsrud, M.-A., Controlling oriented attachment and *in situ* functionalization of TiO_2 nanoparticles during hydrothermal synthesis with APTES, *J. Phys. Chem. C* **121**, 11897-11906 (2017).

   * Contributions: Performed the *in situ* X-ray experiments together with Dr. Antoine R. M. Dalod and Dr. Susanne L. Skjærvø, performed the *ex situ* autoclave synthesis and characterized the product with XRD, TGA, FTIR and nitrogen surface adsorption. Gave feedback on the drafted manuscript.

2. Dalod, A. R. M., **Grendal, O.G.***, Blichfeld, A. B., Furtula, V., Pérez, J., Henriksen, L., Grande, T., Einarsrud, M.-A., Structure and optical properties of titania-PDMS

hybrid nanocomposites prepared by *in situ* non-aqueous synthesis, *Nanomaterials* **7**, 460-475 (2017).

* Contributions: Performed the small angle X-ray scattering experiments together with Dr. Anders B. Blichfeld and Dr. Javier Pérez and gave feedback on the drafted manuscript.

3. Hongjun, L., **Grendal, O.G.***, Skjærvø, S. L., Dalod, A. R. M., van Beek, W., Einarsrud, M.-A., Muñoz-Rojas, D., Reaction mechanism of the hydrothermal synthesis of $AgCuO_2$ by *in situ* time-resolved X-ray diffraction, in review *Crystal Growth & Design* (2020).

   * Contributions: Performed the *in situ* X-ray diffraction experiments together with Dr. Hongjun Liu, performed the batch Rietveld analysis and gave feedback on the drafted manuscript.

4. Marshall, K. P., Blichfeld, A. B., Skjærvø, S. L., **Grendal, O.G.***, van Beek, W., Selbach, S. M., Grande, T., Einarsrud, M.-A., A fast, low temperature synthesis method for hexagonal $YMnO_3$: Kinetics, purity, size and shape as studied by *in situ* X-ray diffraction, submitted to *Chemistry: A European Journal* (January 2020).

   * Contributions: Performed the *in situ* X-ray diffraction experiments together with Dr. Kenny Marshall and gave feedback on the drafted manuscript.

5. Skjærvø, S. L., Ong, G., **Grendal, O.G.***, Høydalsvik, K. W., van Beek, W., Ohara, K., Grande, T., Satoshi, T., Milliron, D., Einarsrud, M.-A., Reaction scheme during hydrothermal synthesis of nanosized $NaNbO_3$, in manuscript (2020).

   * Contributions: Measured the X-ray total scattering on alkaline Nb_2O_5 slurries and gave feedback on the drafted manuscript.

Acknowledgments

Now, at the end of my PhD it is time to thank everyone that have supported me, and have made this journey so memorable and incredibly enjoyable.

First, I want to thank my supervisor Mari-Ann Einarsrud, it has been a pleasure working with you. Our un-spoken friendly competition of "not-it" have made our collaboration extremely efficient and streamlined. Your guidance and support have been invaluable throughout this project. I especially remember during our second beam time, where nothing was working and I was ready to quit everything. To my co-supervisors, Tor Grande and Sverre M. Selbach, thank you for your advices and inputs, which have always helped in lifting the quality of my work. I am incredibly grateful to Dr. Satoshi Tominaka for introducing me to X-ray total scattering and PDF analysis and of course for hosting me during my 7 months exchange at the National Institute for Materials Science in Tsukuba, Japan. I am also grateful for the opportunity to co-supervise two excellent master students, Frida Sveen Hempel and Viviann Hole. I learnt a lot from our collaborations.

I am grateful for have been part of the TOPPFORSK/FASTS project and its extended family. Special thanks goes to Anders Bank Blichfeld for his exceptional skills in both engineering and science and his relentless quest for improving the *status quo*. To Susanne Linn Skjærvø for paving the road for us coming after her. To Kristine Bakken for sharing the same struggles and challenges as me, and solving them together. To Inger-Emma Nylund for help and support with TEM experiments. I would also like to thank Antoine Dalod, I learnt a lot from our collaboration with you as my co-supervisor during my master thesis.

I have been part of the FACET family for almost 5 years, and I have encountered too many awesome people to mention them all with names. However, to all colleagues and friends, I would like to thank you for this amazing time, with long lunches discussing everything and nothing, social events, running and skiing. I am afraid I will never work in a place like this again!

During the last year of my PhD, I have been able to do more dissemination of my work to the general public than what is generally normal for someone in academia. This includes presenting all my research in only 4 min at Forsker Grand Prix 2019 and explaining piezoelectricity to 6 years old at Folkebiblioteket. I have learnt a lot from these experiences,

and my presentation and storytelling skills have significantly improved. I am thankful to Gunnar Kåre Hansen and Kjersti Kremmervik at the Communication Division at NTNU and Merete Røskaft at Det Kongelige Norske Videnskabers Selskab for trusting me with these opportunities.

In addition to the beam times directly linked to my own work, I have been fortunate enough to be included in other groups beam times, which have provide me a broader insight into the fantastic world of X-ray science. For this I am thankful to Dr. Katrien De Keukeleere (XANES and EXAFS at ESRF), Antoine Dalod (SAXS at SOLEIL), Prof. Bo Iversen and his group at Aarhus University (total scattering at PETRA III) and Dr. Satoshi Tominaka (total scattering at SPRING-8).

Finally, I would like to thank my parents and family, for their constant encouragement, support and interest in what I am doing, no matter what I have chosen to do.

Abstract

Combining the technologically important properties of ferroelectric materials with the interesting phenomena of nanosizing and nanostructuring is believed to lead to further development of non-volatile ferroelectric memories, energy harvesting devices and materials for bio-medical applications among others. Cheap, controllable and environmental-friendly synthesis routes, yielding high quality materials, are needed to meet the growing demand of nanosized and nanostructured ferroelectric materials. The wet chemical methods, and especially hydrothermal synthesis, is scoring high on several of these merits. Still, the hydrothermal method is limited to a trial-and-error process for controlling size, morphology and composition of the synthesized materials and the same is true for development of new synthesis routes. This follows from the limited fundamental understanding of the underlying mechanisms for nucleation and growth during hydrothermal synthesis. Thus, to fully utilize the hydrothermal method for synthesis of nanostructured ferroelectric materials, a better understanding of the synthesis method is needed.

In this work, extensive *in situ* synchrotron diffraction studies were utilized to reveal the formation mechanisms of nanosized and nanostructured ferroelectric materials in real-time during hydrothermal synthesis. Two materials were investigated, namely the perovskite $BaTiO_3$ (BT), and the tetragonal tungsten bronze $Sr_xBa_{1-x}Nb_2O_6$ (SBN).

The formation of BT was studied using two different titanium precursors, one amorphous $TiO_2{\cdot}xH_2O$ precipitate, and a soluble titanium citric acid complex. The *in situ* diffraction study combined with Rietveld refinement revealed a fast (~15 s) formation of nanocrystalline BT from the $TiO_2{\cdot}xH_2O$ precipitate. The reaction kinetics were observed to be independent of reaction temperature for the studied temperature range. Kinetics analysis, showed that BT formed from a dissolution precipitation mechanism limited by nucleation and growth (growth order $n = 2$) from the $TiO_2{\cdot}xH_2O$ precipitate. Nanocrystalline BT also formed by a dissolution precipitation mechanism using the titanium citric acid complex at high temperatures, and changed from a nucleation and growth mechanism to phase-boundary limited growth with decreasing temperature. Moreover, the effect of two surfactants, ethylene glycol and sodium dodecylbenzenesulfonate, were investigated and were found to decrease and increase the crystallite size using the $TiO_2{\cdot}xH_2O$ precursor,

respectively. The surfactants had no significant effect when using the titanium citric acid complex precursor.

A new synthesis route for SBN was developed and demonstrated. The formation of SBN was studied as a function of reaction temperature and Sr:Ba ratio in the precursor. The results show that the Sr-fraction in the final product can be tuned both by the Sr:Ba ratio in the precursor, and by changing the dielectric constant of the solvent. Furthermore, the growth mechanism can be controlled, and thus the final morphology, by changing the Sr:Ba ratio in the precursor and the reaction temperature. At low Sr-fractions and low temperatures, the particles grew by a hopper-growth mechanism, forming hollow-ended elongated particles. Increasing the Sr-fraction and/or reaction temperature yielded cube-shaped (~500 nm) or rod-shaped particles by a layer-by-layer growth mechanism. X-ray total scattering and pair distribution function (PDF) analysis revealed that the amorphous niobium precursors consist of Lindquist-like ions ($[Nb_6O_{19}]^{8-}$). With this insight, the changes in growth mechanism as a function of Sr:Ba ratio and reaction temperature could be explained based on relative differences in supersaturation between the experiments. With high supersaturation, growth proceeds by a hopper-growth mechanism, while lower supersaturation promotes layer-by-layer growth.

Contents

1 Background

1.1 Motivation

In 1920 Valasek reported on the first electrical hysteresis loop on the Rochelle salt $NaKC_4H_4O_6 \cdot 6H_2O$, and become the first to experimentally find the electric analogy to the more well-known hysteresis loops in ferromagnetic materials [1]. Until the early 1940s, with the discovery of $BaTiO_3$ by several groups [2], ferroelectrics were mostly academic curiosities with few applications [3]. Since then many more materials have been discovered, including state-of-the-art $PbZr_xTi_{1-x}O_3$ (PZT) [4], which together with $BaTiO_3$ are both part of the important perovskite class of materials. Other important material classes are tungsten bronzes [5], pyrochlores [6] and Aurivillius compounds [7] (also called bismuth layered structures). Today, ferroelectric materials have become an integral part of our technological society in the form of thin films integrated with the semiconductor industry [3], sensors [8] and actuators [9] to list some important examples. In the future, we might have new lens technology in our mobile devices with the poLight AS TLens® and even robot bees [10] pollinating our crops, both working based on ferroelectric actuators. With the general growing interest in nanomaterials due to size dependent properties [11] and downscaling of devices , there is today also a growing interest in nanostructured ferroelectrics. These materials have possible applications in non-volatile ferroelectric memories [12], energy harvesting [13], bio-sensing [14] and for fundamental studies of the finite size effects of ferroelectricity [15].

The increasing interest for nanostructured ferroelectrics demands developments in suitable synthesis routes of these materials. For any kind of material, the ideal synthesis route should be environmental-friendly, cheap, a low temperature process, controllable, reproducible and perhaps most importantly, yield high quality materials. For the preparation

of nanostructured ferroelectrics with controlled size and morphology or hierarchical structures, hydrothermal synthesis, see Figure 1.1, stands out as one of the most promising[16, 17]. Hydrothermal synthesis was in its beginning in the mid-nineteenth century a way for geologist to simulate the formation conditions of naturally occurring minerals [18]. Currently, the main focus using the hydrothermal method is on technological inorganic materials without natural analogues with an extra focus on the preparation of nanostructured materials [18]. Today, the list of materials, size ranges and morphologies of the materials that have been prepared by the hydrothermal method is too long to be listed here, but common for most of these, is that a trial-and-error approach, in addition to chemical intuition probably played a big role in the development of the specific synthesis routes. This approach follows from the lack of fundamental understanding of the nucleation and growth process taking place inside the autoclave. For further improvement, development, control and utilization of the hydrothermal method, a more fundamental understanding is required. We need to understand the "*chemistry of nucleation*" as expressed by Bøjesen and Iversen [19].

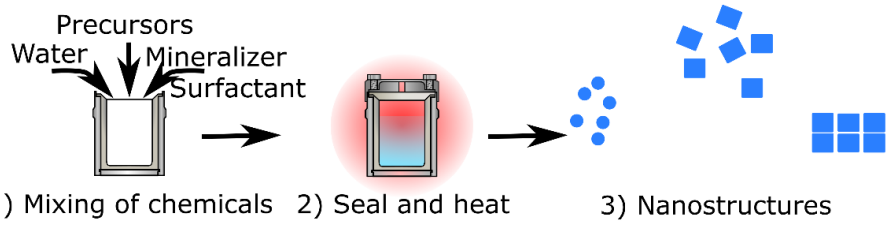

Figure 1.1: Schematic illustration of hydrothermal synthesis, from mixing of precursors, solvent and additives in the autoclave to the final product.

Several groups have for the last decades utilized *in situ* techniques for looking into the "*black box*" that is the autoclave used for hydrothermal synthesis, with various experimental setups, radiation sources and techniques [20]. Today, these *in situ* experiments are mostly performed using synchrotron X-ray diffraction with a capillary setup first developed by Norby *et al.* [21, 22], before being significantly improved by Becker *et al.* [23], see Figure 1.2. These type of experiments have proven their versatility, revealing an oriented attachment mechanism for growth of TiO_2 nanoparticles [24], pre-nucleation cluster for a range of binary oxides [19] and an intricate nucleation pathway for $NaNbO_3$ [25]. With the current achievements of the "*in situ* hydrothermal community" in mind, there is no doubt that there is still not an atomic scale understanding of the governing mechanism occurring during hydrothermal synthesis. More material systems need to be investigated, and already studied material systems still need

attention to fully explore the complexity that inorganic chemistry with the entire periodic table as playing ground has to offer.

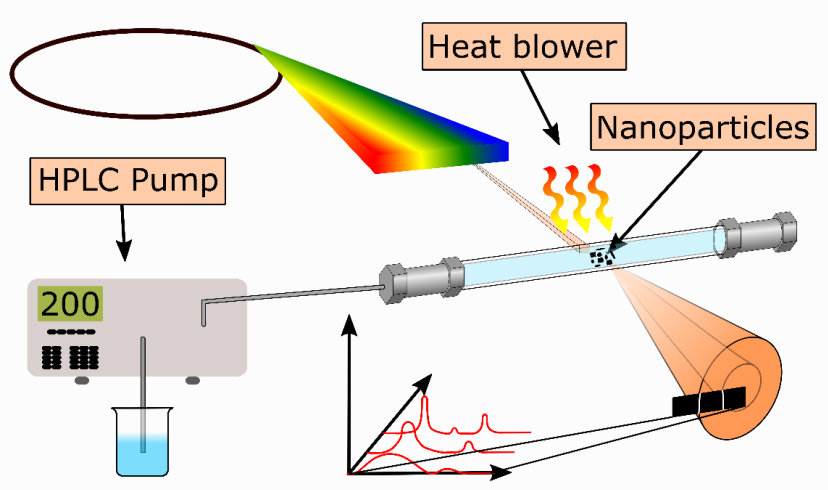

Figure 1.2: Schematic illustration the setup for *in situ* synchrotron X-ray diffraction experiments. A capillary is used as reaction vessel. The capillary is heated with a hot air-stream and pressurized with a HPLC pump. High brilliance X-rays and 2D detectors allows for the capture of full diffraction patterns within fractions of a second, giving high time resolution.

1.2 Aim of the work

The main objective of this thesis is to provide fundamental understanding of the nucleation and growth during hydrothermal synthesis so that the current trial-and-error processes in synthesis optimization can become a rational design of synthesis parameters. The focus is on technologically important nanosized ferroelectric materials, and on environmental-friendly water-based synthesis of especially lead-free ferroelectric materials, following the large efforts of the community for finding lead-free alternatives to replace state-of-the art PZT. The work consisted of two parts, which both contribute to an increased knowledge of nucleation and growth during hydrothermal synthesis.

The first part of this work, aimed at expanding the knowledge related to hydrothermal synthesis of the technologically important $BaTiO_3$ (BT) by exploring nucleation and growth from two new precursor chemistries with *in situ* X-ray diffraction. BT is a well-studied perovskite ferroelectric, including several previous *in situ* characterization investigations, which makes it one of few candidate materials for comparison with existing literature. Interestingly, we found that from quite similar precursor chemistries significantly different growth kinetics were observed, still yielding a similar final nanosized BT.

The second part of this work aimed at studying a new material system, both in regards to *in situ* X-ray studies, but also hydrothermal synthesis. Tetragonal tungsten bronze $Sr_xBa_{1-x}Nb_2O_6$ (SBN100*x*, $0.2 < x < 0.8$) was chosen for this part of the work. SBN, and other tungsten bronzes, have gained an increased interest in the quest of replacing PZT, in addition to being well studied for its optical properties. Opposed to BT, there exist hardly any literature on the hydrothermal synthesis of SBN, and no investigations on nucleation and growth of SBN under these conditions. A new hydrothermal route for the synthesis of SBN was developed, which was studied in detail with a combination of *in situ* X-ray diffraction and X-ray total scattering experiments. The structure of the amorphous precursor observed by X-ray total scattering was linked to a change in growth mechanism, from layer-by-layer growth, to hopper growth, as a function of decreasing Sr-fraction in the precursor slurry and the reaction temperature.

References

1. Valasek, J. Piezo-electric and allied phenomena in Rochelle salt, *Physical Review* **17**, 475-481, (1921). DOI: 10.1103/PhysRev.17.475

2. Haertling, G. H. Ferroelectric ceramics: history and technology, *Journal of the American Ceramic Society* **82**, 797-818, (1999). DOI: 10.1111/j.1151-2916.1999.tb01840.x

3. Scott, J. F. Applications of modern ferroelectrics, *Science* **315**, 954-959, (2007). DOI: 10.1126/science.1129564

4. Panda, P. K. and Sahoo, B. PZT to lead free piezo ceramics: a review, *Ferroelectrics* **474**, 128-143, (2015). DOI: 10.1080/00150193.2015.997146

5. Jamieson, P. B., Abrahams, S. C. and Bernstein, J. L. Ferroelectric tungsten bronze-type crystal structures. I. Barium strontium niobate $Ba_{0.27}Sr_{0.75}Nb_2O_{5.78}$, *The Journal of Chemical Physics* **48**, 5048-5057, (1968). DOI: 10.1063/1.1668176

6. Bernard, D., Pannetier, J. and Lucas, J. Ferroelectric and antiferroelectric materials with pyrochlore structure, *Ferroelectrics* **21**, 429-431, (1978). DOI: 10.1080/00150197808237288

7. Moure, A. Review and perspectives of aurivillius structures as a lead-free piezoelectric system, *Applied Sciences* **8**, (2018). DOI: 10.3390/app8010062

8. Damjanovic, D., Muralt, P. and Setter, N. Ferroelectric sensors, *IEEE Sensors Journal* **1**, 191-206, (2001). DOI: 10.1109/JSEN.2001.954832

9. Aksel, E. and Jones, J. L. Advances in lead-free piezoelectric materials for sensors and actuators, *Sensors (Basel)* **10**, 1935-1954, (2010). DOI: 10.3390/s100301935

10. Jafferis, N. T., Helbling, E. F., Karpelson, M. and Wood, R. J. Untethered flight of an insect-sized flapping-wing microscale aerial vehicle, *Nature* **570**, 491-495, (2019). DOI: 10.1038/s41586-019-1322-0

11. Banfield, J. F. and Zhang, H. Nanoparticles in the environment, *Reviews in Mineralogy and Geochemistry* **44**, 1-58, (2001). DOI: 10.2138/rmg.2001.44.01

12. Shen, Z., Chen, Z., Lu, Q., Qiu, Z., Jiang, A., Qu, X., Chen, Y. and Liu, R. Nano-embossing technology on ferroelectric thin film $Pb(Zr_{0.3},Ti_{0.7})O_3$ for multi-bit storage application, *Nanoscale Research Letters* **6**, 474, (2011). DOI: 10.1186/1556-276X-6-474

13. Bowen, C. R., Kim, H. A., Weaver, P. M. and Dunn, S. Piezoelectric and ferroelectric materials and structures for energy harvesting applications, *Energy & Environmental Science* **7**, 25-44, (2014). DOI: 10.1039/C3EE42454E

14. Blázquez-Castro, A., García-Cabañes, A. and Carrascosa, M. Biological applications of ferroelectric materials, *Applied Physics Reviews* **5**, 041101, (2018). DOI: 10.1063/1.5044472

15. Page, K., Proffen, T., Niederberger, M. and Seshadri, R. Probing local dipoles and ligand structure in $BaTiO_3$ nanoparticles, *Chemistry of Materials* **22**, 4386-4391, (2010). DOI: 10.1021/cm100440p

16. Einarsrud, M.-A. and Grande, T. 1D oxide nanostructures from chemical solutions, *Chemical Society Reviews* **43**, 2187-2199, (2014). DOI: 10.1039/C3CS60219B

17. Rørvik, P. M., Grande, T. and Einarsrud, M.-A. One-dimensional nanostructures of ferroelectric perovskites, *Advanced Materials* **23**, 4007-4034, (2011). DOI: 10.1002/adma.201004676

18. Byrappa, K. and Yoshimura, M., in *Handbook of Hydrothermal Technology*, William Andrew Publishing, Oxford, Second Edition, Chp. 2, 51-73, (2013). DOI: 10.1016/B978-0-12-375090-7.00002-5

19. Bøjesen, E. D. and Iversen, B. B. The chemistry of nucleation, *CrystEngComm* **18**, 8332-8353, (2016). DOI: 10.1039/C6CE01489E

20. Jensen, K. M., Tyrsted, C., Bremholm, M. and Iversen, B. B. *In situ* studies of solvothermal synthesis of energy materials, *ChemSusChem* **7**, 1594-1611, (2014). DOI: 10.1002/cssc.201301042

21. Norby, P., Nørlund Christensen, A. and Hanson, J. C. *In situ* studies of zeolite syntheses using powder diffraction methods. Crystallization of "instant zeolite A" powder and synthesis of CoAPO-5, *Studies in Surface Science and Catalysis* **84**, 179-186, (1994). DOI: 10.1016/S0167-2991(08)64112-9

22. Norby, P. Hydrothermal conversion of ceolites: an *in situ* synchrotron X-ray powder diffraction study, *Journal of the American Chemical Society* **119**, 5215-5221, (1997). DOI: 10.1021/ja964245g

23. Becker, J., Bremholm, M., Tyrsted, C., Pauw, B., Jensen, K. M. O., Eltzholt, J., Christensen, M. and Iversen, B. B. Experimental setup for *in situ* X-ray SAXS/WAXS/PDF studies of the formation and growth of nanoparticles in near- and supercritical fluids, *Journal of Applied Crystallography* **43**, 729-736, (2010). DOI: 10.1107/S0021889810014688

24. Dalod, A. R. M., Grendal, O. G., Skjærvø, S. L., Inzani, K., Selbach, S. M., Henriksen, L., van Beek, W., Grande, T. and Einarsrud, M.-A. Controlling oriented attachment and *in situ* functionalization of TiO_2 nanoparticles during hydrothermal synthesis with APTES, *The Journal of Physical Chemistry C* **121**, 11897-11906, (2017). DOI: 10.1021/acs.jpcc.7b02604

25. Skjærvø, S. L., Wells, K. H., Sommer, S., Vu, T.-D., Tolchard, J. R., van Beek, W., Grande, T., Iversen, B. B. and Einarsrud, M.-A. Rationalization of hydrothermal synthesis of $NaNbO_3$ by rapid *in situ* time-resolved synchrotron X-ray diffraction, *Crystal Growth & Design* **18**, 770-774, (2018). DOI: 10.1021/acs.cgd.7b01192

2 Introduction

In the following sections an introduction to key topics are presented, including ferroelectricity, hydrothermal synthesis and *in situ* X-ray diffraction studies. The two material systems studied in this work, $BaTiO_3$ (BT) and $Sr_xBa_{1-x}Nb_2O_6$ (SBN), are also introduced.

2.1 Ferroelectricity

2.1.1 Fundamentals

The characteristic feature for all ferroelectric materials is that they have a spontaneous polarization (P_s) below their Curie temperature (T_c), which is switchable in an applied electric field (E) [1]. The first prerequisite for ferroelectricity is an electrically insulating material (*i.e.* a dielectric), so that an applied electric field does not induce an ohmic current through the material. Secondly, the crystal structure needs a unique polar axis (*i.e.* piezoelectricity). Piezoelectricity refers to the material property inducing electrical polarization in the material by an applied mechanical stress, and *vice versa*, mechanical stress in the material by an applied electric field. Lastly, the crystal structure needs to be spontaneously polarized along the polar axis below a critical temperature (T_c) (*i.e.* pyroelectricity), and as mentioned, this polarization needs to be switchable. From this it follows that all ferroelectric materials are a subclass of pyroelectric materials (have a spontaneous polarization that is not switchable by an applied electric field), which is further a subclass of piezoelectric materials (polarized with an applied mechanical stress). This means that all ferroelectric materials are piezoelectric and pyroelectric, but not necessarily the other way around (*e.g.* quartz is piezoelectric but not pyro- or ferroelectric). Furthermore,

all ferroelectric crystals therefore belong to one of the 10 polar out of the total 32 point groups [2].

There are several mechanisms for spontaneous polarization in ferroelectric materials. One common mechanism is displacement of a cation from a second-order Jahn-Teller mechanism due to partial covalence between empty transition metal *d*-states and oxygen *p*-states [3]. This is typical for d^0 transition metal perovskite oxides, exemplified with the displacement of Ti^{4+} in $BaTiO_3$ in Figure 2.1. Some other mechanisms are related to electron lone-pairs (*e.g.* $PbTiO_3$, $BiFeO_3$) [4], charge ordering (*e.g.* $LuFe_2O_4$) [4] and geometric mechanisms (*e.g.* rare earth hexagonal manganites) [5].

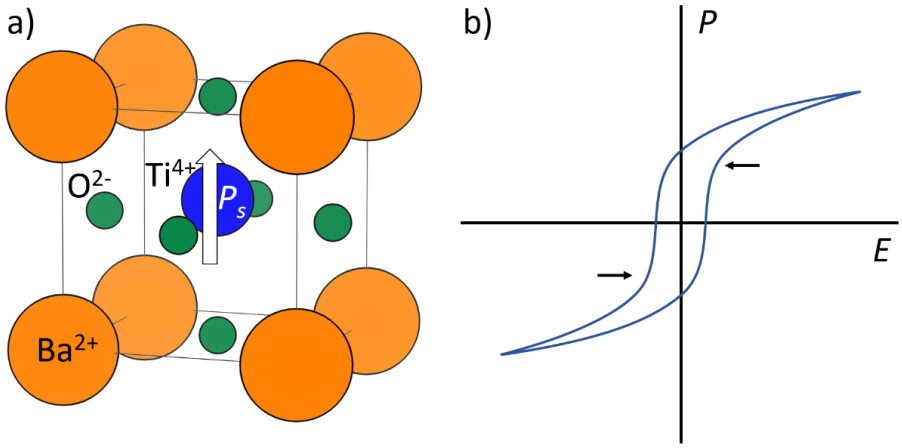

Figure 2.1: a) Unit cell of $BaTiO_3$ showing the off-centering of Ti^{4+} (in blue) giving a microscopic electric dipole (P_s). b) A typical hysteresis loop for a ferroelectric material when polarization is measured as a function of an applied electric field. Notice the change in gradient (arrows) which in addition to the hysteresis is indicative of a switching of the polarization direction, and thus ferroelectricity.

In the absence of an applied electric field, a ferroelectric material will consist of regions of uniformly oriented polarization, called domains, separated by domain walls. The domains will form and orient them self in order to lower the total polarization (*i.e.* different domains will cancel each other, giving no net polarization) [6]. In addition to no net polarization, a ferroelectric material in this state will also have no net piezoelectric response, since the domains in total cancel each other out. By applying a sufficiently large field to switch the polarization direction, the polarizations can be aligned (*i.e.* domains can be reoriented), making the net polarization ≠ 0. This is called poling of the material. This

switching behavior, shown as a hysteresis in Figure 2.1, is how ferroelectricity is demonstrated in materials. It is also the key for any application utilizing the piezoelectric properties of ferroelectric materials, as the material will now have a net piezoelectric response. A hysteresis loop without the change in gradient, indicated with arrows in Figure 2.1 (*i.e.* a hysteresis loop with a cigar-shape) can be measured for any leaky dielectric material and is not necessarily evidence for ferroelectricity, as presented in the "Ferroelectrics go bananas"-paper [7].

Even though $BaTiO_3$ sparked the interest for ferroelectric materials [8], the solid solution $PbZr_xTi_{1-x}O_3$ (PZT) has become the technologically most important ferroelectric material due to its superior properties [9]. Both of these materials have the perovskite structure (general formula ABO_3), which is the most important class of ferroelectric materials. Other perovskite ferroelectric materials include doped $BaTiO_3$ (normally with Ca^{2+} and/or Zr^{4+}), the solid solution $K_xNa_{1-x}NbO_3$ with doping and the solid solution $Bi_{0.5}(Na_xK_{1-x})TiO_3$ with doping [10]. Second to the perovskite class of ferroelectric materials are the tetragonal tungsten bronzes (TTB) with the general formula $(A1)_2(A2)_4C_4(B1)_2(B2)_8O_{30}$ [11]. As for the perovskite structure, a great number of materials can be accommodated in this structure, exemplified with the three subclasses of TTBs based on the cation filling of the A1, A2 and C sites. For example, $K_6Li_4Nb_{10}O_{30}$ is a *stuffed* TTB (*i.e.* all A1, A2 and C sites are filled), $Ba_2Na_4Nb_{10}O_{30}$ is a *filled* TTB (*i.e.* A1 and A2 sites are filled while the C site is empty) and $Sr_{5x}Ba_{5-5x}Nb_{10}O_{30}$ is an *unfilled* TTB (*i.e.* A1 and A2 sites are partly filled while the C site is empty) [12]. Other important material classes are pyrochlores [13] and Aurivillius compounds [14] (also called bismuth layered structures), that in combination with TTBs and lead-free perovskite materials are extensively studied in an attempt to replace PZT [10, 15]

2.1.2 Applications for nanostructured ferroelectrics

Nanostructured ferroelectric materials in different forms show great promise for a wide range of applications [16]. For example, the switchable polarization can be used to represent the binary "1" and "0", and can thus be used for data storage in ferroelectric random access memory (FeRAM). With nanostructured ferroelectrics, for example nanotubes or nanorod arrays, a high storage density can be achieved [16, 17]. Energy harvesting is another promising application for nanostructured ferroelectrics [18]. By using PZT nanowires embedded in the soft polymer polydimethylsiloxane (PDMS), a peak output of 1.6 V have been reported [19]. Other device designs and lead-free ferroelectric materials have also showed promise for energy harvesting applications, for example vertically aligned nanorod arrays of $BaTiO_3$ and

$K_xNa_{1-x}NbO_3$ [20, 21]. Ferroelectric materials are used for sensing applications in their bulk form, and with the increased specific surface area (m^2/g) obtained for nanostructured materials the sensing properties can be improved [22]. The photocatalytic properties of ferroelectric materials will also benefit from the increased specific surface area of nanostructured materials [18, 23]. Furthermore, in biomedical applications, $BaTiO_3$ nanoparticles and $BiFeO_3$ nanofilms have shown to improve bone regeneration [24]. Lastly, nanostructured ferroelectric materials are also important for fundamental studies on finite size effects of the ferroelectric properties [25, 26]. Hence, there is a wide range of possible applications for nanostructured ferroelectric materials meriting further investigations into the synthesis of these materials.

2.2 The materials: $BaTiO_3$ and $Sr_xBa_{1-x}Nb_2O_6$

2.2.1 Perovskite $BaTiO_3$

Structure and properties

$BaTiO_3$ (BT) crystalizes in the tetragonal polymorph (space group no. 99, *P*4*mm*) of the perovskite structure at room temperature (RT), and is a II-IV perovskite ($A^{II}B^{IV}O_3$), referring to the valance of the Ba- and Ti-cations. The perovskite structure is easiest visualized as a network of corner sharing TiO_6-octahedra, with Ba^{2+} in 12-fold cuboctahedral coordination, as seen in Figure 2.2. At around 125 °C (T_c), BT goes from tetragonal to cubic and becomes paraelectric (space group no. 221, $Pm\bar{3}m$). Upon cooling, BT undergoes two phase transitions, first from tetragonal to orthorhombic (space group no. 38, *Amm*2) before becoming rhombohedral (space group no. 160, *R*3*m*) around -5 and -90 °C respectively [27].

Today, BT and BT-based materials are the most widely used in dielectric capacitors because of the high dielectric constant [8]. Due to the low T_c relative to PZT, BT is not extensively used for its piezo- or pyroelectric properties, but with the increased focus on finding lead-free alternatives, this is changing. Doping BT with especially Ca^{2+} (A-site doping) and Zr^{4+} (B-site doping), are improving the piezoelectric properties and making doped BT a candidate for low temperature applications (-40 to 120 °C) in consumer electronics [6], *e.g.* energy harvesting devices [20], transducers and microphones [6, 15]. For biomedical applications the low T_c is not limiting, and BT being biocompatible has great potential for uses in medical applications and implants [6]. Especially interesting is the use of doped BT as a functional implant to aid in bone growth and recovery [28, 29]. Furthermore, recent investigations have shown that doped BT has promising properties for electrocalorics [30], flexible sensors [31], photoluminescence [32] and electro-optics [33]. In addition to its properties, BT has been, and

still is, researched as a model system to gain further insight and understanding of ferroelectric materials and phase transitions in ferroelectric perovskite materials. This is unlikely to change with the downscaling and nanosizing of ferroelectric materials.

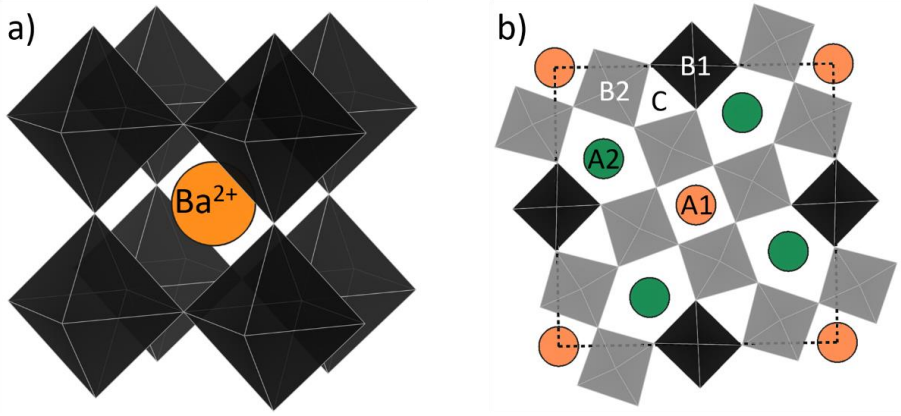

Figure 2.2: a) Unit cell of BT showing network of corner-sharing TiO_6 octahedra in black and Ba^{2+} in 12-fold cuboctahedral coordination in orange. b) Unit cell of SBN projected on the *ab*-plane. NbO_6 octahedra are indicated in black and grey (B1 and B2), the triangular C-sites are empty and the square A1- and pentagonal A2-sites are orange and green respectively. Both figures are made using VESTA [34].

2.2.2 Tetragonal tungsten bronze $Sr_xBa_{1-x}Nb_2O_6$

Structure and properties

$Sr_xBa_{1-x}Nb_2O_6$ (SBN100*x*, 0.32 < *x* < 0.82) is a lead-free ferroelectric with an unfilled tetragonal tungsten-bronze (TTB) structure [35, 36]. The average structure at room temperature is described by the non-centrosymmetric *P*4*bm* (no. 100) space group, while the high-temperature non-ferroelectric phase is described by the centrosymmetric *P*4/*mbm* (no. 127) space group. The structure can be seen as a network of corner-sharing NbO_6 octahedra forming triangular C-sites (empty in SBN), square A1-sites and pentagonal A2-sites [35, 37], as shown in Figure 2.2, and is linked with the perovskite structure by a rotation of groups of octahedra [38], as schematically shown in Figure 2.3. The C-, A1- and A2-sites are forming channels running along the [001]-direction. A total of 5 alkaline earth and 1 vacancy are distributed on the 6 atomic sites (2 A1- and 4 A2-sites). The structure of SBN is flexible with respect to Sr:Ba ratio, making SBN stable for a wide range of compositions. At room temperature, the stability range is reported to be $x = 0.32 - 0.82$ [36], with an even wider range at higher temperatures [39]. The structure is known to have incommensurate tilt patterns of the

NbO_6 octahedra [40, 41]. The larger Ba^{2+} is often assumed to be only located on the larger A2-sites, but several works have shown the possibility of cation-disorder (both Sr^{2+} and Ba^{2+} on both A1- and A2-sites), both experimentally [42, 43] and with simulations [44, 45], and signs of correlated disorder [46].

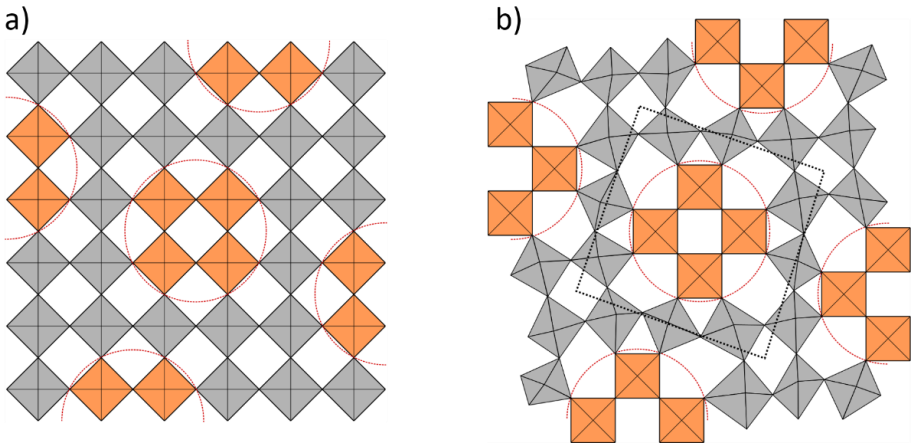

Figure 2.3: Relationship between the perovskite and tetragonal tungsten bronze structure. a) The perovskite structure with corner-sharing octahedra. b) The tetragonal tungsten bronze structure projected onto the *ab*-plan is obtained by rotating the octahdra in orange by 45 degrees as indicated by red dashed circles. The tetragonal unit cell is indicated with a black dashed line. Figure made based on ref [38].

The properties of SBN is directly linked to the flexible chemistry. SBN can be tuned from having normal to relaxor ferroelectric properties [47], and the T_c can be tuned from 60 to 230 °C [48] as a function of the Sr fraction. Still, SBN has historically been studied because of its high electro-optic coefficients [49] and photorefractive properties [50], which have spurred research in using SBN in holographic displays [51, 52]. In addition to this, SBN is reported to have good pyroelectric properties [53, 54] and photocatalytic activity [23, 55]. Furthermore, filled SBN ($Sr_xBa_{1.2-x}Nb_2O_6$) is reported to show low temperature superconductivity [56] and reduced SBN ($Sr_xBa_{1-x}Nb_2O_{6-\delta}$) have good thermoelectric properties [57].

2.3 Hydrothermal synthesis

Hydrothermal synthesis refers to reactions in aqueous media at elevated temperatures and pressures, normally higher than 100 °C and 1 bar, and is known as a versatile synthesis route for nanostructured materials [58, 59], including ferroelectric materials [17, 60]. If another solvent than water is used, *e.g.* alcohols or other organic solvents, the method is called

solvothermal synthesis. Conventional batch hydrothermal synthesis is performed in a closed vessel shown in Figure 2.4, called an autoclave, which is normally heated in an oven. More recently, setups for microwave assisted hydrothermal synthesis is developed, allowing for fast and uniform heating of the content in the autoclave [61]. The increased temperature gives rise to an autogenous pressure inside the closed autoclave, which is dependent on the filling factor, as shown in Figure 2.5. With increasing temperature and pressure, the properties of water changes, as shown for the density, dielectric constant and ionic product as a function of temperature at a pressure of 300 bar in Figure 2.5 [58, 60], and the reactivity of the precursors are increased. The density of water decreases with increasing temperature while the density of the gas phase increases, until the densities become equal at the critical point (374 °C and 221 bar), above which water is supercritical. With the transition to the supercritical phase, a drop in the dielectric constant is observed, making water change from a polar to a non-polar solvent. The viscosity of water is known to decrease with increasing temperature, thus increasing the mobility of molecules and ions in the solution.

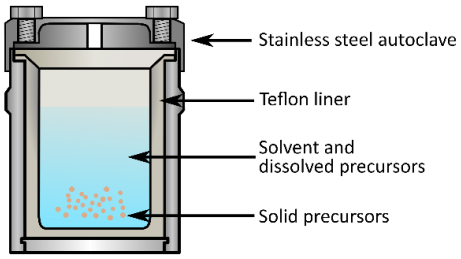

Figure 2.4: Schematic cross-section of a conventional stainless steel autoclave, with Teflon liner, solvent and solute and solid precursor.

The increased reactivity and high mobility of dissolved species allows for the use of a wide range of precursors that will be homogenously mixed. Common precursors include metal salts (*e.g.* nitrates, hydroxides, acetates, and chlorides), metal alkoxides and metal oxides. In addition to the precursor, a mineralizer (*e.g.* NaOH and KOH) can be added to further increase solubility and a surfactant to stabilize colloidal particles and/or act as growth directing agents. In total, the properties of water, precursor flexibility, potential additives and reaction parameters (*i.e.* reaction time, reaction temperature, filling factor and pH) give the

hydrothermal method a great potential for the designed synthesis of nanostructured ferroelectrics, but it also makes an incredibly complex system to fully understand and control.

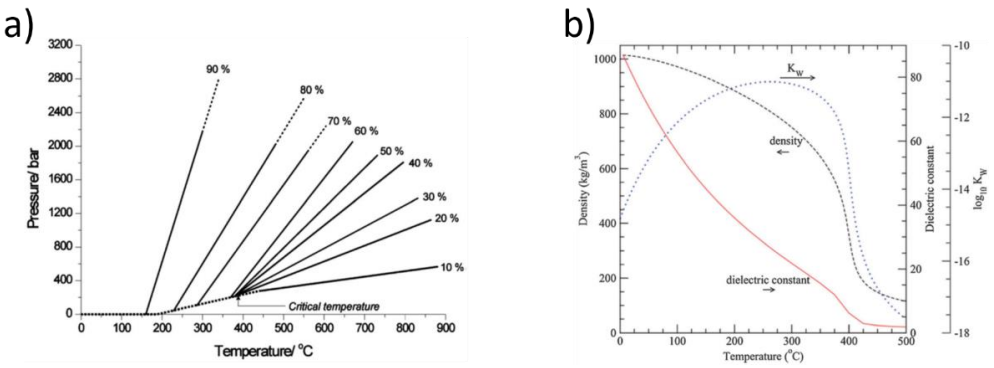

Figure 2.5: a) Pressure-temperature dependence of water with different filling factors of the autoclave. b) Density, dielectric constant and ionic product for water as a function of temperature at a constant pressure of 300 bar. Reproduced from ref. [60] with permission from The Royal Society of Chemistry.

2.3.1 Nucleation and growth

Classical theories

Homogenous nucleation, meaning formation of nuclei in a parent phase (*e.g.* nucleation in a solution) is described thermodynamically by considering the surface energy (γ) and the bulk free energy of the forming nuclei (ΔG_v) [62]. The total free energy for the formation of a nuclei can then be written as the sum of the total surface energy and total bulk free energy when assuming spherical nuclei with a single interfacial surface energy, as in Equation 2.1, with r being the radius of the nuclei.

$$\Delta G = 4\pi r^2 \gamma + \frac{4}{3}\pi r^3 \Delta G_v \qquad (2.1)$$

The bulk free energy of the nuclei (ΔG_v) is dependent on the temperature and supersaturation (S), as shown in Equation 2.2, where k_b is the Boltzmann's constant, T is the temperature and v the molar volume [62].

$$\Delta G_v = -\frac{k_b T \ln S}{v} \qquad (2.2)$$

The formation of a new surface (surface of the nuclei) acts as an energy barrier for the formation of stable nuclei, while the degree of supersaturation acts as a driving force by

promoting the formation of the thermodynamically stable phase. For small *r*, the surface term in Equation 2.1 will dominate and suppress the formation of stable nuclei (the nuclei are called embryos at this stage), while for larger *r* the volume term dominates, as shown in Figure 2.6. This means that the nuclei are only stable when larger than a critical size, r_c (see Figure 2.6), smaller than this they will dissolve back into the solution. This thermodynamic description of nucleation is a stochastic process, where the probability for the random formation of a stable nuclei increases with increasing driving force (*i.e.* supersaturation), but can occur at different times for identical systems and conditions [63, 64]. An extension of the homogenous nucleation theory is the LaMer model [65], as shown in Figure 2.6 b), where the monomer concentration is initially increasing up to a critical supersaturation (C_{max}). Here a rapid nucleation occur, lowering the supersaturation below the level of self-nucleation (C_{min}), stopping further nucleation, and only growth occurs.

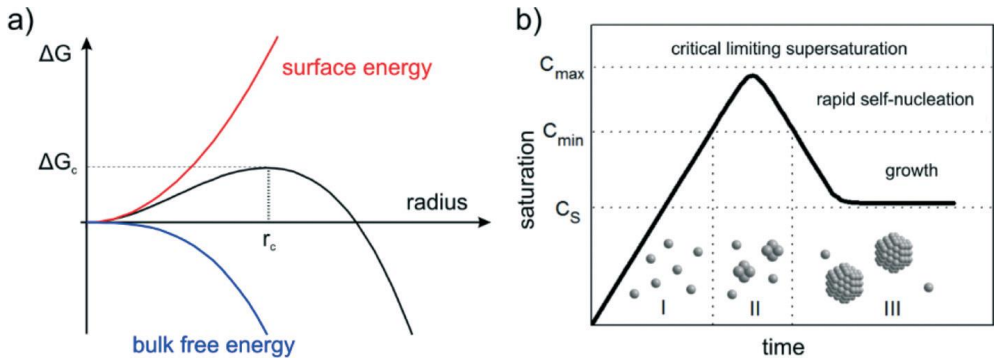

Figure 2.6: a) Surface energy ($4\pi r^2\gamma$), bulk free energy (ΔG_v) and total free energy (ΔG) for a forming nuclei as a function of nuclei size (*r*). b) Nanoparticle nucleation by LaMer's nucleation theory, qualitatively showing monomer concentration (*C*) as a function of time. Reproduced from ref. [65] under the Creative Commons Attribution Unported License (CC BY 3.0).

The classical theories for growth occurring after the initial nucleation is described by the addition of monomers (*e.g.* ions, molecules or atoms) from the surrounding solution to the surface of the growing crystal [66]. At lower to moderate supersaturations this process is seen as a layer-by-layer growth, where new layers normally form at edges and corners of the growing crystal due to the Berg effect [67] (*i.e.* higher supersaturation at edges and corners than at facets). This growth leads to particle shape symmetry reflecting the unit cell of the material, with macroscopically flat facets because of an "equilibrium" between the formation of new layers, and the completion of these layers. At higher supersaturation, this equilibrium

can be disrupted [64, 68], and what is known as skeletal growth can occur [69], where edges and corners grow faster than the facets, leading to intricately shaped crystals, as shown in Figure 2.7. These can be referred to as skeletal crystals, but are normally differentiated into hopper (or just hoppers as for bismuth in Figure 2.7) and dendritic crystals (or just dendrites as for the ice crystal in Figure 2.7). At early stages of classical growth, the growth rate is generally described as being limited either by the surface reaction (*i.e.* incorporation of monomers onto the surface of the growing crystal) or by diffusion of monomers (*i.e.* diffusion of monomers to the surface of the growing crystal). One of the classical growth models is the Ostwald ripening mechanism [70], where larger crystals grow on the expense of smaller ones by a dissolution-precipitation mechanism, because of the higher solubility of smaller crystals [62]. This growth can also be limited by the dissolution of the smaller particles, in addition to surface reaction and diffusion. The rate limiting mechanism can be found by modeling the kinetics, and several models have been developed for this, for example the Johnson-Mehl-Avrami-Kolmogorov (JMAK) model [71], as described in Equation 2.3. Here f is the fractional extent of the reaction as a function of time (t) after the first appearance of the phase (t_0), k is a rate constant and n is the growth order being linked to the rate limiting mechanism [71, 72].

$$f = 1 - \exp(-k(t - t_0)^n) \tag{2.3}$$

The JMAK model was developed to describe solid-state reactions, but the model has also been used for modeling growth kinetics during hydrothermal reactions [73-75]. Some of the assumptions of the model (*e.g.* isotropic growth and constant reaction conditions) are not always applicable for hydrothermal reactions, and care must be taken to not ascribe too much physical meaning to the refined values, especially for n [72].

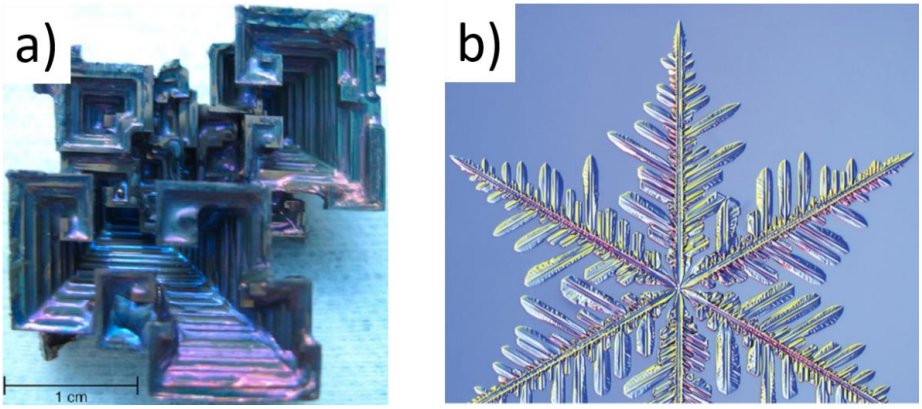

Figure 2.7: a) Hopper-crystal of bismuth. Reproduced from ref. [76]. Copyright 2013 American Chemical Society. b) Dendritic ice crystal. Reproduced from ref. [77] with permission from Annual Reviews.

Non-classical theories

In the thermodynamic description of nucleation there is a critical size, r_c, for which a nuclei larger than this is stable and unstable when smaller. In recent years, observations of small, so-called pre-nucleation clusters have been observed [78, 79]. These are small thermodynamically stable solutes even before nucleation, that are composed of atoms, molecules or ions of the forming solid and acts as molecular precursors [79]. Studying the structure and transformation of these into crystalline materials have shown that these pre-nucleation clusters can decompose into smaller units [80], or undergo just small structural changes [81] (*e.g.* rotations or coordination) before crystallization.

Non-classical growth can generally be described as growth by particle-particle interaction, as opposed to the particle-monomer interactions as described by classical growth theory. For example, oriented attachment is the process of two particles attaching together along a common crystallographic plane, resulting in a new monocrystalline particle [82]. This mechanism has been reported for TiO_2 nanoparticles during hydrothermal synthesis, forming chain like structures [83] and nanorods [84]. Furthermore, the formation of mesocrystals, where primary particles assemble together aided by surfactants grafted to the particle surface is another described growth mechanism [85]. These mesocrystals can be stabilized in their mesocrystal form, or fuse together and form polycrystalline or even monocrystalline particles [86]. A summary of the non-classical theories for nucleation and growth is presented in Figure 2.8.

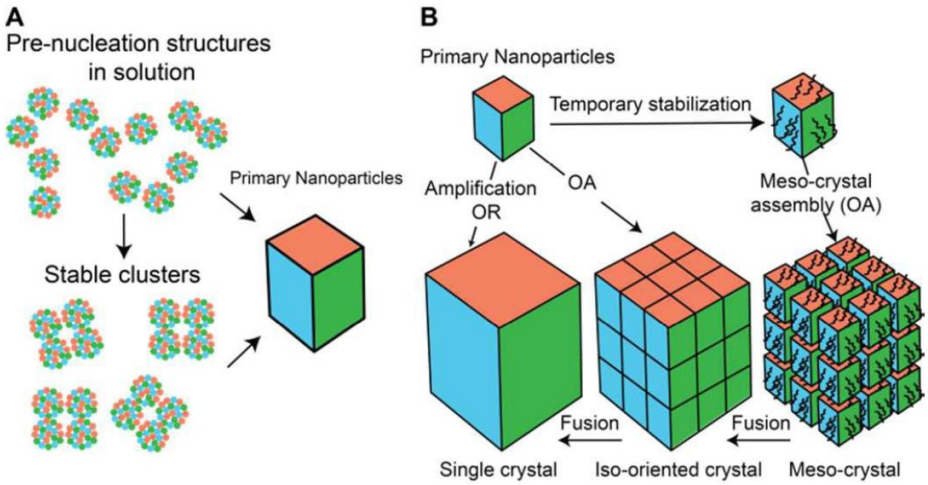

Figure 2.8: a) Schematic of non-classical nucleation with pre-nucleation clusters forming stable clusters or nanoparticle nuclei. b) Possible growth routes for the nanoparticle nuclei: Ostwald ripening (OR), oriented attachment (OA) and mesocrystal formation. Reproduced from ref. [63] with permission from The Royal Society of Chemistry.

The theories described here, until the development of one single theory that can accommodate them all, should be considered complimentary, explaining their part of the complex nucleation and growth of inorganic materials. To be able to fully control these underlying mechanisms, so that rational design of particle size and morphology can be achieved, a more complete understanding is needed. By studying the nucleation and growth in real time by *in situ* experiments, this fundamental understanding can be achieved. In section 2.4 an introduction to *in situ* hydrothermal synthesis experiments is presented.

2.3.2 Hydro-/solvothermal synthesis of $BaTiO_3$

BT is a technological important material with a high interest among scientist for several decades, a comprehensive review of the literature on hydrothermal synthesis of BT is therefore not given. The focus in this overview is on hydrothermal/solvothermal synthesis of nanostructured BT and reported reaction mechanisms.

A wide range of different reaction conditions and precursors have been successfully used to synthesize BT [87]. Common barium precursors are barium salts (*e.g.* hydroxides, nitrates and acetates) or barium alkoxides and common titanium precursors are titanium alkoxides, $TiCl_4$ or TiO_2 (crystalline or as an amorphous $TiO_2{\cdot}xH_2O$ precipitate after hydrolysis of alkoxides or $TiCl_4$). Reaction times and temperatures are typically in the range

of a few hours to several days and 100 to 300 °C, respectively. Solvents are commonly water, water-ethanol mixtures or other alcohols. The mineralizer concentration (*e.g.* NaOH, KOH) needs to be high typically giving pH > 12, to form BT [88]. A range of different sizes and morphologies have been reported, for example spherical particles ranging from 5 to 150 nm [89-92], cube-shaped particles ranging from 5 to 200 nm [93-96], rods and wires with different aspect ratios [97, 98], nanotories [96] and dendrites [99-101]. For example, size control of spherical BT nanoparticles from 40 to 150 nm have been achieved by changing the ratio between water and isopropanol when using barium hydroxide and titanium isopropoxide as precursors [91]. Even smaller spherical particle sizes (~5 nm) were achieved using barium metal and titanium isopropoxide in anhydrous benzyl alcohol.

The formation mechanism of BT is typically best described with a dissolution-precipitation mechanism in the case of several different precursors, especially when crystalline or amorphous TiO_2 is used as titanium source (see section 2.4.2). For some cases though, a topotactic transformation is the most likely formation mechanism, since the morphology of the precursor is kept in the resulting BT particles [60]. For example, BT hierarchical microspheres were made by a topotactic transformation of $H_2Ti_2O_5 \cdot H_2O$ hierarchical microspheres with barium hydroxide in a water-ethanol mixture, as shown in Figure 2.9 [102].

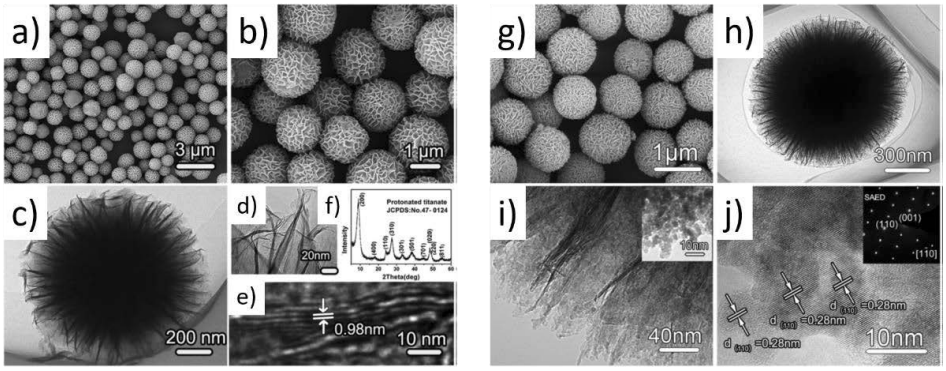

Figure 2.9: a-e) SEM and TEM images of solvothermally synthesized $H_2Ti_2O_5 \cdot H_2O$ hierarchical microspheres. g-j) SEM and TEM of solvothermally synthesized $BaTiO_3$ hierarchical microspheres by topotactic transformation of $H_2Ti_2O_5 \cdot H_2O$ hierarchical microspheres. Reproduced from ref. [102] with permission from The Royal Society of Chemistry.

2.3.3 Hydrothermal synthesis of $Sr_xBa_{1-x}Nb_2O_6$

Only one previous study of hydrothermal synthesis of SBN have previously been reported. $BaCl_2$, $SrCO_3$ and Nb_2O_5 were used as precursors, KOH as mineralizer (0.2 to 0.8 M) and reaction times and temperatures were ranging from 16 to 32 h and 220 and 260 °C, respectively [103]. Phase pure SBN was only obtained for high mineralizer concentrations, and the crystals grew "more perfectly" with increasing reaction time and temperature. The obtained particles were elongated (~1 μm) with a square cross section (~0.1 μm). This work was unsuccessfully reproduced in our group.

Materials related to SBN, either by chemistry (*e.g.* niobate-based oxides) or crystal structure (*e.g.* materials with tungsten bronze structure) have been produced with hydrothermal synthesis. For example, hydrothermal synthesis of the perovskites $NaNbO_3$ [104, 105], $KNbO_3$ [106] and their solid solution $K_xNa_{1-x}NbO_3$ [107] has been reported. Typically, Nb_2O_5 is used as precursor together with high NaOH and/or KOH mineralizer concentrations. A dissolution precipitation mechanism is proposed for the formation, where the solubility of dissolved Nb-species, and thus crystalline intermediate phases, is strongly dependent on the alkali metal-ion, further controlling the final polymorph in the case of $NaNbO_3$ [104] and particle size and composition for $K_xNa_{1-x}NbO_3$ [107]. $NaNbO_3$ has also been made using Nb-acid (see section 2.3.4) and NaOH with a microwave assisted hydrothermal synthesis route [108]. An orthorhombic phase was formed, as opposed to the monoclinic, and the particle size increased compared to using Nb_2O_5 in the same work. Other niobates, like $SrBi_2Nb_2O_9$ (Aurivillius structure) [109] and layered structured niobates [110-116] have also been synthesizes using either Nb_2O_5 or Nb-acid under alkaline conditions. A common feature for the synthesis of these niobium-based materials, is the need for mineralizers, especially when using Nb_2O_5 as a precursor. Furthermore, apparently small changes in the precursor chemistry, for example using NaOH instead of KOH, have a significant effect on the reaction pathway, and the size and polymorph of the final product.

Tetragonal tungsten bronze $PbNb_2O_6$ have been synthesized from lead acetate and Nb-acid, but an additional calcination-step was needed to obtain crystalline $PbNb_2O_6$ [117]. PbC_2O_4 or a pyrochlore phase depending on reaction conditions was reported to form during the hydrothermal reaction. A mixed metal oxide tetragonal tungsten bronze (reported as Mo(W)VNbO) has also been reported from a similar two-step method after calcination in N_2 atmosphere of the precipitates obtained from hydrothermal synthesis [118]. The prototypical WO_3 has also been synthesized by hydrothermal synthesis [119]. Furthermore, tungsten

bronzes on the form M_xWO_3 (M =Na, K) have been prepared. For M=Na, an additional calcination step after the hydrothermal synthesis was needed to obtain Na_xWO_3 [120] while for M=K, crystalline K_xWO_3 with rod or whisker shaped particles were obtained directly from hydrothermal synthesis by a reaction between WO_3 and KOH [121]. Hydrothermal synthesis of materials with a tungsten bronze structure is shown to be possible, but not always straight forward, and in some cases the tungsten bronze structure is only obtained after subsequent calcination of the precipitates obtained by the hydrothermal method.

2.3.4 Chemistry of Nb in aqueous solutions

The chemistry of Nb in aqueous solutions turned out to be important for the hydrothermal synthesis of SBN in this thesis, thus a brief introduction to this complex part of inorganic chemistry is reviewed.

Niobium is known to have a low solubility in water, thus only a few precursor for preparing aqueous niobium solutions exist [122, 123]. One of these is the ammonium niobate (V) oxalate hydrate, which can be dissolved in water, forming a solution of pH ~1 [123]. From this solution, the ill-defined Nb-acid, often denoted with the chemical formula $Nb_2O_5{\cdot}nH_2O$, can be precipitated out by the addition of ammonia solution, increasing the pH to ~11. This amorphous precipitate is reported to consist of clusters with a mix of NbO_4 tetrahedra and NbO_6 octahedra as shown by Fourier transform infrared spectroscopy (FT-IR) [124], while a mix of NbO_6, NbO_7 and NbO_8 is reported based on Raman spectroscopy [125]. The precipitate can be re-dispersed in water, and is reported to form stable complexes with malic acid at pH 7 [123], with oxalic acid down to pH 3.5 [126] and citric acid in combination with hydrogen peroxide at pH > 7.5 [127].

Niobium is known to form stable clusters, or polyoxoniobates (sub-group of polyoxometalates) [128], in alkaline solutions. Most common is the well-known Lindquist-ion or hexaniobate ($[Nb_6O_{19}]^{8-}$) [129, 130], but also decaniobate ($[Nb_{10}O_{28}]^{6-}$) [131, 132] and the α-Keggin ion ($[TNb_{12}O_{40}]^{16-}$, T = Ge, Si)[128] is reported, the first two shown in Figure 2.10. The hexa- and decaniobate clusters are built up by edge sharing NbO_6 octahedra and can be viewed as one and two edge-sharing superoctahedra, respectively. Both the hexa- and decaniobate ions have been synthesized from Nb-acid with a microwave assisted hydrothermal route [132]. The hexaniobate ion, with its anionic charge of 8, has the highest charge density (defined as anionic charge divided by total number of non-hydrogen atoms) of all known polyoxometalates [128]. It is known that alkali metal ions will coordinate to the Lindquist-ion, and form salt-complexes [128]. Furthermore, the solubility of these salt-complexes increases

going down the periodic table (solubility increases in the order Li<Na<K<Rb<Cs), which is a surprising trend, as the solubility normally increases with increasing size differences between anion and cation. For the hexaniobate-alkali metal salts the solubility should increase going up the periodic table, based on the simple size difference argument. This trend has shown to directly affect the hydrothermal synthesis of Nb-based perovskite oxides, as described in the previous section. No data about solubility trends for other elements than the alkali metals have been found. The degree of protonation of the hexaniobate is reported to change with the pH of the solution, where the triprotonated ($[H_3Nb_6O_{19}]^{5-}$), diprotonated ($[H_2Nb_6O_{19}]^{6-}$), monoprotonated ($[HNb_6O_{19}]^{7-}$) and un-protonated ($[Nb_6O_{19}]^{8-}$) clusters are dominant at pH values of 8, 10, 12 and 14, respectively [128].

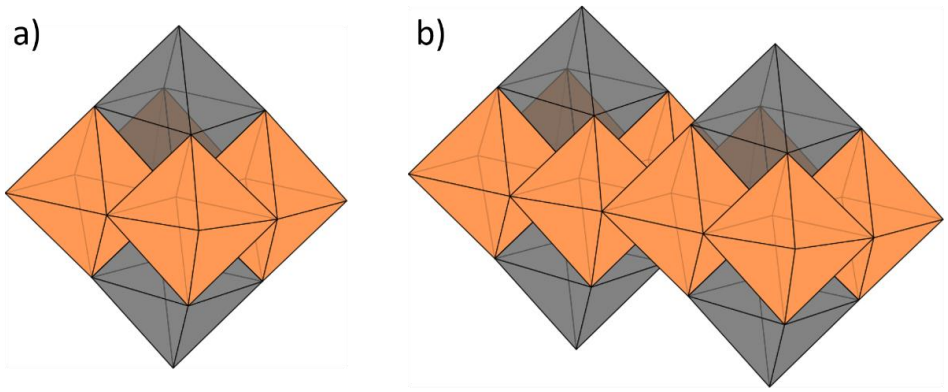

Figure 2.10: a) Schematic representation of the hexaniobate, or Lindquist-ion being a superoctahedra built up from 6 octahedra (in gray and orange). b) The decaniobate, which is two edge sharing Lindquist-ions. The octahedra here are simplified, not showing the atoms.

2.4 *In situ* diffraction studies during hydrothermal synthesis

Since the pioneering work by W. H. Bragg and W. L. Bragg [133], X-ray (and neutron) diffraction has been key for material characterization where the atomic arrangement can be deduced from their diffraction patterns. Furthermore, with the Rietveld method [134] powder diffraction has become an extremely powerful tool, where information on unit cell parameters, atomic positions, atom-site occupancies, thermal parameters and microstructural information can be obtained from diffraction patterns. Thus, diffraction is the workhorse within materials characterization, including *in situ* studies of hydrothermal synthesis.

2.4.1 Experimental setups and techniques

For *in situ* diffraction studies of hydrothermal synthesis, a probe that can penetrate through a reaction vessel that can withstand elevated temperatures and pressures is needed. In addition, rapid acquisition times of the data to have sufficient time resolution (the needed time resolution depends on the reaction kinetics) is desired. Here follows a description of selected key developments focused on the use of neutrons and X-rays for *in situ* diffraction experiments during hydrothermal synthesis. A more complete overview is found in the following review articles [135-138].

Experimental setups

Neutrons, reacting weakly with matter and having a low absorption cross-section compared to X-rays, were utilized by Polak *et al.* [139] to perform the first *in situ* diffraction studies during hydrothermal synthesis. They used an aluminum autoclave–like reaction cell mounted inside a furnace that was externally pressurized (could reach conditions up to 195 °C and 10 bar), to study the formation of zeolites and a layered calcium silicate hydrate with a time resolution of ~ 30 min. In addition to the low absorption cross-section of neutrons, some elements have negative scattering power, which was utilized by Walton *et al.* [140] to make a neutron-transparent reaction vessel (67.7 atom% Ti, 32.3 atom% Zr), greatly improving the quantitative and structural information that could be extracted from the collected diffraction patterns. Reaction conditions up to 250 °C and 20 bar could be reached with this setup. To improve the signal, the cell walls were thinned in the areas of ingoing and outgoing beam. With these *in situ* cells (and others developed for *in situ* neutron diffraction), reaction conditions very similar to that of a conventional autoclave hydrothermal synthesis can be investigated (reaction volume, temperatures, pressures and heating rates), and enough products for further *ex situ* characterization is produced.

The specialization and improvement of synchrotron facilities [141], generating high brilliance and high energy X-rays in addition to the development and improvement of 2D detectors have made it feasible to use X-rays for probing the reaction mechanism for hydrothermal synthesis. Norby *et al.* [142, 143] studied the formation of zeolites using a closed-end capillary design, heated with a hot air stream and pressurized with N_2. This setup was later significantly improved by Becker *et al.* [144] which used open-ended capillaries connected to a high pressure liquid chromatography (HPLC) pump with Swagelok fittings for hydrostatically pressurization and heated with a hot air stream, shown in Figure 2.11. This setup can reach temperatures and pressures of 450 °C and 250 bar (which allows for

performing supercritical hydrothermal reactions). This setup have proven very versatile, being used at several synchrotron facilities and adapted by several research groups performing conventional powder diffraction, small angle scattering (SAXS), total scattering and X-ray spectroscopy with high time resolution and good reproducibility [145]. The setup is limited to small reaction volumes, which makes direct comparison with conventional autoclave synthesis and further *ex situ* characterization of product (very little product can be obtained after experiments) challenging.

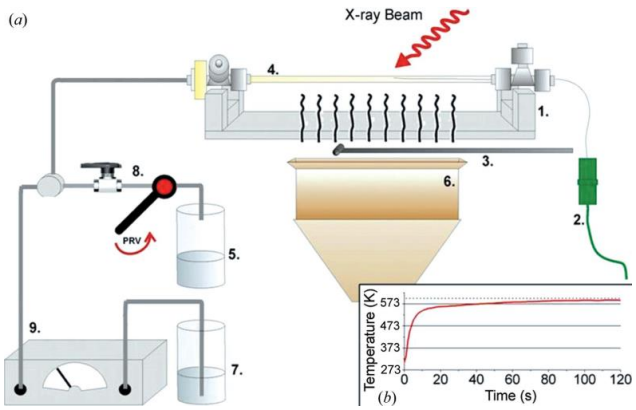

Figure 2.11: a) Schematic illustration of the open-ended capillary *in situ* setup, showing the capillary (4) heated with a hot air stream (6) and connected to a HPLC pump (9). b) A typical temperature profile for this setup, showing a rapid initial heating rate. Reproduced from ref. [144].

Reaction cells being closer to the conventional autoclaves have also been developed for the use of X-rays, but then mostly focused on performing energy dispersive diffraction. With the higher flux in a white X-ray beam compared with a monochromatic beam, larger and thicker reaction cells can be penetrated by the X-rays. In addition, since the diffracted beam is measured at a fixed diffraction angle as a function of energy, only a narrow opening/window is needed for the outgoing beam. The first of these cells were developed by Munn *et al.* [146] consisting of a steel autoclave with a polytetrafluoroethylene (PTFE) lining, heated with a solid copper block heating jacket reaching temperatures and pressures of 230 °C and 40 bar. Even though *in situ* energy dispersive X-ray diffraction allows for reaction conditions more similar to conventional autoclaves, data treatment for extracting structural information is significantly more complicated compared with conventional powder (angular dispersive) X-ray diffraction, limiting the use of these setups. More recently, a lightly modified Biotage Initiator microwave reactor was used to study the formation of titanates

during microwave assisted hydrothermal synthesis with X-ray total scattering [147]. This setup can be used up to 300 °C and 20 bar [148], and gives direct comparison with *ex situ* experiments performed in the same reactor, and is not limited to energy dispersive diffraction.

Experimental techniques

Conventional powder diffraction (PXRD for X-rays) is the most utilized experimental technique for studying the formation and growth during hydrothermal synthesis. With the use of Rietveld refinement [134], detailed information about the average crystalline structure of materials can be obtained, in addition to revealing nucleation pathways (assuming crystalline intermediates) and reaction kinetics [72]. The limitation of this technique is that it only includes the Bragg diffraction (elastic coherent scattering), which only arises in crystalline materials, making the accurate description of nanosized and amorphous materials without a long range crystalline structure challenging at best. Furthermore, even though average crystallite sizes can be obtained, which often can be correlated with particle sizes for nanosized materials, no direct measurement of particle size, size distribution or shape is obtained.

Total scattering and pair distribution function (PDF) takes advantage of the Bragg scattering (for crystalline materials) *and* the diffuse scattering (inelastic coherent scattering, which is removed in background subtractions for Rietveld refinement) and can thus give "structural" information of amorphous and nanosized (being the local short range structure), as well as crystalline materials [149]. There is no major difference between experiments for conventional powder diffraction and total scattering experiments, except the need to measure over a large Q-space (achieved with high energy radiation and/or short sample to detector distance), and an accurate description of the real background. Similar to powder diffraction, only limited information about crystallite sizes, size distributions and shapes can be obtained for total scattering and PDF analysis.

If information about particle size, size distributions and particle shapes is the main interest for the *in situ* studies, small angle scattering (SAXS/SANS) is a good alternative to the previously mentioned techniques [150]. Experimentally it is not significantly different from powder diffraction or total scattering, other than placing the detector far away from the sample to resolve the small angle scattering. SAXS/SANS in combination with total scattering or powder diffraction will give complementary insight on a wide range of length scales, from particle size and shape, to the average/local arrangement of atoms, potentially for both crystalline and amorphous phases.

In addition to the scattering techniques, spectroscopy techniques, like X-ray absorption near edge structure (XANES) and extended X-ray absorption fine structure (EXAFS) can also give valuable insight about reaction mechanics during hydrothermal synthesis [151]. By measuring the absorption as a function of energy close to the absorption edge of an element in the sample, information about local structure (*e.g.* coordination number/environment) and oxidation states can be obtained.

In combinations, as separate [152] or simultaneous experiments [151, 152], these techniques can give a complete view of the reaction mechanisms during the hydrothermal synthesis, from the pre- and early nucleation stages, through intricate formation pathways all the way to detailed structural information and particle size and morphology of the final product, as shown in Figure 2.12. In addition, the combination of X-rays and neutrons, where neutrons complement X-rays with the ability to locate light atoms in the presence of heavy atoms (*e.g.* hydrogen) further expands our toolbox for understanding the hydrothermal synthesis.

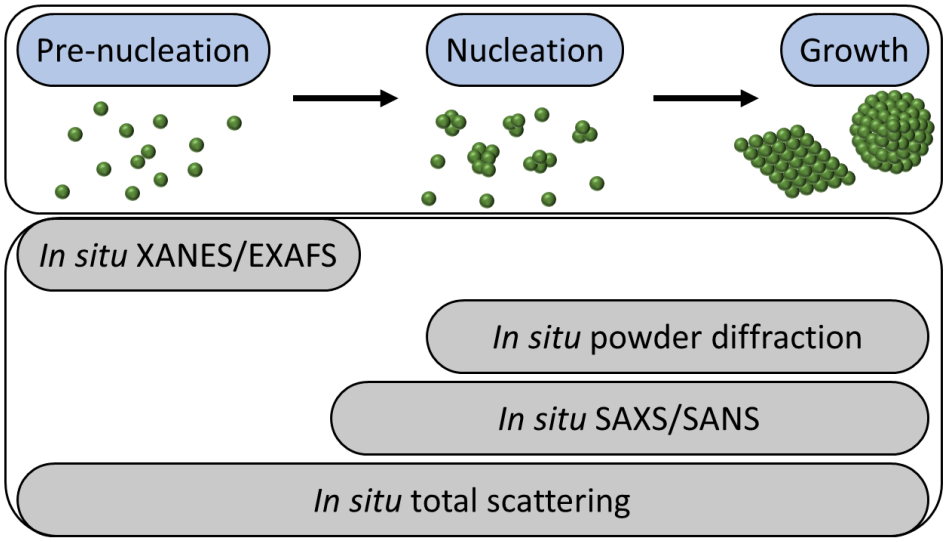

Figure 2.12: Schematic illustration of different steps during a hydrothermal reaction, going from the pre-nucleation clusters all the way to final crystalline particles. The most suited *in situ* technique for gaining insight about the different steps is also indicated.

2.4.2 Achievements based on *in situ* diffraction

In this section, a wide range of reported *in situ* experiments are presented in Table 2.1, with material, *in situ* technique and main findings highlighted. This is followed by a more detailed description of selected key achievements based on *in situ* diffraction.

Table 2.1: An overview of selected *in situ* hydrothermal experiments from literature, focusing on oxide materials and their formation and growth. The experiments are listed chronologically (from top to bottom) and divided into binary and ternary oxides.

Material	Year	*In situ* technique	Type of cation(s)	Main findings
Fe_3O_4 [153]	2009	PXRD/SAXS	Transition metal	Formation of amorphous nanoclusters prior to crystallization by dissolution and precipitation mechanism.
CeO_2 [154]	2010	PXRD	Lanthanide	Two growth regimes: Early growth limited by surface reactions and changes into diffusion limited growth for larger particle sizes.
ZrO_2 [154]	2010	PXRD	Transition metal	Growth reported to be diffusion limited.
SnO_2 [80]	2012	PDF	Post-transition metal	Formation from clustering of octahedrally coordinated monomeric Sn^{4+} pre-nucleation clusters. Diffusion limited growth observed.
CeO_2 [155]	2012	PDF/PXRD	Lanthanide	Transformation of octahedrally coordinated dimeric Ce^{4+} pre-nucleation clusters.
γ-Fe_2O_3 [74]	2014	PXRD	Transition metal	Temperature dependent growth kinetics. Going from diffusion limited to nucleation limited growth with decreasing temperature.
ZnO [156]	2014	PXRD	Transition metal	Dissolution and precipitation from crystalline precursor. Depletion rate of precursor is highly temperature dependent.
γ-Fe_2O_3 [157]	2014	PDF	Transition metal	Octahedrally coordinated Fe^{3+} in polymer-like pre-nucleation clusters assembles into amorphous particles before final crystallization.
WO_3 [81]	2014	PDF	Transition metal	Structural change in pre-nucleation clusters from mix of corner- and edge-sharing to more corner sharing octahedrally coordinated W^{6+}.
TiO_2 [158]	2015	PDF	Transition metal	Solid-state phase transition from amorphous precursor consisting of anatase-like pre-nucleation clusters.
ZrO_2 [159]	2016	PDF	Transition metal	Edge-shared tetramer chains undergo different structural changes in water and methanol, forming two different polymorphs respectively.
TiO_2 [84]	2017	PXRD	Transition metal	Growth mechanism changed from Ostwald ripening to oriented attachment by the use of surfactant.

Table 2.1: Continued.

TiO_2 [150] [a]	2018	SAXS	Transition metal	Pre-nucleation clusters attach in an anisotropic arrangement forming rods, before further increasing the fractal dimension.
WO_3 [119]	2019	PDF	Transition metal	α-Keggin pre-nucleation cluster undergo different structural changes in water and oleylamine, forming different polymorphs respectively.
$BaTiO_3$ [160]	2000	ND	Alkali earth/ transition metal	Formation by dissolution and precipitation mechanism from a solid oxide precursor (TiO_2 anatase).
γ-Bi_2MoO_6 [151, 161]	2009	PXRD/ XANES	Post-transition/ transition metal	Formation through a Bi_2O_3 intermediate by reaction with tetrahedral MoO_4^{2-} species. Growth limited by diffusion.
$NaNbO_3$ [104]	2009	PXRD [b]	Alkali/ transition metal	Formation by dissolution and precipitation mechanism from a solid oxide precursor (Nb_2O_5). Final polymorph affected by intermediates.
$LiFePO_4$ [162]	2011	PXRD	Alkali/transition metal	Formation by dissolution and precipitation. Growth limited by diffusion.
$LiFePO_4$ [163]	2011	PXRD	Alkali/transition metal	Formation by dissolution and precipitation through an unknown crystalline intermediate.
$LiCoO_2$ [164]	2011	PXRD	Alkali/transition metal	Formation by dissolution precipitation, being rate limited by the dissolution of CoOOH.
$LiMn_2O_4$ [165]	2014	PXRD	Alkali/transition metal	Formation through a set of crystalline intermediates, where $LiMn_2O_4$ also is an intermediate for the more stable Mn_3O_4.
$BaTiO_3$ [92]	2014	PXRD	Alkali earth/ transition metal	Formation by dissolution and precipitation. Change in growth mechanism between sub- and supercritical conditions.
$ZnWO_4$ [166]	2016	PDF	Transition/ transition metal	Formation through local restructuring of Tourné-type sandwich pre-nucleation clusters. Growth by oriented attachment.
$CoSb_2O_4$ [73]	2016	PXRD	Transition/ post-transition metal	Formation by dissolution and precipitation. Growth limited by diffusion.
$K_xN_{1-x}NbO_3$ [106]	2017	PXRD	Alkali/transition metal	Formation by dissolution and precipitating. Solubility of Nb-species influenced by K/Na-ratio further influencing intermediates.
$BaTiO_3$ [167] [c]	2019	PXRD	Alkali earth/ transition metal	Formation by dissolution and precipitate. Temperature dependent growth mechanism with a complexed Ti-precursor.
$Sr_xBa_{1-x}Nb_2O_6$ [c]	2020	PXRD	Alkali earth/ transition metal	Formation by dissolution and precipitating. Solubility of Nb-species influenced by Sr/Ba-ratio further influencing growth mechanisms.

[a] No crystallization of TiO_2 was observed, but assumed to happen at a later stage.

[b] Energy dispersive X-ray powder diffraction.

[c] This work.

Expose formation mechanisms of $BaTiO_3$

In 1988 Hertl [168] proposed a topotactic transformation of TiO_2 (anatase) particles into BT under hydrothermal reaction with $Ba(OH)_2$ forming TiO_2@$BaTiO_3$ core-shell intermediate particles based on modeling of the reaction kinetics. For similar reaction conditions, Eckert *et al.* [88] proposed a dissolution-precipitation mechanism, where TiO_2 dissolves and together with Ba^{2+} in solution precipitates as BT. Experimental evidence are today strongly suggesting that a dissolution-precipitations mechanism is most likely. Especially the *in situ* neutron diffraction studies by Walton *et al.* [160, 169, 170] showing a decrease in the TiO_2 fraction before the appearance of BT suggest that TiO_2 dissolve before BT forms. Later Philippot *et al.* [92] used *in situ* X-ray diffraction to study the crystallization of BT in a water-ethanol mixture from barium and titanium isopropoxide precursors, showing no evidence for a topotactic transformation. Furthermore, transmission electron microscopy (TEM) studies of quenched samples at various reaction times prepared from amorphous $TiO_2{\cdot}xH_2O$ and $Ba(OH)_2$ showed only separate amorphous $TiO_2{\cdot}xH_2O$ and $BaTiO_3$ particles, no core-shell particles, further supporting the dissolution-precipitation mechanism.

Revealing oriented attachment mechanism of TiO_2 nanoparticles

In the work by Dalod *et al.* [84], a one-pot synthesis and surface functionalization of TiO_2 (anatase) nanoparticles were studied with *in situ* X-ray diffraction using an adapted version [106] of the Becker *et al.* [144] capillary setup. A significant narrowing of the [001]-diffraction line was observed suggesting anisometric crystallite shapes. Time resolved and orientation dependent crystallite sizes were extracted using Rietveld refinement, and revealed that the growth kinetics in the [001]-direction could be modeled with an oriented attachment model, while the growth kinetics in [100]-direction could be modeled according to an Ostwald ripening mechanism. These findings were further supported with scanning electron microscopy (SEM), TEM and density functional theory (DFT).

Intricate nucleation pathway and polymorph control for $NaNbO_3$

Skjærvø *et al.* [105] studied the formation of $NaNbO_3$ at supercritical conditions (423 °C and 250 bar) with a high time resolution (0.1 s), showing an intricate nucleation pathway from a crystalline Nb_2O_5 precursor in a highly alkaline solution (9 M NaOH). The dissolution of Nb_2O_5 and formation of $NaNbO_3$ took only 5 s from start to end, but 4 - 5 transient crystalline intermediate phases were observed in this short time period. Understanding and controlling the formation of the intermediates have proven important for controlling the polymorphs of $NaNbO_3$ [104] and stoichiometry of the $K_{1-x}Na_xNbO_3$ (KNN) solid solution [107].

Pre-nucleation clusters

Tungsten is known to form polyoxotungstates in solutions [171], and recently *in situ* total scattering have shown the importance of these pre-nucleation clusters for the formation of WO_3 nanoparticles. With *in situ* total scattering, Juelsholt *et al.* [119] showed how the same polyoxotungstates (α-Keggin structure) were present in the precursor solutions using both water and oleylamine, but different polyoxotungstates were stabilized during the reaction in the two solvents. This directly influenced the atomic structure of the formed WO_3 nanoparticles, as a locally disordered structure was obtained with reactions in water, and a perfectly ordered structure in oleylamine. Similar insight to the pre-nucleation clusters have also been obtained for other binary oxides, like CeO_2 [155], ZrO_2 [159], SnO_2 [80] and γ-Fe_2O_3 [157].

References

1. Rabe, K. M., Dawber, M., Lichtensteiger, C., Ahn, C. H. and Triscone, J.-M., in *Physics of ferroelectrics: a modern perspective*, Springer Berlin Heidelberg, Berlin, Heidelberg, 1-30, (2007). DOI: 10.1007/978-3-540-34591-6_1

2. Damjanovic, D. Ferroelectric, dielectric and piezoelectric properties of ferroelectric thin films and ceramics, *Reports on Progress in Physics* **61**, 1267, (1998). DOI: 10.1088/0034-4885/61/9/002

3. Halasyamani, P. S. and Poeppelmeier, K. R. Noncentrosymmetric oxides, *Chemistry of Materials* **10**, 2753-2769, (1998). DOI: 10.1021/cm980140w

4. Barone, P. and Picozzi, S. Mechanisms and origin of multiferroicity, *Comptes Rendus Physique* **16**, 143-152, (2015). DOI: 10.1016/j.crhy.2015.01.009

5. Lilienblum, M., Lottermoser, T., Manz, S., Selbach, S. M., Cano, A. and Fiebig, M. Ferroelectricity in the multiferroic hexagonal manganites, *Nature Physics* **11**, 1070-1073, (2015). DOI: 10.1038/nphys3468

6. Acosta, M., Novak, N., Rojas, V., Patel, S., Vaish, R., Koruza, J., Rossetti, G. A. and Rödel, J. $BaTiO_3$-based piezoelectrics: fundamentals, current status, and perspectives, *Applied Physics Reviews* **4**, 041305, (2017). DOI: 10.1063/1.4990046

7. Scott, J. F. Ferroelectrics go bananas, *Journal of Physics: Condensed Matter* **20**, 021001, (2008).

8. Scott, J. F. Applications of modern ferroelectrics, *Science* **315**, 954-959, (2007). DOI: 10.1126/science.1129564

9. Panda, P. K. and Sahoo, B. PZT to lead free piezo ceramics: a review, *Ferroelectrics* **474**, 128-143, (2015). DOI: 10.1080/00150193.2015.997146

10. Rödel, J., Jo, W., Seifert, K. T. P., Anton, E.-M., Granzow, T. and Damjanovic, D. Perspective on the development of lead-free piezoceramics, *Journal of the American Ceramic Society* **92**, 1153-1177, (2009). DOI: 10.1111/j.1551-2916.2009.03061.x

11. Labbe, P. Tungsten oxides, tungsten bronzes and tungsten bronze-type structures, *Key Engineering Materials* **68**, 293-300, (1992).

12. Zhu, X., Fu, M., Stennett, M. C., Vilarinho, P. M., Levin, I., Randall, C. A., Gardner, J., Morrison, F. D. and Reaney, I. M. A crystal-chemical framework for relaxor versus normal ferroelectric behavior in tetragonal tungsten bronzes, *Chemistry of Materials* **27**, 3250-3261, (2015). DOI: 10.1021/acs.chemmater.5b00072

13. Bernard, D., Pannetier, J. and Lucas, J. Ferroelectric and antiferroelectric materials with pyrochlore structure, *Ferroelectrics* **21**, 429-431, (1978). DOI: 10.1080/00150197808237288

14. Moure, A. Review and perspectives of aurivillius structures as a lead-free piezoelectric system, *Applied Sciences* **8**, (2018). DOI: 10.3390/app8010062

15. Rödel, J., Webber, K. G., Dittmer, R., Jo, W., Kimura, M. and Damjanovic, D. Transferring lead-free piezoelectric ceramics into application, *Journal of the European Ceramic Society* **35**, 1659-1681, (2015). DOI: 10.1016/j.jeurceramsoc.2014.12.013

16. Varghese, J., Whatmore, R. W. and Holmes, J. D. Ferroelectric nanoparticles, wires and tubes: synthesis, characterisation and applications, *Journal of Materials Chemistry C* **1**, 2618-2638, (2013). DOI: 10.1039/C3TC00597F

17. Rørvik, P. M., Grande, T. and Einarsrud, M.-A. One-dimensional nanostructures of ferroelectric perovskites, *Advanced Materials* **23**, 4007-4034, (2011). DOI: 10.1002/adma.201004676

18. Bowen, C. R., Kim, H. A., Weaver, P. M. and Dunn, S. Piezoelectric and ferroelectric materials and structures for energy harvesting applications, *Energy & Environmental Science* **7**, 25-44, (2014). DOI: 10.1039/C3EE42454E

19. Chen, X., Xu, S., Yao, N. and Shi, Y. 1.6 V nanogenerator for mechanical energy harvesting using PZT nanofibers *Nano Letters* **10**, 2133-2137, (2010). DOI: 10.1021/nl100812k

20. Koka, A., Zhou, Z. and Sodano, H. A. Vertically aligned $BaTiO_3$ nanowire arrays for energy harvesting, *Energy & Environmental Science* **7**, 288-296, (2014). DOI: 10.1039/C3EE42540A

21. He, Y., Wang, Z., Hu, X., Cai, Y., Li, L., Gao, Y., Zhang, X., Huang, Z., Hu, Y. and Gu, H. Orientation-dependent piezoresponse and high-performance energy harvesting of lead-free $(K,Na)NbO_3$ nanorod arrays, *RSC Advances* **7**, 16908-16915, (2017). DOI: 10.1039/C7RA01359K

22. He, Y., Zhang, T., Zheng, W., Wang, R., Liu, X., Xia, Y. and Zhao, J. Humidity sensing properties of $BaTiO_3$ nanofiber prepared via electrospinning, *Sensors and Actuators B: Chemical* **146**, 98-102, (2010). DOI: 10.1016/j.snb.2010.02.030

23. Han, G., Cao, S. and Lin, B. UV photocatalytic activity for water decomposition of $Sr_xBa_{1-x}Nb_2O_6$ nanocrystals with different components and morphologies, *Journal of Chemistry* **2017**, 6, (2017). DOI: 10.1155/2017/2163608

24. Blázquez-Castro, A., García-Cabañes, A. and Carrascosa, M. Biological applications of ferroelectric materials, *Applied Physics Reviews* **5**, 041101, (2018). DOI: 10.1063/1.5044472

25. Yun, W. S., Urban, J. J., Gu, Q. and Park, H. Ferroelectric properties of individual barium titanate nanowires investigated by scanned probe microscopy, *Nano Letters* **2**, 447-450, (2002). DOI: 10.1021/nl015702g

26. Sæterli, R., Rørvik, P. M., You, C. C., Holmestad, R., Tybell, T., Grande, T., van Helvoort, A. T. J. and Einarsrud, M.-A. Polarization control in ferroelectric $PbTiO_3$ nanorods, *Journal of Applied Physics* **108**, 124320, (2010). DOI: 10.1063/1.3525593

27. Kay, H. F. and Vousden, P. Symmetry changes in barium titanate at low temperatures and their relation to its ferroelectric properties, *The London, Edinburgh, and Dublin Philosophical Magazine and Journal of Science* **40**, 1019-1040, (1949). DOI: 10.1080/14786444908561371

28. Poon, K. K., Wurm, M. C., Evans, D. M., Einarsrud, M.-A., Lutz, R. and Glaum, J. Biocompatibility of $(Ba,Ca)(Zr,Ti)O_3$ piezoelectric ceramics for bone replacement materials, *Journal of Biomedical Materials Research Part B: Applied Biomaterials* **n/a**, 1-9, (2019). DOI: 10.1002/jbm.b.34477

29. Li, Y., Dai, X., Bai, Y., Liu, Y., Wang, Y., Liu, O., Yan, F., Tang, Z., Zhang, X. and Deng, X. Electroactive $BaTiO_3$ nanoparticle-functionalized fibrous scaffolds enhance osteogenic differentiation of mesenchymal stem cells, *International journal of nanomedicine* **12**, 4007-4018, (2017). DOI: 10.2147/IJN.S135605

30. Singh, G., Bhaumik, I., Ganesamoorthy, S., Bhatt, R., Karnal, A. K., Tiwari, V. S. and Gupta, P. K. Electro-caloric effect in $0.45BaZr_{0.2}Ti_{0.8}O_3$-$0.55Ba_{0.7}Ca_{0.3}TiO_3$ single crystal, *Applied Physics Letters* **102**, 082902, (2013). DOI: 10.1063/1.4793213

31. Alluri, N. R., Saravanakumar, B. and Kim, S.-J. Flexible, hybrid piezoelectric film $(BaTi_{(1-x)}Zr_xO_3)$ /PVDF nanogenerator as a self-powered fluid velocity sensor, *ACS Applied Materials & Interfaces* **7**, 9831-9840, (2015). DOI: 10.1021/acsami.5b01760

32. Zhang, Q., Sun, H., Wang, X., Zhang, Y. and Li, X. Strong photoluminescence and piezoelectricity properties in Pr-doped $Ba(Zr_{0.2}Ti_{0.8})O_3$–$(Ba_{0.7}Ca_{0.3})TiO_3$ ceramics: Influence of concentration and microstructure, *Journal of the European Ceramic Society* **34**, 1439-1444, (2014). DOI: 10.1016/j.jeurceramsoc.2013.11.028

33. Dupuy, A. D., Kodera, Y. and Garay, J. E. Unprecedented electro-optic performance in lead-free transparent ceramics, *Advanced Materials* **28**, 7970-7977, (2016). DOI: 10.1002/adma.201600947

34. Momma, K. and Izumi, F. VESTA 3 for three-dimensional visualization of crystal, volumetric and morphology data, *Journal of Applied Crystallography* **44**, 1272-1276, (2011). DOI: 10.1107/S0021889811038970

35. Jamieson, P. B., Abrahams, S. C. and Bernstein, J. L. Ferroelectric tungsten bronze - type crystal structures. I. Barium strontium niobate $Ba_{0.27}Sr_{0.75}Nb_2O_{5.78}$, *The Journal of Chemical Physics* **48**, 5048-5057, (1968). DOI: 10.1063/1.1668176

36. Podlozhenov, S., Graetsch, H. A., Schneider, J., Ulex, M., Wohlecke, M. and Betzler, K. Structure of strontium barium niobate $Sr_xBa_{1-x}Nb_2O_6$ (SBN) in the composition range 0.32 <= *x* <= 0.82, *Acta Crystallographica Section B* **62**, 960-965, (2006). DOI: 10.1107/S0108768106038869

37. Paściak, M., Ondrejkovic, P., Kulda, J., Vaněk, P., Drahokoupil, J., Steciuk, G., Palatinus, L., Welberry, T. R., Fischer, H. E., Hlinka, J. and Buixaderas, E. Local structure of relaxor ferroelectric $Sr_xBa_{1-x}Nb_2O_6$ from a pair distribution function analysis, *Physical Review B* **99**, 104102, (2019). DOI: 10.1103/PhysRevB.99.104102

38. Ngai, K. L. and Reinecke, T. L. Model of the ferroelectric phase transition in the tetragonal tungsten-bronze-structure ferroelectrics, *Physical Review Letters* **38**, 74-77, (1977). DOI: 10.1103/PhysRevLett.38.74

39. Nikasch, C. and Göbbels, M. Phase relations and lattice parameters in the system SrO–BaO–Nb_2O_5 focusing on SBN ($Sr_xBa_{1-x}Nb_2O_6$), *Journal of Crystal Growth* **269**, 324-332, (2004). DOI: 10.1016/j.jcrysgro.2004.04.037

40. Schneck, J., Toledano, J. C., Whatmore, R. and Ainger, F. W. Incommensurate phases in ferroelectric tetragonal tungsten bronzes, *Ferroelectrics* **36**, 327-330, (1981). DOI: 10.1080/00150198108218114

41. Prokert, F., Balagurov, A. M. and Savenko, B. N. Investigation of the incommensurate modulated structure of $Sr_{0.7}Ba_{0.3}Nb_2O_6$ by neutron diffraction, *Ferroelectrics* **79**, 307-310, (1988). DOI: 10.1080/00150198808229456

42. Guo, R., Bhalla, A. S., Burns, G. and Dacol, F. H. Studies on annealing and quenching of strontium barium niobate (SBN) single crystals: A-site cation ordering-disordering effect, *Ferroelectrics* **93**, 397-405, (1989). DOI: 10.1080/00150198908017376

43. Aamlid, S. S., Selbach, M. S. and Grande, T. The effect of cation disorder on ferroelectric properties of $Sr_xBa_{1-x}Nb_2O_6$ tungsten bronzes, *Materials* **12**, (2019). DOI: 10.3390/ma12071156

44. Olsen, G. H., Selbach, S. M. and Grande, T. On the energetics of cation ordering in tungsten-bronze-type oxides, *Physical Chemistry Chemical Physics* **17**, 30343-30351, (2015). DOI: 10.1039/C5CP05119C

45. Olsen, G. H., Aschauer, U., Spaldin, N. A., Selbach, S. M. and Grande, T. Origin of ferroelectric polarization in tetragonal tungsten-bronze-type oxides, *Physical Review B* **93**, 180101, (2016). DOI: 10.1103/PhysRevB.93.180101

46. López-Conesa, L., Rebled, J. M., Ruiz-Caridad, A., Torres-Pardo, A., Ruiz-González, M. L., González-Calbet, J. M., Dezanneau, G., Estradé, S. and Peiró, F. Cation disorder in $Sr_{0.67}Ba_{0.33}Nb_2O_6$ assessed by aberration corrected STEM, *Results in Materials* **3**, 100038, (2019). DOI: 10.1016/j.rinma.2019.100038

47. Lukasiewicz, T., Swirkowicz, M. A., Dec, J., Hofman, W. and Szyrski, W. Strontium–barium niobate single crystals, growth and ferroelectric properties, *Journal of Crystal Growth* **310**, 1464-1469, (2008). DOI: 10.1016/j.jcrysgro.2007.11.233

48. Zhang, J., Wang, G., Gao, F., Mao, C., Cao, F. and Dong, X. Influence of Sr/Ba ratio on the dielectric, ferroelectric and pyroelectric properties of strontium barium niobate ceramics, *Ceramics International* **39**, 1971-1976, (2013). DOI: 10.1016/j.ceramint.2012.08.048

49. Lenzo, P. V., Spencer, E. G. and Ballman, A. A. Electro - optic coefficients of ferroelectric strontium barium niobate, *Applied Physics Letters* **11**, 23-24, (1967). DOI: 10.1063/1.1754944

50. Ewbank, M. D., Neurgaonkar, R. R., Cory, W. K. and Feinberg, J. Photorefractive properties of strontium - barium niobate, *Journal of Applied Physics* **62**, 374-380, (1987). DOI: 10.1063/1.339807

51. Ford, J. E., Ma, J., Fainman, Y., Lee, S. H., Taketomi, Y., Bize, D. and Neurgaonkar, R. R. Multiplex holography in strontium barium niobate with applied field, *Journal of the Optical Society of America A* **9**, 1183-1192, (1992). DOI: 10.1364/JOSAA.9.001183

52. Ketchel, B. P., Heid, C. A., Wood, G. L., Miller, M. J., Mott, A. G., Anderson, R. J. and Salamo, G. J. Three-dimensional color holographic display, *Applied Optics* **38**, 6159-6166, (1999). DOI: 10.1364/AO.38.006159

53. Glass, A. M. Investigation of the electrical properties of $Sr_{1-x}Ba_xNb_2O_6$ with Special reference to pyroelectric detection, *Journal of Applied Physics* **40**, 4699-4713, (1969). DOI: 10.1063/1.1657277

54. Tang, H., Tang, X.-G., Li, M.-D., Liu, Q.-X. and Jiang, Y.-P. Pyroelectric energy harvesting capabilities and electrocaloric effect in lead-free $Sr_xBa_{1-x}Nb_2O_6$ ferroelectric ceramics, *Journal of Alloys and Compounds* **791**, 1038-1045, (2019). DOI: 10.1016/j.jallcom.2019.03.385

55. Dayong Fan, Ruifeng Chong, Fengtao Fan, Xiuli Wang, Can Li and Feng, Z. A tetragonal tungsten bronze-type photocatalyst: ferro-paraelectric phase transition and photocatalysis, *Chinese Journal of Catalysis* **37**, 1257-1262, (2016). DOI: 10.1016/S1872-2067(15)61126-3

56. Kolodiazhnyi, T., Sakurai, H., Isobe, M., Matsushita, Y., Forbes, S., Mozharivskyj, Y., Munsie, T. J. S., Luke, G. M., Gurak, M. and Clarke, D. R. Superconductivity and crystal structural origins of the metal-insulator transition in $Ba_{6-x}Sr_xNb_{10}O_{30}$ tetragonal tungsten bronzes, *Physical Review B* **92**, 214508, (2015). DOI: 10.1103/PhysRevB.92.214508

57. Lee, S., Wilke, R. H. T., Trolier-McKinstry, S., Zhang, S. and Randall, C. A. $Sr_xBa_{1-x}Nb_2O_{6-\delta}$ ferroelectric-thermoelectrics: crystal anisotropy, conduction mechanism, and power factor, *Applied Physics Letters* **96**, 031910, (2010). DOI: 10.1063/1.3291563

58. Rabenau, A. The role of hydrothermal synthesis in preparative chemistry, *Angewandte Chemie International Edition in English* **24**, 1026-1040, (1985). DOI: 10.1002/anie.198510261

59. Byrappa, K. and Yoshimura, M., in *Handbook of Hydrothermal Technology*, William Andrew Publishing, Oxford, Second Edition, Chp. 2, 51-73, (2013). DOI: 10.1016/B978-0-12-375090-7.00002-5

60. Einarsrud, M.-A. and Grande, T. 1D oxide nanostructures from chemical solutions, *Chemical Society Reviews* **43**, 2187-2199, (2014). DOI: 10.1039/C3CS60219B

61. Meng, L.-Y., Wang, B., Ma, M.-G. and Lin, K.-L. The progress of microwave-assisted hydrothermal method in the synthesis of functional nanomaterials, *Materials Today Chemistry* **1-2**, 63-83, (2016). DOI: 10.1016/j.mtchem.2016.11.003

62. Thanh, N. T. K., Maclean, N. and Mahiddine, S. Mechanisms of nucleation and growth of nanoparticles in solution, *Chemical Reviews* **114**, 7610-7630, (2014). DOI: 10.1021/cr400544s

63. Bøjesen, E. D. and Iversen, B. B. The chemistry of nucleation, *CrystEngComm* **18**, 8332-8353, (2016). DOI: 10.1039/C6CE01489E

64. Desarnaud, J., Derluyn, H., Carmeliet, J., Bonn, D. and Shahidzadeh, N. Hopper growth of salt crystals, *The Journal of Physical Chemistry Letters* **9**, 2961-2966, (2018). DOI: 10.1021/acs.jpclett.8b01082

65. Polte, J. Fundamental growth principles of colloidal metal nanoparticles – a new perspective, *CrystEngComm* **17**, 6809-6830, (2015). DOI: 10.1039/C5CE01014D

66. Andreassen, J.-P. and Lewis, A. E., in *New Perspectives on Mineral Nucleation and Growth: From Solution Precursors to Solid Materials*, Springer International Publishing, Cham, Switzerland, 137-154, (2017). DOI: 10.1007/978-3-319-45669-0_7

67. Berg, W. F. and Bragg, W. L. Crystal growth from solutions, *Proceedings of the Royal Society of London. Series A - Mathematical and Physical Sciences* **164**, 79-95, (1938). DOI: 10.1098/rspa.1938.0006

68. Shaddel, S., Ucar, S., Andreassen, J.-P. and Østerhus, S. W. Engineering of struvite crystals by regulating supersaturation – correlation with phosphorus recovery, crystal morphology and process efficiency, *Journal of Environmental Chemical Engineering* **7**, 102918, (2019). DOI: 10.1016/j.jece.2019.102918

69. Gornitz, V., in *Mineralogy*, Springer US, Boston, MA, 469-473, (1981). DOI: 10.1007/0-387-30720-6_130

70. Wagner, C. Theorie der Alterung von Niederschlägen durch Umlösen (Ostwald-Reifung), *Zeitschrift für Elektrochemie, Berichte der Bunsengesellschaft für physikalische Chemie* **65**, 581-591, (1961). DOI: 10.1002/bbpc.19610650704

71. Avrami, M. Kinetics of phase change. I General theory, *The Journal of Chemical Physics* **7**, 1103-1112, (1939). DOI: 10.1063/1.1750380

72. Peterson, K. M., Heaney, P. J. and Post, J. E. A kinetic analysis of the transformation from akaganeite to hematite: an *in situ* time-resolved X-ray diffraction study, *Chemical Geology* **444**, 27-36, (2016). DOI: doi.org/10.1016/j.chemgeo.2016.09.017

73. Nørby, P., Roelsgaard, M., Søndergaard, M. and Iversen, B. B. Hydrothermal synthesis of $CoSb_2O_4$: *in situ* powder X-ray diffraction, crystal structure, and electrochemical properties, *Crystal Growth & Design* **16**, 834-841, (2016). DOI: 10.1021/acs.cgd.5b01421

74. Andersen, H. L., Jensen, K. M. Ø., Tyrsted, C., Bøjesen, E. D. and Christensen, M. Size and size distribution control of γ-Fe_2O_3 nanocrystallites: an *in situ* study, *Crystal Growth & Design* **14**, 1307-1313, (2014). DOI: 10.1021/cg401815a

75. Eltzholtz, J. R., Tyrsted, C., Jensen, K. M. O., Bremholm, M., Christensen, M., Becker-Christensen, J. and Iversen, B. B. Pulsed supercritical synthesis of anatase TiO_2 nanoparticles in a water-isopropanol mixture studied by *in situ* powder X-ray diffraction, *Nanoscale* **5**, 2372-2378, (2013). DOI: 10.1039/C3NR33127J

76. Milán, G. A., Millier, B., Ritchie, A., Bryan, C., Vinette, S., Wielens, B. and White, M. A. Bismuth crystals: preparation and measurement of thermal and electrical properties, *Journal of Chemical Education* **90**, 1675-1680, (2013). DOI: 10.1021/ed4001409

77. Libbrecht, K. G. Physical dynamics of ice crystal growth, *Annual Review of Materials Research* **47**, 271-295, (2017). DOI: 10.1146/annurev-matsci-070616-124135

78. Gebauer, D. and Cölfen, H. Prenucleation clusters and non-classical nucleation, *Nano Today* **6**, 564-584, (2011). DOI: 10.1016/j.nantod.2011.10.005

79. Gebauer, D., Kellermeier, M., Gale, J. D., Bergström, L. and Cölfen, H. Pre-nucleation clusters as solute precursors in crystallisation, *Chemical Society Reviews* **43**, 2348-2371, (2014). DOI: 10.1039/C3CS60451A

80. Jensen, K. M., Christensen, M., Juhas, P., Tyrsted, C., Bojesen, E. D., Lock, N., Billinge, S. J. and Iversen, B. B. Revealing the mechanisms behind SnO_2 nanoparticle formation and growth during hydrothermal synthesis: an *in situ* total scattering study, *J Am Chem Soc* **134**, 6785-6792, (2012). DOI: 10.1021/ja300978f

81. Saha, D., Jensen, K. M. Ø., Tyrsted, C., Bøjesen, E. D., Mamakhel, A. H., Dippel, A.-C., Christensen, M. and Iversen, B. B. *In situ* total X-ray scattering study of WO_3 nanoparticle formation under hydrothermal conditions, *Angewandte Chemie International Edition* **53**, 3667-3670, (2014). DOI: 10.1002/anie.201311254

82. Ivanov, V. K., Fedorov, P. P., Baranchikov, A. Y. and Osiko, V. V. Oriented attachment of particles: 100 years of investigations of non-classical crystal growth, *Russian Chemical Reviews* **83**, 1204, (2014). DOI: 10.1070/RCR4453

83. Penn, R. L. and Banfield, J. F. Morphology development and crystal growth in nanocrystalline aggregates under hydrothermal conditions: insights from titania, *Geochimica et Cosmochimica Acta* **63**, 1549-1557, (1999). DOI: 10.1016/S0016-7037(99)00037-X

84. Dalod, A. R. M., Grendal, O. G., Skjærvø, S. L., Inzani, K., Selbach, S. M., Henriksen, L., van Beek, W., Grande, T. and Einarsrud, M.-A. Controlling oriented attachment and *in situ* functionalization of TiO_2 nanoparticles during hydrothermal synthesis with APTES, *The Journal of Physical Chemistry C* **121**, 11897-11906, (2017). DOI: 10.1021/acs.jpcc.7b02604

85. Niederberger, M. and Cölfen, H. Oriented attachment and mesocrystals: non-classical crystallization mechanisms based on nanoparticle assembly, *Physical Chemistry Chemical Physics* **8**, 3271-3287, (2006). DOI: 10.1039/B604589H

86. Cölfen, H. and Antonietti, M. Mesocrystals: inorganic superstructures made by highly parallel crystallization and controlled alignment, *Angewandte Chemie International Edition* **44**, 5576-5591, (2005). DOI: 10.1002/anie.200500496

87. Modeshia, D. R. and Walton, R. I. Solvothermal synthesis of perovskites and pyrochlores: crystallisation of functional oxides under mild conditions, *Chemical Society Reviews* **39**, 4303-4325, (2010). DOI: 10.1039/B904702F

88. Eckert, J. O., Hung-Houston, C. C., Gersten, B. L., Lencka, M. M. and Riman, R. E. Kinetics and mechanisms of hydrothermal synthesis of barium titanate, *Journal of the American Ceramic Society* **79**, 2929-2939, (1996). DOI: 10.1111/j.1151-2916.1996.tb08728.x

89. Page, K., Proffen, T., Niederberger, M. and Seshadri, R. Probing local dipoles and ligand structure in $BaTiO_3$ nanoparticles, *Chemistry of Materials* **22**, 4386-4391, (2010). DOI: 10.1021/cm100440p

90. Sun, W., Pang, Y., Li, J. and Ao, W. Particle coarsening II: growth kinetics of hydrothermal $BaTiO_3$, *Chemistry of Materials* **19**, 1772-1779, (2007). DOI: 10.1021/cm061741n

91. Adam, J., Klein, G. and Lehnert, T. Hydroxyl content of $BaTiO_3$ nanoparticles with varied size, *Journal of the American Ceramic Society* **96**, 2987-2993, (2013). DOI: 10.1111/jace.12404

92. Philippot, G., Jensen, K. M. O., Christensen, M., Elissalde, C., Maglione, M., Iversen, B. B. and Aymonier, C. Coupling *in situ* synchrotron radiation with ex situ spectroscopy characterizations to study the formation of $Ba_{1-x}Sr_xTiO_3$ nanoparticles in supercritical fluids, *Journal of Supercritical Fluids* **87**, 111-117, (2014). DOI: 10.1016/j.supflu.2013.12.009

93. Cai, W., Rao, T., Wang, A., Hu, J., Wang, J., Zhong, J. and Xiang, W. A simple and controllable hydrothermal route for the synthesis of monodispersed cube-like barium titanate nanocrystals, *Ceramics International* **41**, 4514-4522, (2015). DOI: 10.1016/j.ceramint.2014.11.146

94. Ma, Q., Mimura, K. and Kato, K. Tuning shape of barium titanate nanocubes by combination of oleic acid/tert-butylamine through hydrothermal process, *Journal of Alloys and Compounds* **655**, 71-78, (2016). DOI: 10.1016//j.jallcom.2015.09.156

95. Ma, Q. and Kato, K. Anisotropy in morphology and crystal structure of $BaTiO_3$ nanoblocks, *Materials & Design* **107**, 378-385, (2016). DOI: 10.1016/j.matdes.2016.06.065

96. Bogicevic, C., Thorner, G., Karolak, F., Haghi-Ashtiani, P. and Kiat, J.-M. Morphogenesis mechanisms in the solvothermal synthesis of $BaTiO_3$ from titanate nanorods and nanotubes, *Nanoscale* **7**, 3594-3603, (2015). DOI: 10.1039/C4NR06266C

97. Bao, N., Shen, L., Gupta, A., Tatarenko, A., Srinivasan, G. and Yanagisawa, K. Size-controlled one-dimensional monocrystalline $BaTiO_3$ nanostructures, *Applied Physics Letters* **94**, 253109, (2009). DOI: 10.1063/1.3159817

98. Urban, J. J., Yun, W. S., Gu, Q. and Park, H. Synthesis of single-crystalline perovskite nanorods composed of barium titanate and strontium titanate, *Journal of the American Chemical Society* **124**, 1186-1187, (2002). DOI: 10.1021/ja017694b

99. Yang, L., Wang, Y., Wang, Y., Wang, X., Guo, X. and Han, G. Synthesis of single-crystal $Ba_{1-x}Sr_xTiO_3$ (x = 0–1) dendrites via a simple hydrothermal method, *Journal of Alloys and Compounds* **500**, L1-L5, (2010). DOI: 10.1016/j.jallcom.2010.03.196

100. Bao, N., Shen, L., Srinivasan, G., Yanagisawa, K. and Gupta, A. Shape-controlled monocrystalline ferroelectric barium titanate nanostructures: from nanotubes and nanowires to ordered nanostructures, *The Journal of Physical Chemistry C* **112**, 8634-8642, (2008). DOI: 10.1021/jp802055a

101. Krzmanc, M. M., Klement, D., Jancar, B. and Suvorov, D. Hydrothermal conditions for the formation of tetragonal $BaTiO_3$ particles from potassium titanate and barium salt, *Ceramics International* **41**, 15128-15137, (2015). DOI: 10.1016/j.ceramint.2015.08.085

102. Chen, C.-K., Zhao, S.-X., Lu, Q.-L., Luo, K., Zhang, X.-H. and Nan, C.-W. Topochemical synthesis and photocatalytic activity of 3D hierarchical $BaTiO_3$ microspheres constructed from crystal-axis-oriented nanosheets, *Dalton Transactions* **46**, 5017-5024, (2017). DOI: 10.1039/C7DT00724H

103. Xia, A., Ding, Q., Miao, H.-y. and TAN, G.-q. Study on hydrothermal synthesis of strontium barium niobate powders, *Electronic Components Materials* **26**, 37, (2007).

104. Modeshia, D. R., Darton, R. J., Ashbrook, S. E. and Walton, R. I. Control of polymorphism in $NaNbO_3$ by hydrothermal synthesis, *Chemical Communications*, 68-70, (2009). DOI: 10.1039/B814601B

105. Skjærvø, S. L., Wells, K. H., Sommer, S., Vu, T.-D., Tolchard, J. R., van Beek, W., Grande, T., Iversen, B. B. and Einarsrud, M.-A. Rationalization of hydrothermal synthesis of $NaNbO_3$ by rapid *in situ* time-resolved synchrotron X-ray diffraction, *Crystal Growth & Design* **18**, 770-774, (2018). DOI: 10.1021/acs.cgd.7b01192

106. Skjærvø, S. L., Sommer, S., Nørby, P., Bøjesen, E. D., Grande, T., Iversen, B. B. and Einarsrud, M.-A. Formation mechanism and growth of $MNbO_3$, M=K, Na by *in situ* X-ray diffraction, *Journal of the American Ceramic Society* **100**, 3835-3842, (2017). DOI: 10.1111/jace.14932

107. Skjærvø, S. L., Wells, K. H., van Beek, W., Grande, T. and Einarsrud, M.-A. Kinetics during hydrothermal synthesis of nanosized $K_xNa_{1-x}NbO_3$, *CrystEngComm* **20**, 6795-6802, (2018). DOI: 10.1039/C8CE01178H

108. Paula, A. J., Zaghete, M. A., Longo, E. and Varela, J. A. Microwave-assisted hydrothermal synthesis of structurally and morphologically controlled sodium niobates by using niobic acid as a precursor, *European Journal of Inorganic Chemistry* **2008**, 1300-1308, (2008). DOI: 10.1002/ejic.200701138

109. Xie, H., Wang, K., Jiang, Y., Zhao, Y. and Wang, X. Hydrothermal synthesis and characterization of $SrBi_2Nb_2O_9$ nanoplates, *Synthesis and Reactivity in Inorganic, Metal-Organic, and Nano-Metal Chemistry* **45**, 80-85, (2015). DOI: 10.1080/15533174.2013.818686

110. Uchida, S., Inoue, Y., Fujishiro, Y. and Sato, T. Hydrothermal synthesis of $K_4Nb_6O_{17}$, *Journal of Materials Science* **33**, 5125-5129, (1998). DOI: 10.1023/a:1004411315906

111. Liu, J.-F., Li, X.-L. and Li, Y.-D. Synthesis and characterization of nanocrystalline niobates, *Journal of Crystal Growth* **247**, 419-424, (2003). DOI: 10.1016/S0022-0248(02)02015-8

112. Zhang, G., He, F., Zou, X., Gong, J., Tu, H., Zhang, H., Zhang, Q. and Liu, Y. Hydrothermal synthesis and photocatalytic property of KNb_3O_8 with nanometer leaf-like network, *Journal of Alloys and Compounds* **427**, 82-86, (2007). DOI: 10.1016/j.jallcom.2006.03.023

113. Zhang, G., He, F., Zou, X., Gong, J. and Zhang, H. Hydrothermal preparation and photocatalytic properties of sheet-like nanometer niobate $K_4Nb_6O_{17}$, *Journal of Physics and Chemistry of Solids* **69**, 1471-1474, (2008). DOI: 10.1016/j.jpcs.2007.10.095

114. Qu, W., Chen, F., Zhao, B. and Zhang, J. Preparation and visible light photocatalytic performance of methylene blue intercalated $K_4Nb_6O_{17}$, *Journal of Physics and Chemistry of Solids* **71**, 35-41, (2010). DOI: 10.1016/j.jpcs.2009.10.005

115. Cao, Y., Jiang, L., Guo, H. and Zheng, Q. Nano-layered $K_4Nb_6O_{17}$ as an efficient photocatalyst for methyl orange degradation: Influence of solution pH and surface-dispersed gold nanoparticles, *Journal of Molecular Catalysis A: Chemical* **383–384**, 209-216, (2014). DOI: 10.1016/j.molcata.2013.12.009

116. Liu, X., Que, W. and Kong, L. B. Hydrothermal synthesis of bamboo-shaped nanosheet KNb_3O_8 with enhanced photocatalytic activity, *Journal of Alloys and Compounds* **627**, 117-122, (2015). DOI: 10.1016/j.jallcom.2014.12.115

117. Lu, C.-H. and Chyi, N. Fabrication of fine lead metaniobate powder using hydrothermal processes, *Materials Letters* **29**, 101-105, (1996). DOI: 10.1016/S0167-577X(96)00134-6

118. Botella, P., Solsona, B., Garcia-Gonzalez, E., Gonzalez-Calbet, J. M. and Lopez Nieto, J. M. The hydrothermal synthesis of tetragonal tungsten bronze-based catalysts for the selective oxidation of hydrocarbons, *Chemical Communications*, 5040-5042, (2007). DOI: 10.1039/B711228A

119. Juelsholt, M., Lindahl Christiansen, T. and Jensen, K. M. Ø. Mechanisms for tungsten oxide nanoparticle formation in solvothermal synthesis: from polyoxometalates to crystalline materials, *The Journal of Physical Chemistry C* **123**, 5110-5119, (2019). DOI: 10.1021/acs.jpcc.8b12395

120. Luo, J., Liu, J., Shi, F., Xu, Q., Jiang, Y., Liu, G. and Hu, Z., Dalian, China, 2013.

121. Yang, X.-G., Li, C., Mo, M.-S., Zhan, J.-h., Yu, W.-C., Yan, Y. and Qian, Y.-T. Growth of $K_{0.4}WO_3$ whiskers via a pressure-relief-assisted hydrothermal process, *Journal of Crystal Growth* **249**, 594-599, (2003). DOI: 10.1016/S0022-0248(02)02323-0

122. Livage, J., Henry, M. and Sanchez, C. Sol-gel chemistry of transition metal oxides, *Progress in Solid State Chemistry* **18**, 259-341, (1988). DOI: 10.1016/0079-6786(88)90005-2

123. Mokkelbost, T., Andersen, Ø., Strøm, R. A., Wiik, K., Grande, T. and Einarsrud, M.-A. High-temperature proton-conducting $LaNbO_4$-based materials: powder synthesis by spray pyrolysis, *Journal of the American Ceramic Society* **90**, 3395-3400, (2007). DOI: 10.1111/j.1551-2916.2007.01904.x

124. Nakajima, K., Baba, Y., Noma, R., Kitano, M., N. Kondo, J., Hayashi, S. and Hara, M. $Nb_2O_5{\cdot}nH_2O$ as a heterogeneous catalyst with water-tolerant Lewis acid sites, *Journal of the American Chemical Society* **133**, 4224-4227, (2011). DOI: 10.1021/ja110482r

125. Jehng, J. M. and Wachs, I. E. Structural chemistry and Raman spectra of niobium oxides, *Chemistry of Materials* **3**, 100-107, (1991). DOI: 10.1021/cm00013a025

126. Jehng, J.-M. and Wachs, I. E. Niobium oxide solution chemistry, *Journal of Raman Spectroscopy* **22**, 83-89, (1991). DOI: 10.1002/jrs.1250220207

127. Narendar, Y. and Messing, G. L. Synthesis, decomposition and crystallization characteristics of peroxo–citrato–niobium: an aqueous niobium precursor, *Chemistry of Materials* **9**, 580-587, (1997). DOI: 10.1021/cm960407w

128. Nyman, M. Polyoxoniobate chemistry in the 21st century, *Dalton Transactions* **40**, 8049-8058, (2011). DOI: 10.1039/C1DT10435G

129. Lindqvist, I. The structure of the hexaniobate ion in $7Na_2O{\cdot}6Nb_2O_5{\cdot}32H_2O$, *Arkiv for kemi* **5**, 247-250, (1952).

130. Friis, H. and Casey, W. H. Niobium is highly mobile as a polyoxometalate ion during natural weathering, *The Canadian Mineralogist* **56**, 905-912, (2018). DOI: 10.3749/canmin.1800058

131. Aureliano, M., Ohlin, C. A., Vieira, M. O., Marques, M. P. M., Casey, W. H. and Batista de Carvalho, L. A. E. Characterization of decavanadate and decaniobate solutions by Raman spectroscopy, *Dalton Transactions* **45**, 7391-7399, (2016). DOI: 10.1039/C5DT04176G

132. Rambaran, M. A., Pascual-Borràs, M. and Ohlin, C. A. Microwave synthesis of alkali-free hexaniobate, decaniobate, and hexatantalate polyoxometalate ions, *European Journal of Inorganic Chemistry* **2019**, 3913-3918, (2019). DOI: 10.1002/ejic.201900750

133. Bragg, W. H. and Bragg, W. L. The reflection of X-rays by crystals, *Proceedings of the Royal Society of London. Series A, Containing Papers of a Mathematical and Physical Character* **88**, 428-438, (1913). DOI: 10.1098/rspa.1913.0040

134. Rietveld, H. A profile refinement method for nuclear and magnetic structures, *Journal of Applied Crystallography* **2**, 65-71, (1969). DOI: doi:10.1107/S0021889869006558

135. Walton, R. I. and O'Hare, D. Watching solids crystallise using powder diffraction, *Chemical Communications*, 2283-2291, (2000). DOI: 10.1039/B007795J

136. Sun, Y. and Ren, Y. *In situ* synchrotron X-say techniques for real-time probing of colloidal nanoparticle synthesis, *Particle & Particle Systems Characterization* **30**, 399-419, (2013). DOI: 10.1002/ppsc.201300033

137. Jensen, K. M., Tyrsted, C., Bremholm, M. and Iversen, B. B. *In situ* studies of solvothermal synthesis of energy materials, *ChemSusChem* **7**, 1594-1611, (2014). DOI: 10.1002/cssc.201301042

138. Wu, S., Li, M. and Sun, Y. *In situ* synchrotron X-ray characterization shining light on the nucleation and growth kinetics of colloidal nanoparticles, *Angewandte Chemie International Edition* **0**, (2019). DOI: 10.1002/anie.201900690

139. Polak, E., Munn, J., Barnes, P., Tarling, S. E. and Ritter, C. Time-resolved neutron diffraction analyses of hydrothermal syntheses using a novel autoclave cell, *Journal of Applied Crystallography* **23**, 258-262, (1990). DOI: 10.1107/S0021889890002473

140. Walton, R. I., Francis, R. J., Halasyamani, P. S., O' Hare, D., Smith, R. I., Done, R. and Humphreys, R. J. Novel apparatus for the in situ study of hydrothermal crystallizations using time-resolved neutron diffraction, *Review of Scientific Instruments* **70**, 3391-3396, (1999). DOI: 10.1063/1.1149925

141. Thompson, A., Attwood, D., Gullikson, E., Howells, M., Kin, K.-J., Kirz, J., Kortright, J., Lindau, I., Liu, Y., Pianetta, P., Robinson, A., Scofield, J., Underwood, J., Williams, G. and Winick, H., *X-ray data booklet*, Center for X-ray optics and advanced light source, Lawrence Berkley National Laboratory, University of California, Berkley, 2009.

142. Norby, P., Nørlund Christensen, A. and Hanson, J. C. *In situ* studies of zeolite syntheses using powder diffraction methods. Crystallization of "instant zeolite A" powder and synthesis of CoAPO-5, *Studies in Surface Science and Catalysis* **84**, 179-186, (1994). DOI: 10.1016/S0167-2991(08)64112-9

143. Norby, P. Hydrothermal conversion of ceolites: an *in situ* synchrotron X-ray powder diffraction study, *Journal of the American Chemical Society* **119**, 5215-5221, (1997). DOI: 10.1021/ja964245g

144. Becker, J., Bremholm, M., Tyrsted, C., Pauw, B., Jensen, K. M. O., Eltzholt, J., Christensen, M. and Iversen, B. B. Experimental setup for *in situ* X-ray SAXS/WAXS/PDF studies of the formation and growth of nanoparticles in near- and supercritical fluids, *Journal of Applied Crystallography* **43**, 729-736, (2010). DOI: 10.1107/S0021889810014688

145. Andersen Henrik, L., Bøjesen Espen, D., Birgisson, S., Christensen, M. and Iversen Bo, B. Pitfalls and reproducibility of *in situ* synchrotron powder X-ray diffraction studies of solvothermal nanoparticle formation, *Journal of Applied Crystallography* **51**, 526-540, (2018). DOI: 10.1107/S1600576718003552

146. Munn, J., Barnes, P., Häusermann, D., Axon, S. A. and Klinowski, J. *In-situ* studies of the hydrothermal synthesis of zeolites using synchrotron energy-dispersive X-ray diffraction, *Phase Transitions* **39**, 129-134, (1992). DOI: 10.1080/01411599208203476

147. Tominaka, S., Yamada, H., Hiroi, S., Kawaguchi, S. I. and Ohara, K. Lepidocrocite-type titanate formation from isostructural prestructures under hydrothermal reactions: observation by synchrotron X-ray total scattering analyses, *ACS Omega* **3**, 8874-8881, (2018). DOI: 10.1021/acsomega.8b01693

148. Ohara, K., Tominaka, S., Yamada, H., Takahashi, M., Yamaguchi, H., Utsuno, F., Umeki, T., Yao, A., Nakada, K., Takemoto, M., Hiroi, S., Tsuji, N. and Wakihara, T. Time-resolved pair distribution function analysis of disordered materials on beamlines BL04B2 and BL08W at SPring-8, *Journal of synchrotron radiation* **25**, (2018). DOI: 10.1107/S1600577518011232

149. Billinge, S. J. L. and Kanatzidis, M. G. Beyond crystallography: the study of disorder, nanocrystallinity and crystallographically challenged materials with pair distribution functions, *Chemical Communications*, 749-760, (2004). DOI: 10.1039/B309577K

150. Hinterberger, S., Tscheließnig, R. and Jungbauer, A. Anisotropic assembly during heat-up: the early stage hydrothermal synthesis of TiO_2 from a complexed precursor, *ChemNanoMat* **4**, 1121-1124, (2018). DOI: 10.1002/cnma.201800326

151. Kongmark, C., Martis, V., Rubbens, A., Pirovano, C., Löfberg, A., Sankar, G., Bordes-Richard, E., Vannier, R.-N. and Van Beek, W. Elucidating the genesis of Bi_2MoO_6 catalyst by combination of synchrotron radiation experiments and Raman scattering, *Chemical Communications*, 4850-4852, (2009). DOI: 10.1039/B907935A

152. Tyrsted, C., Pauw, B. R., Jensen, K. M. Ø., Becker, J., Christensen, M. and Iversen, B. B. Watching nanoparticles form: an *in situ* (small-/wide-angle X-ray scattering/total scattering) study of the growth of yttria-stabilised zirconia in supercritical fluids, *Chemistry - A European Journal* **18**, 5759-5766, (2012). DOI: 10.1002/chem.201102826

153. Bremholm, M., Felicissimo, M. and Iversen, B. B. Time-resolved in situ synchrotron X-ray study and large-scale production of magnetite nanoparticles in supercritical water, *Angewandte Chemie International Edition* **48**, 4788-4791, (2009). DOI: 10.1002/anie.200901048

154. Tyrsted, C., Becker, J., Hald, P., Bremholm, M., Pedersen, J. S., Chevallier, J., Cerenius, Y., Iversen, S. B. and Iversen, B. B. *In-situ* synchrotron radiation study of formation and growth of crystalline $Ce_xZr_{1-x}O_2$ nanoparticles synthesized in supercritical water, *Chemistry of Materials* **22**, 1814-1820, (2010). DOI: 10.1021/cm903316s

155. Tyrsted, C., Jensen, K. M. O., Bøjesen, E. D., Lock, N., Christensen, M., Billinge, S. J. L. and Brummerstedt Iversen, B. Understanding the formation and evolution of ceria nanoparticles under hydrothermal conditions, *Angewandte Chemie* **124**, 9164-9167, (2012). DOI: 10.1002/ange.201204747

156. Bøjesen, E. D., Jensen, K. M. Ø., Tyrsted, C., Lock, N., Christensen, M. and Iversen, B. B. *In situ* powder diffraction study of the hydrothermal synthesis of ZnO nanoparticles, *Crystal Growth & Design* **14**, 2803-2810, (2014). DOI: 10.1021/cg5000606

157. Jensen, K. M. Ø., Andersen, H. L., Tyrsted, C., Bøjesen, E. D., Dippel, A.-C., Lock, N., Billinge, S. J. L., Iversen, B. B. and Christensen, M. Mechanisms for iron oxide formation under hydrothermal conditions: an *in situ* total scattering study, *ACS Nano* **8**, 10704-10714, (2014). DOI: 10.1021/nn5044096

158. Mi, J.-L., Jensen, K. M. Ø., Tyrsted, C., Bremholm, M. and Iversen, B. B. *In situ* total X-ray scattering study of the formation mechanism and structural defects in anatase TiO_2 nanoparticles under hydrothermal conditions, *CrystEngComm* **17**, 6868-6877, (2015). DOI: 10.1039/C5CE00544B

159. Dippel, A.-C., Jensen, K. M. O., Tyrsted, C., Bremholm, M., Bojesen, E. D., Saha, D., Birgisson, S., Christensen, M., Billinge, S. J. L. and Iversen, B. B. Towards atomistic understanding of polymorphism in the solvothermal synthesis of ZrO_2 nanoparticles, *Acta Crystallographica Section A* **72**, 645-650, (2016). DOI: 10.1107/S2053273316012675

160. Walton, R. I., Smith, R. I., Millange, F., Clark, I. J., Sinclair, D. C. and O'Hare, D. An *in situ* time-resolved neutron diffraction study of the hydrothermal crystallisation of barium titanate, *Chemical Communications*, 1267-1268, (2000). DOI: 10.1039/b003386n

161. Kongmark, C., Coulter, R., Cristol, S., Rubbens, A., Pirovano, C., Löfberg, A., Sankar, G., van Beek, W., Bordes-Richard, E. and Vannier, R.-N. A comprehensive scenario of the crystal growth of γ-Bi_2MoO_6 catalyst during hydrothermal synthesis, *Crystal Growth & Design* **12**, 5994-6003, (2012). DOI: 10.1021/cg301070e

162. Chen, J., Bai, J., Chen, H. and Graetz, J. *In situ* hydrothermal synthesis of $LiFePO_4$ studied by synchrotron X-ray diffraction, *The Journal of Physical Chemistry Letters* **2**, 1874-1878, (2011). DOI: 10.1021/jz2008209

163. Jensen, K., Christensen, M., Tyrsted, C. and Brummerstedt Iversen, B. Real-time synchrotron powder X-ray diffraction study of the antisite defect formation during sub- and supercritical synthesis of $LiFePO_4$ and $LiFe_{1-x}Mn_xPO_4$ nanoparticles, *Journal of Applied Crystallography* **44**, 287-294, (2011). DOI: 10.1107/S0021889811006522

164. Jensen, K. M. Ø., Christensen, M., Tyrsted, C., Bremholm, M. and Iversen, B. B. Structure, size, and morphology control of nanocrystalline lithium cobalt oxide, *Crystal Growth & Design* **11**, 753-758, (2011). DOI: 10.1021/cg101271d

165. Birgisson, S., Jensen, K. M. O., Christiansen, T. L., von Bulow, J. F. and Iversen, B. B. *In situ* powder X-ray diffraction study of the hydro-thermal formation of $LiMn_2O_4$ nanocrystallites, *Dalton Transactions* **43**, 15075-15084, (2014). DOI: 10.1039/C4DT01307G

166. Bøjesen, E. D., Jensen, K. M. Ø., Tyrsted, C., Mamakhel, A., Andersen, H. L., Reardon, H., Chevalier, J., Dippel, A.-C. and Iversen, B. B. The chemistry of $ZnWO_4$ nanoparticle formation, *Chemical Science* **7**, 6394-6406, (2016). DOI: 10.1039/C6SC01580H

167. Grendal, O., Blichfeld, A., Skjærvø, S., van Beek, W., Selbach, S., Grande, T. and Einarsrud, M.-A. Facile low temperature hydrothermal synthesis of $BaTiO_3$ nanoparticles studied by *in situ* X-ray diffraction, *Crystals* **8**, 253-264, (2018).

168. Hertl, W. Kinetics of barium titanate synthesis, *Journal of the American Ceramic Society* **71**, 879-883, (1988). DOI: 10.1111/j.1151-2916.1988.tb07540.x

169. Walton, R. I., Millange, F., Smith, R. I., Hansen, T. C. and O'Hare, D. Real time observation of the hydrothermal crystallization of barium titanate using *in situ* neutron powder diffraction, *Journal of the American Chemical Society* **123**, 12547-12555, (2001). DOI: 10.1021/ja011805p

170. Walton, R. I., Norquist, A., Smith, R. I. and O'Hare, D. Recent results from the in situ study of hydrothermal crystallisations using time-resolved X-ray and neutron diffraction methods, *Faraday Discussions* **122**, 331-341, (2002). DOI: 10.1039/b200990k

171. Pope, M. T. and Müller, A. Polyoxometalate chemistry: an old field with new dimensions in several disciplines, *Angewandte Chemie International Edition in English* **30**, 34-48, (1991). DOI: 10.1002/anie.199100341

3 Experimental

3.1 Hydrothermal synthesis of nanocrystalline $BaTiO_3$

3.1.1 Precursor preparation

For the *in situ* hydrothermal synthesis of $BaTiO_3$ (BT) two different titanium precursors were compared, one amorphous Ti-hydroxide precipitate and one citric acid stabilized Ti complex which was based on the work by Wang *et al.* [1] on $PbTiO_3$. The chemicals were used without further treatment.

For the amorphous Ti-hydroxide precipitate (Ti-slurry), titanium (IV) isopropoxide (TIP, Sigma-Aldrich, ≥ 97 %) was mixed with distilled water under continues stirring, immediately forming a white amorphous precipitate with a Ti concentration of 0.3 M. Then barium nitrate (Sigma-Aldrich, ≥ 99 %) was dissolved in a 1:1 molar ratio with Ti under continuous stirring. The slurry was pre-cooled in an ice-water bath before the pH was raised to > 14 by adding potassium hydroxide pellets (KOH, Sigma-Aldrich, 80 %) while the slurry was continuously cooled in the ice-water bath to dissipate the heat from dissolution of KOH. For the experiments were surfactants were used (ethylene glycol, EG, Sigma-Aldrich > 99 % or sodium dodecylbenzenesulfonate, SDBS, Sigma-Aldrich, technical grade), the surfactants were added before KOH in a 1:1 mole ratio with Ti.

The citric acid stabilized Ti complex (Ti-CAsol) solution was prepared by complexing TIP in a 1.5 M citric acid solution (CA, Sigma-Aldrich, ≥ 99 %) at 60 °C under continuous stirring, forming a clear 0.43 M Ti complex solution with a pH of ~1. The pH was then raised to 5 – 6 by adding aqueous ammonia solution (Sigma-Aldrich, 25 wt % solution), before dissolving barium nitrate in a 1:1 mole ratio with Ti under continuous stirring, forming a

clear solution. The pH was raised to > 14 by adding KOH, resulting in the formation of a white amorphous precipitate. For the experiments with surfactants (EG and SDBS), these were added as described above for Ti-slurry. For both the Ti-slurry and Ti-CAsol, stock solutions were prepared prior to the beam times were the experiments were conducted, and for each *in situ* experiment, approximately 5 mL of finished BT precursor solution was prepared. Table 3.1 shows an overview of the synthesis parameters for the conducted *in situ* experiments.

Table 3.1: Sample names, temperature, X-ray wavelength and time resolution for the *in situ* XRD experiments of $BaTiO_3$. Which surfactant used is indicated for the specific experiments. The set pressure was 200 bar for all experiments.

Name	Temperature [°C]	EG	SDBS	Wavelength [Å] [a]	Time resolution [s] [b]
Ti-slurry-100	100	no	no	0.7242	0.1
Ti-slurry-125	125	no	no	0.7242	0.1
Ti-slurry-150	150	no	no	0.7242	0.1
Ti-slurry-EG	125	yes	no	0.7242	0.1
Ti-slurry-SDBS	125	no	yes	0.7762	0.1
Ti-CAsol-100	100	no	no	0.7129	10
Ti-CAsol-125	125	no	no	0.7129	5
Ti-CAsol-150	150	no	no	0.7129	5
Ti-CAsol-EG	125	yes	no	0.7242	5
Ti-CAsol-SDBS	125	no	yes	0.7129	5

[a] Experiments conducted at different beam times, therefore varying wavelength.

[b] Time for data collection. Optimized for the different reaction speeds.

3.1.2 Characterization

***In situ* synchrotron X-ray diffraction**

Three different beam times using the Swiss-Norwegian Beamlines (SNBL, BM01) at the European Synchrotron and Radiation Facility (ESRF), Grenoble, France, was used for performing the *in situ* X-ray diffraction experiments. All experiments were performed in transmission mode, using the PILATUS@SNBL platform [2] with a Pilatus 2M detector [3]. The *in situ* setup is based on Becker *et al.* [4] with open-ended capillary design, and adopted in our group by Dr. Susanne Linn Skjærvø [5-7], and a schematic of the setup is shown in Figure 3.1. The reaction vessel was a single crystal sapphire capillary (~6 cm long, 1.15 ± 0.1 mm outer and 0.8 ± 0.08 mm inner diameter, provided by Crytur, Turnov, Czech Republic). The

capillary was connected to a high pressure liquid chromatography (HPLC) pump (Shimadzu LC-10ADVP, Shimadzu Corp., Kyoto, Japan) with Swagelok fittings, capable of providing a hydrostatic pressure up to 350 bar. Approximately 2 cm of the middle of the capillary was heated with a hot air stream using a heat blower (Leister Le Mini 800, Leister Tech. Kaegiswil, Switzerland) capable of reaching 750 °C. The heat blower was heated to the set point temperature while directed away from the capillary and moved into position by a step motor at the start of the experiment. The set point temperature was reached within 15 to 20 s after the heater was in position, and heat profiles and description of the temperature calibration are included in Appendix A. The capillaries were filled with the precursor using a plastic syringe.

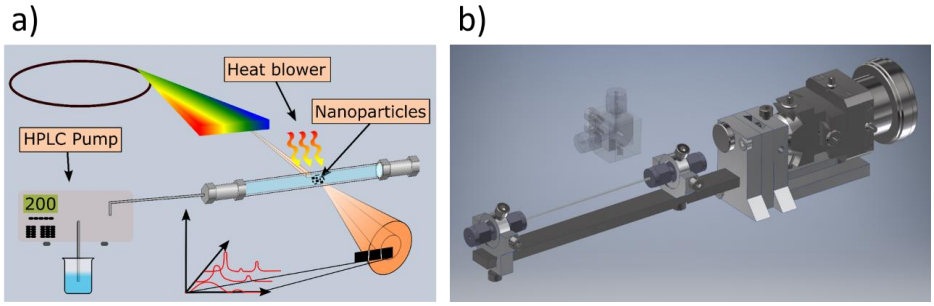

Figure 3.1: a) Schematic illustration of the setup used for the *in situ* synchrotron XRD experiments. A single crystal sapphire capillary used as reaction vessel was heated with a hot air-stream and pressurized with a HPLC pump. b) The *in situ* reaction cell with option for straight or elbow Swagelok connections. Drawn with Autodesk Inventor® LT™ by Anders Bank Blichfeld.

The data were treated by masking parasitic regions (*e.g.* shadow from beam stopper and diffraction spots from the capillary) and integrated from 2D images to 1D diffractograms using *Bubble* (v. 2017.10.23) [2] which uses the *Python* library *pyFAI* [8] for the azimuthal integration. The instrumental broadening was calibrated using a NIST 660a LaB_6 standard, fitted with the modified Thomson-Cox-Hastings pseudo-Voigt peak shape [9]. The batch Rietveld refinements were performed using *TOPAS* (Bruker AXS v. 5) in launch mode using *jEdit* (v. 4.3.1) as the text editor for writing macros for *TOPAS* [10]. Due to the nanocrystalline samples (giving large peak broadening), and the reactions being conducted at temperatures in the range of the cubic to tetragonal phase transition of BT, the cubic and tetragonal space groups could not be differentiated. The cubic space group (no. 221, $Pm\bar{3}m$), using ICDD card #01-074-4539 as a reference, was used for all refinements, refining on zero error, scale factor,

lattice parameter, Lorentzian isotropic size and strain broadening, isotropic thermal parameters (ADP, B_{iso}) for Ba and Ti and a 25th order Chebyshev polynomial for each diffractogram. All batch refinements were refined independently, meaning that the same starting values were used for all diffraction patterns in each batch/experiment.

Kinetics modeling were done using the JMAK model, as described in section 2.3.1. The normalized scale factor obtained from the batch Rietveld refinement was used as measure for the fractional (*f*) extent of the reaction [11].

Scanning electron microscopy

The nature of the *in situ* setup makes collection of the sample for further characterization challenging, but one sample, Ti-CAsol-125, was successfully collected in reasonable amounts. The sample was washed with distilled water several times with a centrifugation and decanting process, before a diluted water-particle dispersion was dropped onto an aluminum sample holder and let dry for ~12 h. Scanning electron microscopy (SEM) images were recorded on an in-lens cold field emission Hitachi S-5500 S(T)EM, with an acceleration voltage of 7 kV and detecting secondary electrons.

3.2 Hydrothermal synthesis of nanostructured $Sr_xBa_{1-x}Nb_2O_6$

3.2.1 Precursor preparation

$Sr_xBa_{1-x}Nb_2O_6$ (SBN100*x*) with nominal composition *x* = 0.2, 0.3, 0.4, 0.5 and 0.6 was prepared by a hydrothermal method using strontium nitrate ($Sr(NO_3)_2$, Sigma-Aldrich, > 99.995 %), barium nitrate ($Ba(NO_3)_2$, Sigma-Aldrich, > 99.999 %) and Nb-acid. The Nb-acid was prepared by first dissolving ammonium niobate (V) oxalate hydrate (~70 g) ($NH_4NbO(C_2O_4)_2\ xH_2O$, Sigma-Aldrich, > 99.99 %) in distilled water (700 mL) under continuous stirring at 50 °C for 3 to 5 h until a clear solution was obtained. Then aqueous ammonia solution (Sigma-Aldrich, 25 wt% solution) was added to increase the pH to 11, leading to the precipitation of Nb-acid (white precipitate), before stirring at room temperature for several days. The precipitate was collected by centrifugation (11300 g/ 10000 rpm for 15 min) and decanting, before re-dispersion in 1 wt% aqueous ammonia solution. This washing procedure was repeated three times to remove oxalate ions. After the final centrifugation, the precipitate was collected and dispersed in 1 wt% aqueous ammonia solution (~125 mL) and kept as a stock solution. Thermogravimetric analysis at 800 °C was used to determine the niobium content of the Nb-acid (normally in the range 0.0008 $\frac{\text{mol Nb}}{\text{g Nb-acid}}$ or ~0.9 M). The washing steps were found to be critical, as low yield and a non-reactive Nb-acid was obtained if the procedure was not performed carefully. For the experiments, 5 mL of precursor was prepared, by first weighing Nb-acid for a final niobium concentration of 0.25 M. Then the pH was increased to 12.4 with the addition of 25 wt% aqueous ammonia solution (~1.5 mL). This step was found to be especially important for aged Nb-acid (*i.e.* when used a few weeks or longer after it was prepared), as it gradually became less and less reactive. Then stoichiometric amounts of strontium and barium nitrate (ratio varied with *x*) were dissolved before adding distilled water to give a total volume of 5 mL. All the *in situ* experiments conducted for SBN is presented in Table 3.2 with an overview of synthesis parameters.

Table 3.2: Sample names, temperature, approximate reaction times, X-ray wavelength and time resolution for the *in situ* XRD experiments of $Sr_xBa_{1-x}Nb_2O_6$. The set pressure was 200 bar for all experiments, except SBN50_supercrit where 250 bar was used.

Name [a]	Temperature [°C]	Approx. experiment time [h]	Wavelength [Å] [b]	Time resolution [s] [c]
SBN60_T300	300	0.9	0.7762	5
SBN60_T225	225	2.3	0.7762	5
SBN60_T200	200	3.7	0.7744	5
SBN50_T400	400	1.3	0.7762	5
SBN50_T300	300	0.7	0.7762	5
SBN50_T225	225	2.1	0.7762	5
SBN50_T200	200	3.6	0.7762	5
SBN50_T175	175	10.4	0.7762	10
SBN40_T300	300	0.6	0.7762	5
SBN40_T225	225	1.3	0.7762	5
SBN40_T200	200	2.4	0.7744	5
SBN30_T300	300	0.6	0.7744	5
SBN30_T225	225	1.4	0.7744	5
SBN30_T200	200	2.6	0.7744	5
SBN20_T300	300	0.5	0.7744	5
SBN20_T225	225	2.2	0.7744	5
SBN20_T200	200	4.1	0.7744	5
SBN50_supercrit	400	3.0	0.7762	2

[a] The nomenclature is SBN*XX*-T*YYY*, where *XX* refers to the Sr mole fraction in precursor times 100 and *YYY* is the reaction temperature.

[b] Experiments conducted at different beam times, therefore slightly varying wavelength.

[c] Time for data collection. Optimized for the different reaction speeds.

Hydrothermal synthesis in the coil setup

Two different setups were used for the hydrothermal synthesis of SBN, namely the *in situ* setup as described for BT, and a tube coil setup. The SBN precursor preparation was identical for the experiments using the two different setups. The tube coil setup, as described by Skjærvø *et al.* [7], consists of a 316 L steel tube coil that was filled with the precursor slurry and connected to a HPLC pump with Swagelok tubes and fittings for hydrostatic pressure. The tube coil was submerged in a fluidized sand bath (Omega FSB-3, Omega Engineering, Norwalk, USA) for heating, and the temperature was controlled with a PID controller. After the reaction, the samples were collected by repeated centrifugation and decanting, before

drying at 105 °C for ~12 h. An overview of the reaction conditions for the experiments conducted in the coil setup is presented in Table 3.3.

Table 3.3: Sample names, temperature and reaction times for all the coil setup experiments of $Sr_xBa_{1-x}Nb_2O_6$. The set pressure was 200 bar for all experiments.

Name [a]	Temperature [°C]	Reaction time [h]
SBN40_T300_1h	300	1
SBN40_T300_6h	300	6
SBN40_T200_1h	200	1
SBN40_T200_6h	200	6
SBN20_T300_1h	300	1
SBN20_T300_6h	300	6

[a] The nomenclature is SBN*XX*-T*YYY*_*ZZ*, where *XX* refers to the Sr mole fraction in precursor times 100 and *YYY* is the reaction temperature and ZZ is the reaction time.

3.2.2 Characterization

***In situ* synchrotron X-ray diffraction**

The setup and experimental details for the *in situ* XRD experiments for SBN are as described for BT, if not otherwise specified in the following section or in Table 3.2. The experiments were conducted at SNBL at ESRF in transmission mode using the PILATUS@SNBL setup [2], and data treatment (*i.e.* masking and integration) was done as explained for BT. Since the experiments were conducted at, or close to the reported T_c for SBN, the centrosymmetric space group (no. 127 *P*4/*mbm*) was used for all the refinements, and not the reported non-centrosymmetric space group (no. 100, *P*4*bm*) stable at room temperature. For the batch refinements, scale factor, two lattice parameters (*a* and *c* in the tetragonal cell), Lorentzian and Gaussian strain parameters, isotropic APD for both niobium and alkaline earth sites (4 in total), Sr fraction, Sr occupancy on the A1-site and 3 atomic position parameters (in total 14 structural parameters) were refined. The three atomic position parameters were the *x* and *y* parameters for the B2- and A1-sites, respectively (only one needed for the A1-site due to symmetry constraints). The structure reported by Carrio *et al.* [12] was used as a starting point, and ADP values for all non-refined ADPs were locked to the values obtained with neutron diffraction in this work. In addition, a 35th order Chebyshev polynomial was refined to account for the broad background feature. Zero error was refined for the last frame, and then kept fixed to this value for the batch refinement. Sr was allowed

to occupy both A1- and A2-sites while Ba was locked to the A2-site, while keeping physical meaningful occupancies (*i.e.* not negative or higher than 1) and the sum of Sr and Ba equal to 5. For increased stability in the refinements, a backwards sequential refinement was performed. This was done by starting the batch refining from the last diffraction pattern (*i.e.* end of experiment with best data quality), and use the output of this refinement as input (*i.e.* starting values) for the next, and so on. This significantly increased stability of the refinements. The reaction kinetics were modeled using the JMAK model and the normalized scale factor as explained for BT and in section 2.3.1 [11].

To gain insight about the pre- and early formation stages during the hydrothermal synthesis of SBN, *in situ* X-ray total scattering and PDF analysis was attempted. To avoid the strong diffuse scattering from the single crystal sapphire capillaries used for the *in situ* powder XRD experiments, these experiments were done in fused silica capillaries (ID 0.7 ± 0.1 mm, OD 0.85 ± 0.2 mm, CM Scientific, Silsden, United Kingdom) coated with Kapton. These experiments were unsuccessful, as SBN did not form in the fused silica capillaries. Later experiments concluded that the use of fused silica was the reason for the unsuccessful outcome of these experiments, which is presented in Appendix B. The reason for this was not investigated further, but is believed to be caused by reactions between silica and niobium species at the highly alkaline conditions.

Synchrotron X-ray total scattering and PDF analysis

X-ray synchrotron total scattering was collected for PDF analysis on selected samples, as described in Table 3.4. The selected samples include SBN synthesized in the coil setup and Nb-acid. The data were collected at BL08W [13] at SPring-8, Koto, Japan using a 16 inch Perkin Elmer XRD 1621 N ES series flat panel detector with a wavelength of 0.10765 Å (115 keV) and a sample to detector distance of ~53 cm. The experimental setup (*i.e.* sample to detector distance and geometry) was calibrated using a NIST CeO_2 standard. The data were treated by masking parasitic regions (*e.g.* beam stopper and edge of detector) and integrated from 2D frames to 1D diffraction patterns using *pyFAI* (v. 0.17.0) [8] and *Jupyter Notebook* (v. 5.7.8) [14]. The data were treated in *xPDFsuite* [15] for background subtraction before Fourier transformation into PDFs using a Q_{max} as listed in Table 3.4. Real-space Rietveld refinement (fitting a unit cell model to the experimental data) was performed using *TOPAS* (Bruker AXS v. 6) in launch mode, with *jEdit* (v. 4.3.1) as the text editor for writing macros [10].

Table 3.4: Overview of the selected samples for PDF analysis. Type and size of capillary in addition to Q_{max} for the Fourier transformation is shown.

Samples	Capillary material	Capillary ID/OD [mm] [a]	Q_{max} [Å^{-1}]	Comment
Nb-acid [b]	Kapton	1.90/1.80	15.0	Nb-acid as-prepared
Nb-acid [c]	Kapton	1.90/1.80	15.0	Nb-acid re-activated
Nb-acid [d]	Kapton	1.05/1.00	21.0	Nb-acid vacuum-dried
SBN40_T300_1h	Kapton	1.05/1.00	29.5	SBN from coil setup
SBN40_T300_6h	Kapton	1.05/1.00	29.5	SBN from coil setup
SBN40_T200_6h	Kapton	1.05/1.00	29.5	SBN from coil setup
SBN20_T300_1h	Kapton	1.05/1.00	29.5	SBN from coil setup
SBN20_T300_6h	kapton	1.05/1.00	29.5	SBN from coil setup

[a] ID and OD stand for inner and outer diameter respectively.

[b] As-prepared Nb-acid. Three samples aged for 18, 284 and 626 days respectively.

[c] Nb-acid re-activated with aqueous ammonia solution. The three samples aged as explained for [a] prior to re-activation.

[d] Nb-acid vacuum dried for increased signal. One sample. Dried right after preparation.

***Ex situ* X-ray diffraction**

Phase purity for the samples prepared with the coil setup were investigated by XRD using a Bruker D8 Advance Da-Vinci equipped with a LynxEye detector working in Bragg-Brentano geometry. Diffraction patterns were recorded with CuK_α radiation (λ = 1.5406 Å), a step size of 0.013° and an integration time of 0.75 s using a variable divergent slit.

Scanning electron microscopy

For SBN, the product from all experiments were collected and investigated with scanning electron microcopy (SEM). When collecting the product from the *in situ* setup, it is nearly impossible to indestructibly separate product from unreacted precursors due to the nature of the *in situ* setup. Thus, a mix of reacted and unreacted precursor in addition to water were collected for these samples, collected by pushing water through the capillary. The samples were used without any further processing after collection, other than dropping a dispersion of the collected samples on an aluminum sample holder for drying. For the samples from the coil setup, an aqueous dispersion was made by mixing the dried particles with distilled water in an ultrasound bath, before dropping this dispersion onto the sample holder. In both cases, the samples were dried for ~6 h. SEM imaging was partly performed with an in-lens cold field emission Hitachi S-5500 S(T)EM, with an acceleration voltage of 7

kV and detecting secondary electrons, and partly with a field emission FEI APREO SEM using an in-lens secondary electron detector with an acceleration voltage of 5 keV and a current of 25 pA.

Transmission electron microscopy

Transmission electron microscopy (TEM) was performed on the hollow-ended nanostructures of SBN20_T300_1h made in the coil setup using a double aberration-corrected Jeol JEM ARM200F with a cold field emission gun. An acceleration voltage of 200 kV was used. The beam convergence angle was 27 mrad and the high-angle annular dark-field scanning TEM (HAADF-STEM) images were acquired using a collection angle of 51 – 203 mrad. Energy-dispersive X-ray spectroscopy (EDS) spectra were collected using a Jeol Centurio SDD detector (solid angle 0.98 sr), with an energy-dispersion of 10 eV per channel. The EDS data were analyzed using *HyperSpy* (v. 1.4.1) [16]. Samples were prepared as described for SEM, but on a holey carbon copper grid.

Nitrogen adsorption measurement

Nitrogen adsorption was measured on selected samples synthesized with the coil setup using a Tristar 3000 (Micrometrics Instrument Corporation, Norcross, USA) at room temperature. Prior to measurements, the samples were degassed at 200 °C for ~17 h to remove adsorbed water. The specific surface area (m^2/g) was estimated using the Brunauer-Emmett-Teller (BET) method [17].

References

1. Wang, G., Rørvik, P. M., van Helvoort, A. T. J., Holmestad, R., Grande, T. and Einarsrud, M.-A. Self-assembled growth of $PbTiO_3$ nanoparticles into microspheres and bur-like structures, *Chemistry of Materials* **19**, 2213-2221, (2007). DOI: 10.1021/cm063047d

2. Dyadkin, V., Pattison, P., Dmitriev, V. and Chernyshov, D. A new multipurpose diffractometer PILATUS@SNBL, *Journal of synchrotron radiation* **23**, 825-829, (2016). DOI: 10.1107/s1600577516002411

3. Broennimann, C. The PILATUS detectors: hybrid pixel detectors for synchrotron and industrial applications, *Acta Crystallographica Section A* **64**, C162, (2008). DOI: 10.1107/S0108767308094786

4. Becker, J., Bremholm, M., Tyrsted, C., Pauw, B., Jensen, K. M. O., Eltzholt, J., Christensen, M. and Iversen, B. B. Experimental setup for *in situ* X-ray SAXS/WAXS/PDF studies of the formation and growth of nanoparticles in near- and supercritical fluids, *Journal of Applied Crystallography* **43**, 729-736, (2010). DOI: 10.1107/S0021889810014688

5. Dalod, A. R. M., Grendal, O. G., Skjærvø, S. L., Inzani, K., Selbach, S. M., Henriksen, L., van Beek, W., Grande, T. and Einarsrud, M.-A. Controlling oriented attachment and *in situ* functionalization of TiO_2 nanoparticles during hydrothermal synthesis with APTES, *The Journal of Physical Chemistry C* **121**, 11897-11906, (2017). DOI: 10.1021/acs.jpcc.7b02604

6. Skjærvø, S. L., Wells, K. H., Sommer, S., Vu, T.-D., Tolchard, J. R., van Beek, W., Grande, T., Iversen, B. B. and Einarsrud, M.-A. Rationalization of hydrothermal synthesis of $NaNbO_3$ by rapid *in situ* time-resolved synchrotron X-ray diffraction, *Crystal Growth & Design* **18**, 770-774, (2018). DOI: 10.1021/acs.cgd.7b01192

7. Skjærvø, S. L., Wells, K. H., van Beek, W., Grande, T. and Einarsrud, M.-A. Kinetics during hydrothermal synthesis of nanosized $K_xNa_{1-x}NbO_3$, *CrystEngComm* **20**, 6795-6802, (2018). DOI: 10.1039/C8CE01178H

8. Ashiotis, G., Deschildre, A., Nawaz, Z., Wright, J. P., Karkoulis, D., Picca, F. E. and Kieffer, J. The fast azimuthal integration Python library: pyFAI, *Journal of Applied Crystallography* **48**, 510-519, (2015). DOI: doi:10.1107/S1600576715004306

9. Thompson, P., Cox, D. E. and Hastings, J. B. Rietveld refinement of Debye-Scherrer synchrotron X-ray data from Al_2O_3, *Journal of Applied Crystallography* **20**, 79-83, (1987). DOI: doi:10.1107/S0021889887087090

10. Evans, J. S. O. Advanced input files & parametric quantitative analysis using Topas, *Materials Science Forum* **650**, 1-9, (2010). DOI: 10.4028/scientific.net/MSF.651.1

11. Peterson, K. M., Heaney, P. J. and Post, J. E. A kinetic analysis of the transformation from akaganeite to hematite: an *in situ* time-resolved X-ray diffraction study, *Chemical Geology* **444**, 27-36, (2016). DOI: doi.org/10.1016/j.chemgeo.2016.09.017

12. Carrio, J. G., Mascarenhas, Y. P., Yelon, W., Santos, I. A., Garcia, D. and Eiras, J. A. Structure refinement of $(Sr,Ba)Nb_2O_6$ ceramic powder from neutron and X-rays diffraction data, *Materials Research* **5**, 57-62, (2002). DOI: 10.1590/S1516-14392002000100010

13. Ohara, K., Tominaka, S., Yamada, H., Takahashi, M., Yamaguchi, H., Utsuno, F., Umeki, T., Yao, A., Nakada, K., Takemoto, M., Hiroi, S., Tsuji, N. and Wakihara, T. Time-resolved pair distribution function analysis of disordered materials on beamlines BL04B2 and BL08W at SPring-8, *Journal of synchrotron radiation* **25**, (2018). DOI: 10.1107/S1600577518011232

14. T. Kluyver, B. Ragan-Kelley, F. Pérez, B. Granger, M. Bussonnier, J. Frederic, K. Kelley, J. Hamrick, J. Grout, S. Corlay, P. Ivanov, D. Avila, Abdalla, S. and C. Willing. Jupyter Notebooks – a publishing format for reproducible computational workflows, *Position. Power Acad. Publ. Play. Agents Agendas,*, 87-90, (2016). DOI: 10.3233/978-1-61499-649-1-87

15. Juhas, P., Davis, T., Farrow, C. L. and Billinge, S. J. L. PDFgetX3: a rapid and highly automatable program for processing powder diffraction data into total scattering pair distribution functions, *Journal of Applied Crystallography* **46**, 560-566, (2013). DOI: doi:10.1107/S0021889813005190

16. F. de la Peña, V. T. Fauske, P. Burdet, E. Prestat, P. Jokubauskas, M. Nord, T. Ostasevicius, K. E. MacArthur, M. Sarahan, D. N. Johnstone, J. Taillon, A. Eljarrat, V. Migunov, J. Caron, T. Furnival, S. Mazzucco, T. Aarholt, M. Walls, T. Slater, F. Winkler, B. Martineau, G. Donval, R. McLeod, E. R. Hoglund, I. Alxneit, I. Hjorth, T. Henninen, L. F. Zagonel, A. Garmannslund and Skorikov, A. hyperspy/hyperspy v1.4.1, (2018). DOI: 10.5281/zenodo.1469364

17. Brunauer, S., Emmett, P. H. and Teller, E. Adsorption of gases in multimolecular layers, *Journal of the American Chemical Society* **60**, 309-319, (1938). DOI: 10.1021/ja01269a023

4 Summary of results and discussion

4.1 Insight into the rapid formation of nanocrystalline $BaTiO_3$

4.1.1 Results

Formation and kinetics

Phase pure nanocrystalline BT was observed to form directly from the amorphous precursors in case of using both the Ti-slurry and Ti-CAsol, without any crystalline intermediates, as shown in Figure 4.1. In case of Ti-CAsol-100 and Ti-CAsol-EG, formation of $BaCO_3$ was also observed, estimated by Rietveld refinement to be 12 and 5 wt%, respectively. The main difference between the results using the two different titanium precursors is the time from heating is initiated to the first crystallization, and time for the reaction to finalize (with respect to changes in crystallite size and normalized scale factor). BT formed almost immediately from the Ti-slurry (within a few seconds after heating is started), and the normalized scale factor and crystallite size stabilize within ~15 s after the heat blower is in position for all reaction temperatures, as shown in Figure 4.2. Using the Ti-CAsol, the first nucleation occurs after around 30 s at 150 °C, and even slower at lower reaction temperatures. The overall reaction times are also increased compared to the Ti-slurry experiments, with the normalized scale factor and crystallite size stabilizing after ~2, ~10 and ~200 min for reactions at 150, 125 and 100 °C, respectively. The crystallite size obtained from Rietveld refinement stabilizes around 15 nm and between 12 and 14 nm for the Ti-slurry and Ti-CAsol experiments, respectively.

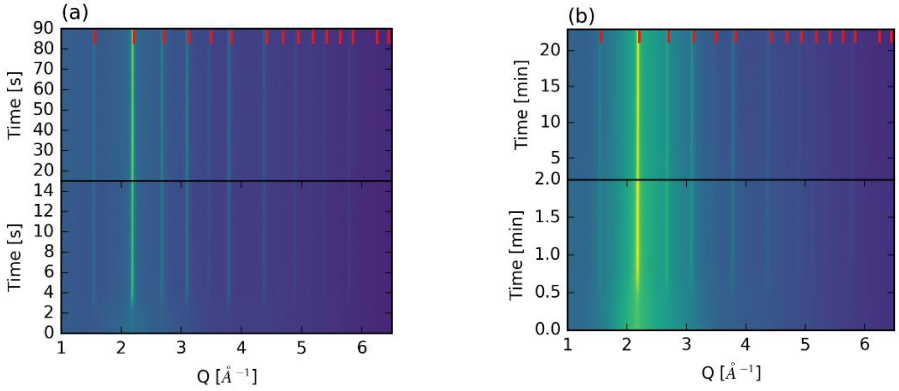

Figure 4.1: Color maps showing the formation of $BaTiO_3$ from amorphous precursors at 150 °C and 200 bar using the a) Ti-slurry and b) Ti-CAsol. Red markers show the room temperature diffraction lines for bulk cubic $BaTiO_3$ from ICDD card #01-074-4539. Notice the different time scales. Reproduced from ref. [1] under the Creative Commons Attribution License (CC BY 4.0).

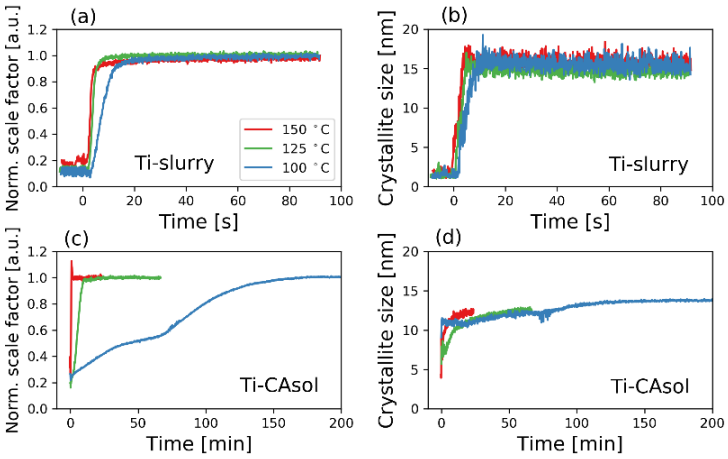

Figure 4.2: In a) and c) time resolved normalized scale factor and in b) and d) crystallite size for $BaTiO_3$ for experiments at 100, 125 and 150 °C with the Ti-slurry and Ti-CAsol, respectively. The scale factors are normalized to the last value. Notice the different time scales. Adapted from ref. [1] under the Creative Commons Attribution License (CC BY 4.0).

By modeling the normalized scale factor with the JMAK-model, the difference between the Ti-slurry and Ti-CAsol experiments also becomes apparent, as shown in the overview given in Table 4.1. The rate constant (k) is one order of magnitude larger using the

Ti-slurry compared to the Ti-CAsol. Using the Ti-slurry, the growth order (*n*) is not significantly affected by the reaction temperature, while for the Ti-CAsol experiments, the growth order increases from 1 to 2 with increasing reaction temperature. The most prominent effect of the surfactants is on the crystallite size for the Ti-slurry experiments. By adding SDBS, the crystallite size increases to ~25 nm, while EG decreases the crystallite size to ~9 nm. Adding SDBS to the Ti-CAsol, no reduction in crystallite size is observed, but with EG ~5 wt% $BaCO_3$ forms together with BT.

Table 4.1: Sample names and rate constant (*k*) and growth order (*n*) as obtained by fitting the time resolved normalized scale factors to the JMAK-model. Included is the coefficient of determination (R^2) indicating the correlation between the experimental data and the JMAK-model.

Sample	*k* [s^{-1}]	*n*	R^2
Ti-slurry-100	0.0130(6)	2.1	0.99
Ti-slurry-125	0.0126(6)	3.1	0.99
Ti-slurry-150	0.063(5)	2.3	0.97
Ti-CAsol-100	0.00054(6)	0.9	0.97
Ti-CAsol-125	0.00023(3)	1.5	0.99
Ti-CAsol-150	0.0013(4)	2.0	0.93

4.1.2 Discussion

Formation and kinetics

The hydrothermal synthesis of BT from the Ti-slurry is shown to proceed rapidly, with nucleation and growth to the final crystallite size of 15 nm all occurring within 15 s from heating is started. This is significantly faster than what is reported when using crystalline TiO_2 (reaction time ~10 h at 125 °C) [2] and faster than what is reported using barium and titanium isopropoxides in a mixed water-ethanol mixture (reaction time ~1 min at 150 °C) [3]. Furthermore, the overall reaction time (from nucleation until growth to final crystallite size) is not significantly affected by the reaction temperature. This is explained by the fact that it takes between 15 to 20 s to reach the set-point temperature with this setup, and the relatively narrow temperature range studied (100 to 150 °C), making the three reactions occurring at essentially similar reaction conditions. From the growth order *n* in Table 4.1, the formation of BT from the Ti-slurry is suggested to proceed by a nucleation and growth controlled mechanism.

When using the Ti-CAsol, BT nucleate and grows into the final crystallite size of 13 nm within 2 min after heating is applied. This is comparable to the hydrothermal synthesis of BT from titanium and barium isopropoxides in a water and ethanol mixture [3] at 150 °C. With decreasing reaction temperature, the total reaction time significantly increases, while the growth order *n* decreases. These observations suggest that the formation of BT with Ti-CAsol proceeds by a nucleation and growth controlled mechanism at high temperatures, while gradually changing to phase-boundary-controlled mechanism with decreasing temperature. A phase-boundary-controlled mechanism is reported earlier for the formation of BT from crystalline TiO_2 (anatase) and $Ba(OH)_2$ [2, 4, 5].

4.2 Composition and morphology control of $Sr_xBa_{1-x}Nb_2O_6$

4.2.1 Results

Phase purity and Sr:Ba ratio

For the experiments performed in both the coil and *in situ* setup, phase pure SBN was obtained for all reaction temperatures when a precursor slurry corresponding to SBN20, SBN30 or SBN40 were used. At higher Sr-fractions (SBN50 and SBN60) two secondary phases were observed, in addition to SBN. One of the secondary phases was identified as a Sr-rich pyrochlore phase (space group $Fd\bar{3}m$ no. 227 with a lattice parameter of ~10.55 Å, referred to as Pyro), while the other secondary phase was not identified (referred to as Uknw). XRD of phase pure SBN obtained for SBN40_T300 is plotted together with SBN50_T300 and SBN50_T175 in Figure 4.3, highlighting observed characteristic diffraction lines for the Pyro and Uknw phase respectively. All observed Bragg reflections that are assigned to either the Pyro or Uknw phase are listed in Table 4.2. The findings regarding the phase purity is summarized in a phase diagram as a function of reaction temperature and Sr-fraction in the precursor slurry in Figure 4.4. Full Rietveld refinements were not performed with all three phases, so the relative amount of the three phases were not determined. Still, based on relative intensities, the general trends are increasing amounts of secondary phases with increasing reaction temperature and Sr-fraction in the precursor. SBN formed directly from the amorphous precursors, with no crystalline intermediates. A temperature dependent incubation time (*i.e.* time from start of reaction to first crystallization) was observed, increasing from a few minutes to ~2 h with decreasing reaction temperature.

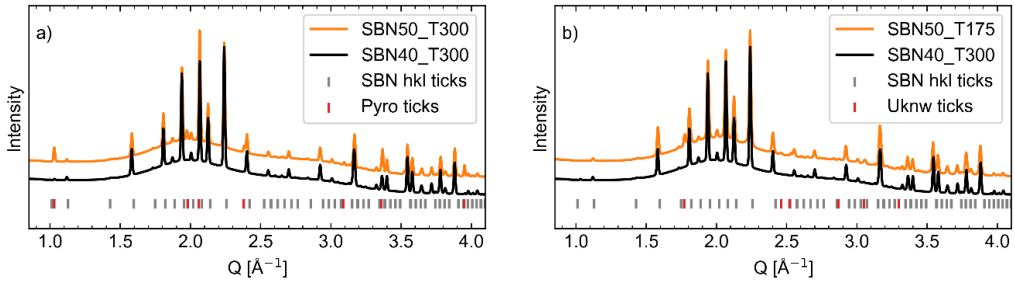

Figure 4.3: a) XRD of phase pure SBN highlighting characteristic diffraction lines assigned to the Pyro phase. b) XRD of phase pure SBN highlighting characteristic diffraction lines assigned to the Uknw phase.

Table 4.2: Identified diffraction lines for both the Pyro and Uknw phase. For Pyro both scattering vector and Miller indices are listed, while only the scattering vector is listed for Uknw.

Pyro		**Uknw**
Q [Å^{-1}]	(h k l)	Q [Å^{-1}]
1.03	(1 1 1)	1.04
1.98	(3 1 1)	1.43
2.06	(2 2 2)	1.68
2.38	(0 0 4)	1.77
3.09	(5 1 1)	1.81
3.37	(0 4 4)	1.94
3.52	(5 3 1)	2.06
3.95	(6 2 2)	2.20
4.12	(4 4 4)	2.45
4.25	(5 5 1)/(7 1 1)	2.52
4.58	(7 3 1)/(5 5 3)	2.55
4.76	(0 0 8)	2.87
5.06	(8 2 2)/(0 6 6)	3.05
5.16	(7 5 1)/(5 5 5)	3.16
5.19	(6 6 2)	3.21
5.33	(0 8 4)	3.28
5.43	(9 1 1)/(7 5 3)	3.42
5.68	(9 3 1)	4.77
5.84	(8 4 4)	4.94
6.19	(6 6 6)/(10 2 2)	5.10

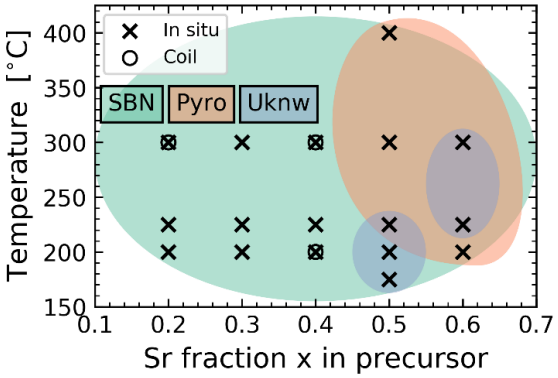

Figure 4.4: Phase diagram showing the formation of SBN, Pyro and Uknw as a function of Sr-fraction in the precursor and reaction temperature. Circles and crosses indicate experiments performed with the *in situ* and coil setup respectively. Adapted from ref. [6] by permission of The Royal Society of Chemistry.

From Rietveld refinements of the *in situ* diffractograms and X-ray total scattering and PDF analysis of selected coil experiments, the Sr-fraction in the different synthesized SBN materials were obtained. A close to linear increase in Sr-fraction in the synthesized SBN was observed with increasing Sr-fraction in the precursor going from 0.2 to 0.5, as shown in Figure 4.5. Increasing the Sr-fraction in the precursor from 0.5 to 0.6 gives no significant increase in the refined Sr-fraction. For all experiments, regardless of reaction temperature or Sr-fraction in the precursor, the Sr-fractions obtained from refinements were in the range 0.35 ± 0.1, with the exception of the *in situ* experiment performed under supercritical conditions, standing out with a Sr fraction of 0.6.

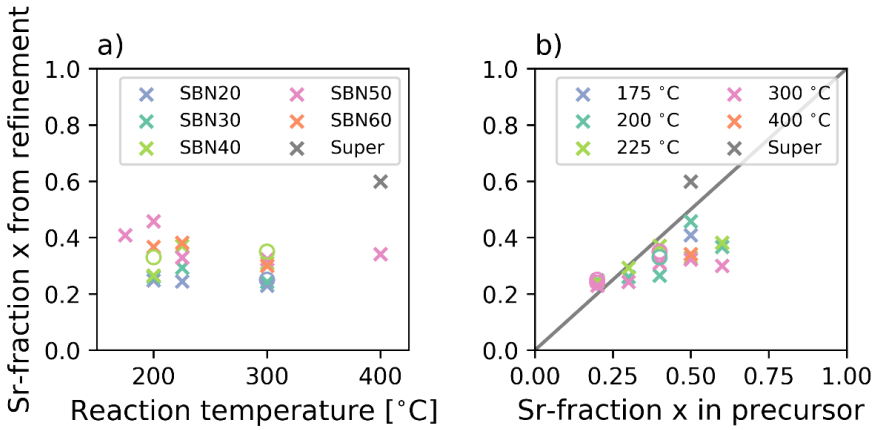

Figure 4.5: a) Sr-fraction as obtained by Rietveld refinement (*in situ* setup) and PDF analysis (coil setup) as a function of reaction temperature b) and Sr-fraction in precursor. Coil experiments are shown as circles with the same color-coding as for the *in situ* experiments shown as crosses. Adapted from ref. [6] by permission of The Royal Society of Chemistry.

Size and morphology

SEM images of SBN synthesized with the *in situ* and coil setups are presented in Figure 4.6 and 4.7, respectively. With a reaction temperature of 300 °C, cube-shaped particles with dimensions around 500 nm were observed for all reactions, except for SBN20, where elongated, apparently hollow particles were observed. For SBN50 and SBN60, some smaller bipyramids were observed in addition to the cube shaped particles, which were found to be the Pyro phase. In some of the SEM images of material prepared by the *in situ* experiments, unreacted amorphous precursor is observed (see SBN60_T225 in Figure 4.6), which is caused by the challenge to separate the reacted and non-reacted precursors when collecting the samples from the *in situ* setup.

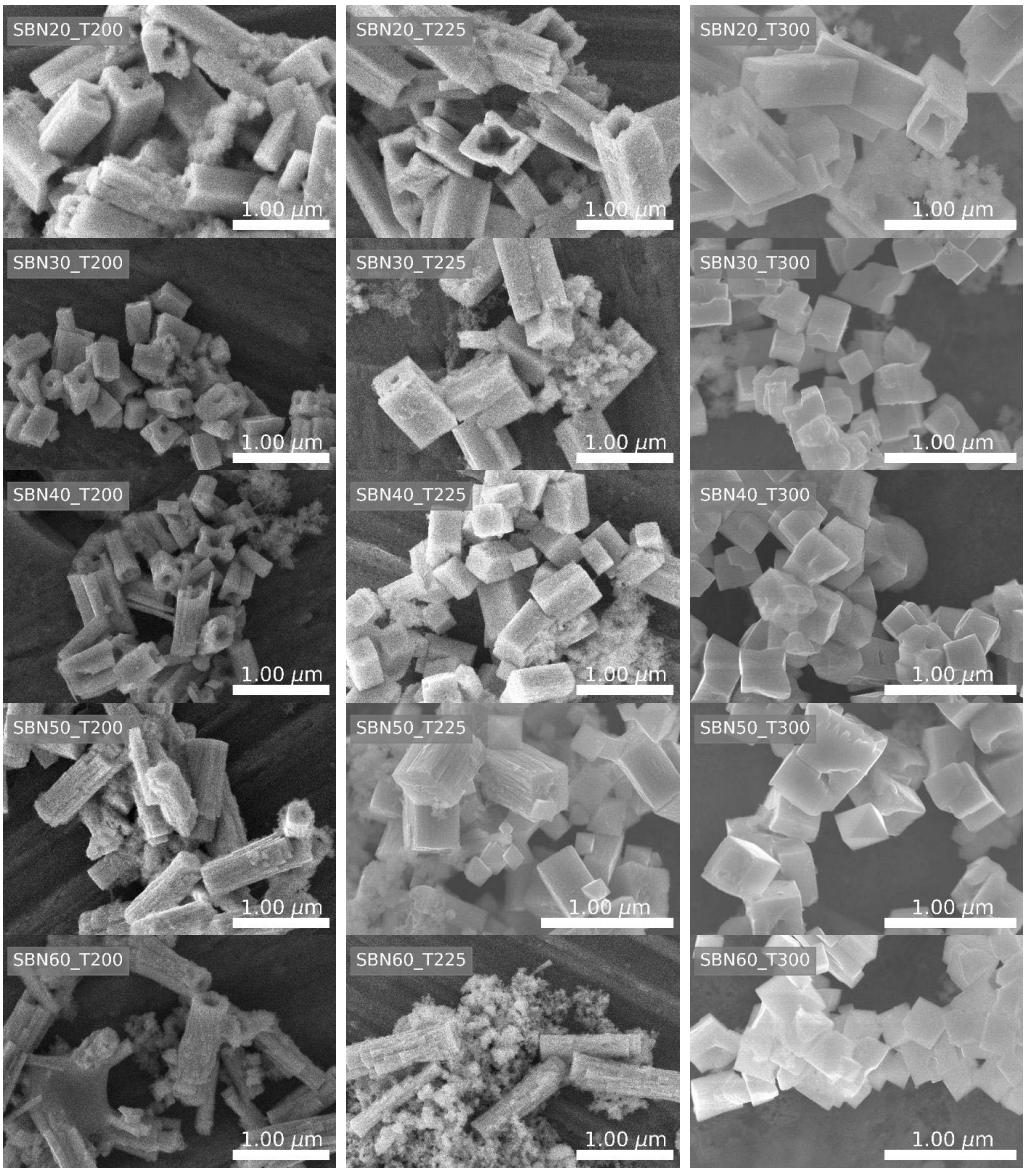

Figure 4.6: SEM images of SBN synthesized in the *in situ* setup with varying Sr-fraction in the precursor (0.2 to 0.6) and reaction temperature (200, 225 and 300 °C). Reproduced from ref. [6] by permission of The Royal Society of Chemistry.

With decreasing reaction temperature there is a general trend of increasing aspect ratio for all Sr-fractions (see SBN50 in Figure 4.6 and SBN40 in Figure 4.6). Furthermore, similar structures to the hollow structures only observed for SBN20 at 300 °C are also observed for higher Sr-fractions at lower reaction temperatures. This is most prominent for SBN30 and SBN40 in Figure 4.6.

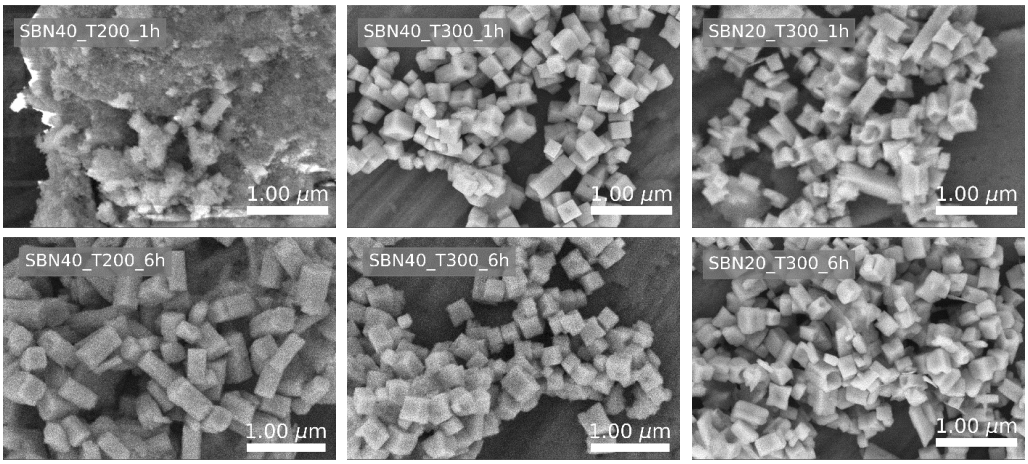

Figure 4.7: SEM images of SBN synthesized in the coil setup with varying Sr-fraction in the precursor (0.2 and 0.4) and reaction temperature (200 and 300 °C). SBN40_T200_1h shows unreacted amorphous precursor, as this reaction did not go to completion, as confirmed with XRD.

The apparently hollow structures of SBN20_T300_1h from the coil setup were investigated further with HAADF-STEM, which gives thickness sensitive contrast assuming constant average Z number in the sample. HAADF-STEM images of two particles are shown in Figure 4.8 a) and c), with the intensity profiles across the image shown as blue lines. It is clear from the images, and the intensity profiles that the particles are not hollow throughout, but have a solid center, with hollow ends. With electron diffraction (Figure 4.8 b) and d)) the elongation of the particles are found to be in the [001]-direction, and the particle facets are normal to the [110]-direction.

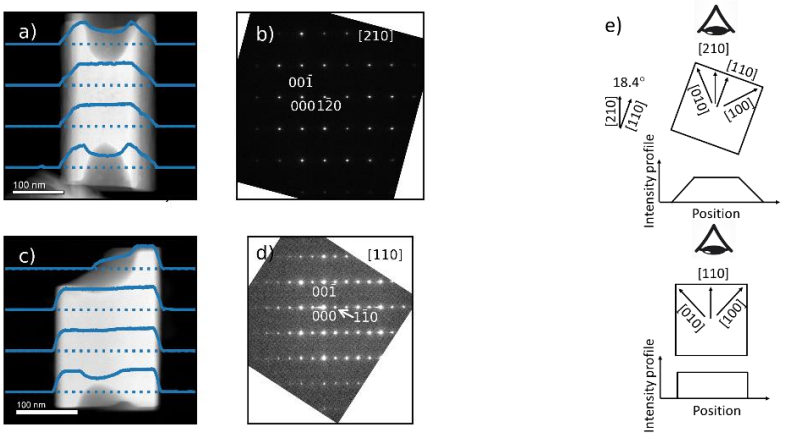

Figure 4.8: a) and c) HAADF-STEM images of two particles from SBN20_T300_1h synthesized with the coil setup. Blue lines show intensity profiles along the blue dashed lines across the particles. b) and d) Indexed electron diffraction patterns of the particles in a) and c), respectively. e) Schematic showing how the two zone axes are linked by a rotation along the length of the particles, and how this affects the intensity profiles across the particle.

The slight difference observed for the intensity profiles in Figure 4.8 a) and c) (*e.g.* box-like function for c) and not for a)) is explained with the two different zone axis and a rotation of the particles relative to the electron beam as shown in Figure 4.8 e). From geometrical considerations and the intensity profiles, this rotation was calculated to be 17.6 °, which is in good agreement with the theoretical angle between the two zone axis of the particles, being 18.4 °.

The formation of hollow-ended structures and cube/rod-shaped particles as a function of reaction temperature and Sr-fraction in the precursor is presented in Figure 4.9. SBN50 and SBN60 is excluded, since SBN formed together with secondary phases, complicating any further discussion. The formation of the hollow-ended structures is promoted at low Sr-fractions (*e.g.* SBN20 forms hollow-ended structures at all reaction temperatures investigated). Furthermore, the formation of the hollow-ended structures is also promoted with decreasing reaction temperature. The reaction kinetics were modeled with the JMAK model for the *in situ* experiments, and the growth order parameter *n* was found to be between 2 and 3.5, without any clear trends with Sr fraction or reaction temperature. These numbers suggest a nucleation and growth controlled mechanism.

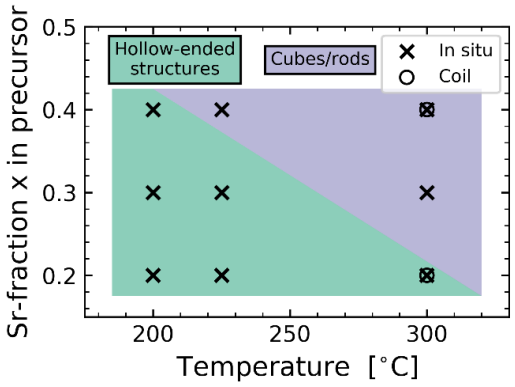

Figure 4.9: Formation of hollow-ended structures as a function of reaction temperature and Sr-fraction in the precursor. Crosses and circles represent experiments performed in the *in situ* and coil setups, respectively.

TEM EDS was used to investigate the distribution of Nb, Sr and Ba using the L_α edge for all elements, as shown in Figure 4.10 for the hollow-ended structures of SBN20_T300_1h. Across the width of the particles, a homogenous composition was observed. In the length direction ([001]-direction) a homogenous composition was observed in the center, with an abrupt onset of a decreasing Sr-fraction closer to the end of the particles (Figure 4.10 c) and h)). In Figure 4.10 k), a schematic representation of the variations in composition is presented, showing the region in the center of the particles with a homogenous composition. In this area, the Sr:Ba ratio is estimated to be 0.3:0.7 based on the relative intensities of Sr L_α and Ba L_α.

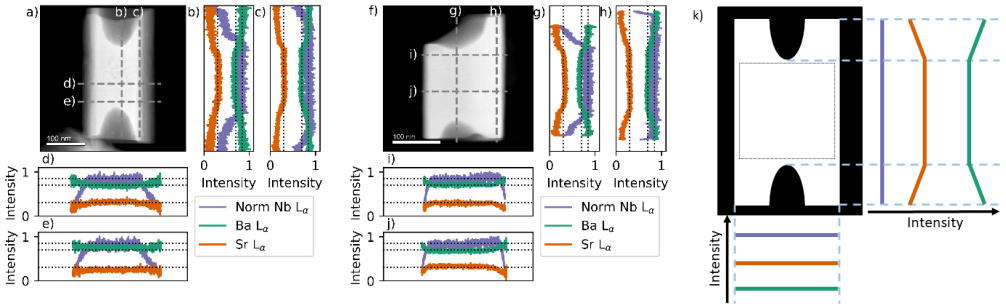

Figure 4.10: a) and f) HAADF-STEM images with gray dashed lines indicating where EDS line scans were performed. b-e) and g-j) show the respective EDS line scans. Nb L_α is normalized to the respective maximum values and is assumed to be constant where there are no thickness gradients, and Sr L_α and Ba L_α have been normalized to the sum of Ba L_α and Sr L_α counts. k) Schematic representation of the intensity distribution of Nb L_α, Sr L_α and Ba L_α, with the gray box indicating an area in the middle of the particle with a homogenous composition. Gray dashed lines in b-e) and g-j) are guides to the eye plotted at 0.3, 0.7 and 0.8, respectively.

Structure of amorphous Nb-acid

The structure of the amorphous Nb-acid was investigated with X-ray total scattering and PDF analysis. The PDF of the as-prepared and vacuum dried Nb-acids are presented in Figure 4.11. Four main peaks are observed in the PDFs, at 1.9, 3.3, 3.7 and 4.7 Å, in addition to some weaker correlations between 5 and 8 Å. No correlations are observed at higher r-values, indicating only short range order. Both PDFs are fitted with a cluster model of the well known Lindquist-ion ($[Nb_6O_{19}]^{8-}$) [7, 8], shown in Figure 4.11 c)). To fit both the peaks at 3.3 and 3.7 Å, the model has been stretched slightly along one of its three equivalent axes, resulting in a good fit to the data.

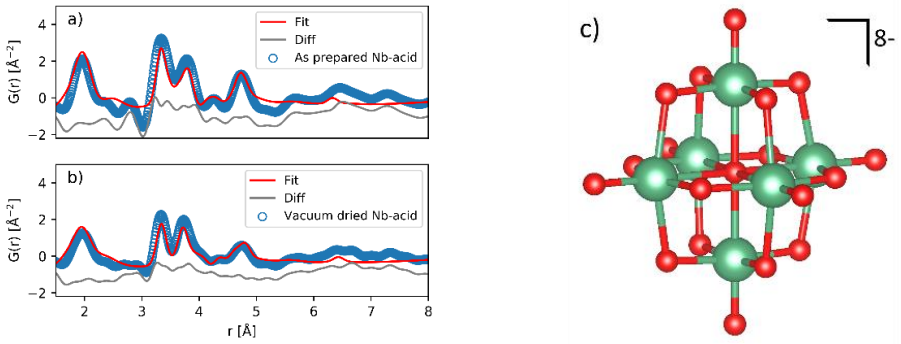

Figure 4.11: a) and b) PDF data of the as-prepared and vacuum dried Nb-acid, fitted with a cluster model of the Lindquist-ion ($[Nb_6O_{19}]^{8-}$). c) A model of the Lindquist-ion, with Nb in green and O in red. Made using *VESTA* [9] based on ref. [7].

Effect of aging of the Nb-acid

At the initial stage of development of the hydrothermal synthesis of SBN, it was found that the age (referring to the time between preparation and use) of the Nb-acid was an important parameter. Aged Nb-acid became unreactive and yielded relatively more secondary phases. This aging is a gradual process, but it became noticeable after ~3 to 4 weeks after preparation. Furthermore, the aged Nb-acid could be re-activated by adding aqueous ammonia solution (increase the pH from ~10 to ~12) hence re-activated aged Nb-acid gave the same results as a freshly prepared Nb-acid. Three Nb-acids prepared in this work were investigated with X-ray total scattering and PDF analysis, in their aged and re-activated state (*i.e.* addition of aqueous ammonia solution to increase pH to ~12 approximately 1 h prior to measurement), as presented in Figure 4.12. At the time of X-ray total scattering data collection, the three Nb-acids had aged for 626, 284 and 18 days, respectively. No significant structural changes in the local structure of Nb-acid was observed as a function of aging, neither before nor after re-activation.

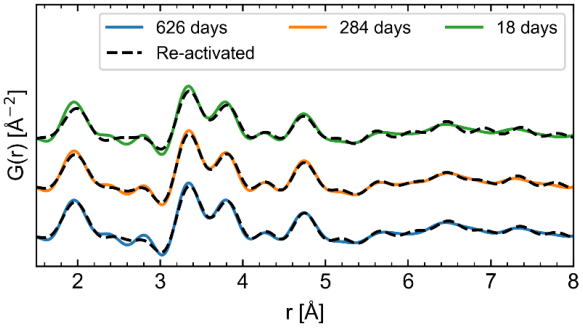

Figure 4.12: PDFs for Nb-acid aged for 626, 284 and 18 days between preparation and measurements in colored full lines. PDFs of the Nb-acid after re-activation in black dashed lines.

4.2.2 Discussion

Growth mechanism of hollow-ended $Sr_xBa_{1-x}Nb_2O_6$

A clear change in morphology is observed as a function of Sr-fraction in precursor and reaction temperature. At low Sr-fractions and low temperature, the formation of hollow-ended nanostructures is observed, while with increasing Sr-fraction and temperature the particles become cube-shaped. The hollow-ended structures are similar to what have been observed for snow crystals [10], olivine in the SiO_2-Al_2O_3-CaO-MgO system from glass cooling experiments [11] and crystallization of struvite (NH_4MgPO_4 $6H_2O$) [12], and can be referred to as a form of skeletal crystals, or more specifically hopper-crystals [13]. This indicates formation under high supersaturation and rapid growth relative to the conditions giving cube-shaped particles. The determining factor for the supersaturation is likely to be the solubility of niobium, as this has the lowest solubility of the three cations (Nb^{5+}, Sr^{2+} and Ba^{2+}), thus the discussion will be focused around this.

First, consider the reactions at 300 °C, with varying Sr-fraction. Here only SBN20 was forming the hollow-ended structures, implying a higher supersaturation of the Nb-species with low Sr-fractions. Knowing that our Nb-acid precursor consists of motifs of the Lindquist-ion, we infer from our observations that this ion forms salt complexes with Sr^{2+} and Ba^{2+}, where the solubility increases with decreasing Sr fraction, giving a higher supersaturation. The same trend (increasing solubility of salt complexes going down the periodic table) is observed for the Lindquist-ion with alkali metal ions [8, 14]. The Sr:Ba fraction is observed to give chemical control over the growth mechanism, where the reaction is pushed into the hopper growth regime with decreasing Sr fraction.

With decreasing temperature, the hollow-ended structures are also observed for SBN30 and SBN40, indicating that decreasing the temperature increases the supersaturation. We propose that due to the slower kinetics at lower temperature, a larger supersaturation is needed to overcome the formation barrier. This pushes all systems into the hopper-growth regime, still keeping the relative differences in supersaturation due to Sr:Ba fraction as explained above. In addition to the chemical control, the growth mechanism can also be controlled by the kinetics via the reaction temperature.

Tuning composition of SBN

With increasing Sr-fraction in the precursor from 0.2 to 0.5 the Sr-fraction in the final SBN increased close to linearly, which is expected, from 0.25 to 0.4. There was not a one-to-one relationship between the Sr-fraction in the precursor and the Sr-fraction in the final SBN, which is possibly explained as an artefact of the refinements. Increasing the Sr-fraction in the precursor further did not increase the Sr-fraction in the final SBN, but increased the amount of secondary phase, which makes sense, since at least the Pyro phase was found to be Sr-rich. All the refined SBN Sr-fractions were found to be in the range 0.35 ± 0.1, except for the reaction at supercritical conditions, which was found to have a Sr fraction of 0.6. At supercritical conditions, the dielectric constant drops significantly and water becomes a non-polar solvent [15], thus the solubility of both $Sr(NO_3)_2$ and $Ba(NO_3)_2$ can be assumed to be low [16]. The higher Sr-fraction can then be explained with an easier incorporation of the smaller Sr^{2+} into the SBN structure. In this work, controlled composition was achieved at low Sr-fractions by just changing the cation ratio in the precursor solution. Changing the dielectric constant of the solvent, either by going supercritical, or having a mixed solvent (*e.g.* water-ethanol) looks like a promising way for controlling the composition also for high Sr-fractions and at the same time avoiding secondary phases based on this work.

Nb-acid aging

A clear effect of aging of the Nb-acid was observed in the hydrothermal synthesis of SBN, as the Nb-precursor became less reactive and yielding more secondary phases after aging. Fairbrother *et al.* [17] reported on a rapid (overnight) decrease in reactivity (measured as how easy it would re-disperse into water soluble complexes with various complexing agents) of freshly precipitated Nb-acid. In this work it was found that the Nb-acid could be re-activated with the addition of aqueous ammonia solution increasing the pH. No local structural changes of the Nb-acid were observed as a function of aging, or before and after re-activation. This suggest that the degree of protonation (*i.e.* value of x in $[H_xNb_6O_{19}]^{(8-x)-}$) is

important for the reactivity of the Nb-acid. The degree of protonation increases with increasing pH [8, 18], and the monoprotonated species is dominant at pH around 12 [8], suggesting that a further increase in reactivity is possible at higher pH values.

References

1. Grendal, O., Blichfeld, A., Skjærvø, S., van Beek, W., Selbach, S., Grande, T. and Einarsrud, M.-A. Facile low temperature hydrothermal synthesis of $BaTiO_3$ nanoparticles studied by *in situ* X-ray diffraction, *Crystals* **8**, 253-264, (2018).

2. Walton, R. I., Smith, R. I., Millange, F., Clark, I. J., Sinclair, D. C. and O'Hare, D. An *in situ* time-resolved neutron diffraction study of the hydrothermal crystallisation of barium titanate, *Chemical Communications*, 1267-1268, (2000). DOI: 10.1039/b003386n

3. Philippot, G., Jensen, K. M. O., Christensen, M., Elissalde, C., Maglione, M., Iversen, B. B. and Aymonier, C. Coupling *in situ* synchrotron radiation with ex situ spectroscopy characterizations to study the formation of $Ba_{1-x}Sr_xTiO_3$ nanoparticles in supercritical fluids, *Journal of Supercritical Fluids* **87**, 111-117, (2014). DOI: 10.1016/j.supflu.2013.12.009

4. Hertl, W. Kinetics of barium titanate synthesis, *Journal of the American Ceramic Society* **71**, 879-883, (1988). DOI: 10.1111/j.1151-2916.1988.tb07540.x

5. Eckert, J. O., Hung-Houston, C. C., Gersten, B. L., Lencka, M. M. and Riman, R. E. Kinetics and mechanisms of hydrothermal synthesis of barium titanate, *Journal of the American Ceramic Society* **79**, 2929-2939, (1996). DOI: 10.1111/j.1151-2916.1996.tb08728.x

6. Grendal, O. G., Blichfeld, A. B., Vu, T. D., van Beek, W., Selbach, S. M., Grande, T. and Einarsrud, M.-A. Composition and morphology tuning during hydrothermal synthesis of $Sr_xBa_{1-x}Nb_2O_6$ tetragonal tungsten bronzes studied by *in situ* X-ray diffraction, *CrystEngComm* **21**, 5922-5930, (2019). DOI: 10.1039/C9CE01049A

7. Lindqvist, I. The structure of the hexaniobate ion in $7Na_2O{\cdot}6Nb_2O_5{\cdot}32H_2O$, *Arkiv for kemi* **5**, 247-250, (1952).

8. Nyman, M. Polyoxoniobate chemistry in the 21st century, *Dalton Transactions* **40**, 8049-8058, (2011). DOI: 10.1039/C1DT10435G

9. Momma, K. and Izumi, F. VESTA 3 for three-dimensional visualization of crystal, volumetric and morphology data, *Journal of Applied Crystallography* **44**, 1272-1276, (2011). DOI: 10.1107/S0021889811038970

10. Libbrecht, K. G. Physical dynamics of ice crystal growth, *Annual Review of Materials Research* **47**, 271-295, (2017). DOI: 10.1146/annurev-matsci-070616-124135

11. Faure, F., Trolliard, G., Nicollet, C. and Montel, J.-M. A developmental model of olivine morphology as a function of the cooling rate and the degree of undercooling, *Contributions to Mineralogy and Petrology* **145**, 251-263, (2003). DOI: 10.1007/s00410-003-0449-y

12. Shaddel, S., Ucar, S., Andreassen, J.-P. and Østerhus, S. W. Engineering of struvite crystals by regulating supersaturation – correlation with phosphorus recovery, crystal morphology and process efficiency, *Journal of Environmental Chemical Engineering* **7**, 102918, (2019). DOI: 10.1016/j.jece.2019.102918

13. Gornitz, V., in *Mineralogy*, Springer US, Boston, MA, 469-473, (1981). DOI: 10.1007/0-387-30720-6_130

14. Skjærvø, S. L., Sommer, S., Nørby, P., Bøjesen, E. D., Grande, T., Iversen, B. B. and Einarsrud, M.-A. Formation mechanism and growth of $MNbO_3$, M=K, Na by *in situ* X-ray diffraction, *Journal of the American Ceramic Society* **100**, 3835-3842, (2017). DOI: 10.1111/jace.14932

15. Einarsrud, M.-A. and Grande, T. 1D oxide nanostructures from chemical solutions, *Chemical Society Reviews* **43**, 2187-2199, (2014). DOI: 10.1039/C3CS60219B

16. *CRC Handbook of Chemistry and Physics, 99th Edition (Internet Version 2018)*, CRC Press/Taylor & Francis, Boca Raton, Florida, USA.

17. Fairbrother, F., Robinson, D. and Taylor, J. B. Some water-soluble complexes of pentavalent niobium and tantalum, *Journal of Inorganic and Nuclear Chemistry* **8**, 296-301, (1958). DOI: 10.1016/0022-1902(58)80194-3

18. Jehng, J.-M. and Wachs, I. E. Niobium oxide solution chemistry, *Journal of Raman Spectroscopy* **22**, 83-89, (1991). DOI: 10.1002/jrs.1250220207

5 Concluding remarks after 30 years of *in situ* experiments

In situ experiments of hydrothermal synthesis have been conducted for 30 years since the early work by Polak *et al.* [1] in 1990, investigating the formation and growth of a wide range of materials. Obviously, system specific (*i.e.* for the specific materials and reaction conditions investigated) insight about the formation and growth has been obtained. However, the high reaching goal for many these studies, including this work, has been to gain a fundamental understanding of the hydrothermal synthesis that is not necessarily system specific, and provide generic theoretical models for nucleation and growth applicable to the synthesis of all materials. This will allow moving away from trial-and-error approaches when developing new synthesis routes, and potentially enable rational design of materials with controlled size, morphology, stoichiometry and doping levels, which to some degree have been achieved for the synthesis of organic materials [2, 3]. So the question is: have we achieved a fundamental understanding of the hydrothermal synthesis? And if not, will we ever do? The short answers are no, and possibly, in my humble opinion.

Trying to draw some general conclusions from existing literature is a challenging task. Both because the focus of the different works are spread, as shown in section 2.3.2, but also because apparently similar materials with similar precursor chemistry show very different nucleation and growth mechanisms. For example, the hydrothermal synthesis of the three perovskites, $BaTiO_3$, $NaNbO_3$ and $KNbO_3$, proceeds very differently from their respective

binary oxides (TiO_2 and Nb_2O_5) and dissolved metal hydroxides ($Ba(OH)_2$, NaOH and KOH) under alkaline conditions. $BaTiO_3$ forms via a dissolution-precipitation mechanism without any crystalline intermediates, with the complete reaction taking ~60 min at 200 °C [4]. A similar dissolution-precipitation mechanism was observed for $KNbO_3$, with the complete reaction taking ~35 min at 250 °C [5]. In contrast, the complete conversion of Nb_2O_5 into $NaNbO_3$ takes less than 5 min at 250 °C, and proceeds through several crystalline intermediate phases [5]. The intermediates are later shown to directly influence the final size and morphology [6].

Another example is the synthesis of $Ce_xZr_{1-x}O_2$ (x = 0.0, 0.2, 0.5, 0.8, 1.0), where a distinct change in growth kinetics are reported as a function x, even though a continues solid solution was obtained [7]. At high ceria fractions, the growth is initially limited by surface reaction kinetics and becoming limited by diffusion of monomers to the surface at larger particle sizes. For high zirconia fractions, the opposite is observed. Later, both the formation of CeO_2 (x = 1) and ZrO_2 (x = 0) have been investigating further with *in situ* X-ray total scattering, revealing significant differences in the pre- and early nucleation stages. In the case of CeO_2, dimeric Ce(IV) nitrate pre-nucleation clusters are observed to assemble into CeO_2 [8], while for ZrO_2 chains of edge-sharing cyclic zirconium tetramers are observed to first break up into smaller clusters before assembly into ZrO_2 [9].

Furthermore, for the synthesis of WO_3 [10] and ZrO_2 [9] the effect of two different solvents were investigated, respectively, giving different reaction routes and influencing the crystalline structure of the final product. In the case of WO_3, the α-Keggin polyoxotungstate was stable in the precursor solution in both water and oleylamine solvents. However, the reactions proceeded through different intermediate clusters in the two solvents, which in the end resulted in crystalline nanoparticles with a large degree of disorder and perfectly ordered in water and oleylamine, respectively [10]. The degree of disorder is rationalized based on the observed intermediate clusters and phases. A similar scheme is reported for ZrO_2, where the same cluster structure is stable in both water and methanol, but undergoes different changes before crystallization in the two solvents, which further controls the polymorph of the final crystalline ZrO_2 (monoclinic in water and mix of tetragonal and monoclinic in methanol) [9]. A schematic overview of reported nucleation and growth mechanisms is presented in Figure 4.13.

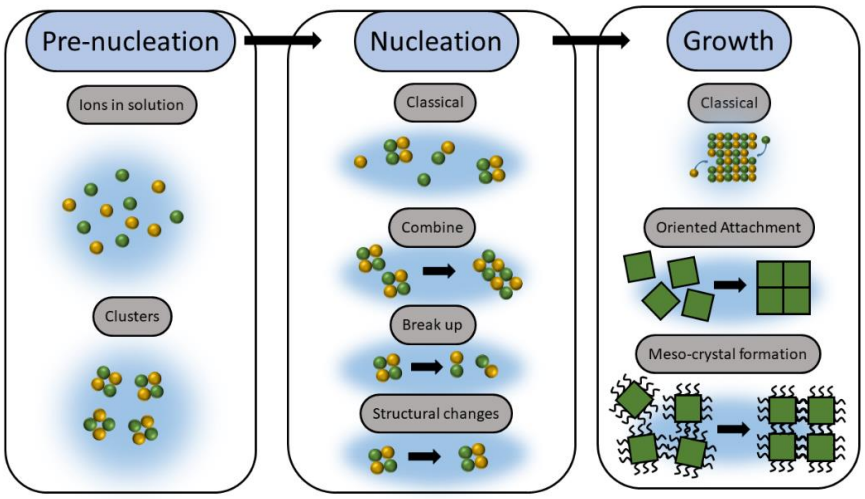

Figure 4.13: Schematic illustration of possible nucleation and growth mechanisms during hydrothermal synthesis, showing both classical and non-classical mechanisms. This is not an exhaustive overview. For a real system, the reaction path is not necessarily a straight path from left to the right.

From the above discussion and section 2.3.2, the only common factor seems to be that chemically different systems behave differently, which is not surprising at all. For full control of the nucleation and growth during hydrothermal synthesis of inorganic materials, a fundamental understanding of the underlying chemistry of each system is necessary. The purely statistical models of classical nucleation and growth theory is in many cases too crude to capture the full picture, but not necessarily wrong, or useless nonetheless. As exemplified in this work, the combination of chemical insight and classical growth theory proved important in explaining the formation of hollow-ended SBN as a function of Sr-fraction in the precursor and reaction temperature. It seems unlikely that one single deterministic model for the nucleation and growth of all inorganic materials can be found. Instead, some predicting power can be sought for chemically similar systems by combining system specific chemical insight and classical theories. For example, the work done on the niobium based $NaNbO_3$, $KNbO_3$ and $K_xNa_{1-x}NbO_3$ [5, 6] have proven to give important insight for the development of the synthesis route for the niobium based SBN in this work.

References

1. Polak, E., Munn, J., Barnes, P., Tarling, S. E. and Ritter, C. Time-resolved neutron diffraction analyses of hydrothermal syntheses using a novel autoclave cell, *Journal of Applied Crystallography* **23**, 258-262, (1990). DOI: 10.1107/S0021889890002473

2. El-Kaderi, H. M., Hunt, J. R., Mendoza-Cortés, J. L., Côté, A. P., Taylor, R. E., Keeffe, M. and Yaghi, O. M. Designed synthesis of 3D covalent organic frameworks, *Science* **316**, 268, (2007). DOI: 10.1126/science.1139915

3. Bøjesen, E. D. and Iversen, B. B. The chemistry of nucleation, *CrystEngComm* **18**, 8332-8353, (2016). DOI: 10.1039/C6CE01489E

4. Walton, R. I., Millange, F., Smith, R. I., Hansen, T. C. and O'Hare, D. Real time observation of the hydrothermal crystallization of barium titanate using *in situ* neutron powder diffraction, *Journal of the American Chemical Society* **123**, 12547-12555, (2001). DOI: 10.1021/ja011805p

5. Skjærvø, S. L., Sommer, S., Nørby, P., Bøjesen, E. D., Grande, T., Iversen, B. B. and Einarsrud, M.-A. Formation mechanism and growth of $MNbO_3$, M=K, Na by *in situ* X-ray diffraction, *Journal of the American Ceramic Society* **100**, 3835-3842, (2017). DOI: 10.1111/jace.14932

6. Skjærvø, S. L., Wells, K. H., van Beek, W., Grande, T. and Einarsrud, M.-A. Kinetics during hydrothermal synthesis of nanosized $K_xNa_{1-x}NbO_3$, *CrystEngComm* **20**, 6795-6802, (2018). DOI: 10.1039/C8CE01178H

7. Tyrsted, C., Becker, J., Hald, P., Bremholm, M., Pedersen, J. S., Chevallier, J., Cerenius, Y., Iversen, S. B. and Iversen, B. B. *In-situ* synchrotron radiation study of formation and growth of crystalline $Ce_xZr_{1-x}O_2$ nanoparticles synthesized in supercritical water, *Chemistry of Materials* **22**, 1814-1820, (2010). DOI: 10.1021/cm903316s

8. Tyrsted, C., Jensen, K. M. O., Bøjesen, E. D., Lock, N., Christensen, M., Billinge, S. J. L. and Brummerstedt Iversen, B. Understanding the formation and evolution of ceria nanoparticles under hydrothermal conditions, *Angewandte Chemie* **124**, 9164-9167, (2012). DOI: 10.1002/ange.201204747

9. Dippel, A.-C., Jensen, K. M. O., Tyrsted, C., Bremholm, M., Bojesen, E. D., Saha, D., Birgisson, S., Christensen, M., Billinge, S. J. L. and Iversen, B. B. Towards atomistic understanding of polymorphism in the solvothermal synthesis of ZrO_2 nanoparticles, *Acta Crystallographica Section A* **72**, 645-650, (2016). DOI: 10.1107/S2053273316012675

10. Juelsholt, M., Lindahl Christiansen, T. and Jensen, K. M. Ø. Mechanisms for tungsten oxide nanoparticle formation in solvothermal synthesis: from polyoxometalates to crystalline materials, *The Journal of Physical Chemistry C* **123**, 5110-5119, (2019). DOI: 10.1021/acs.jpcc.8b12395

6 Conclusions

In this work, hydrothermal synthesis routes for production of the lead-free ferroelectric materials $BaTiO_3$ (BT) and $Sr_xBa_{1-x}Nb_2O_6$ (SBN100*x*) were developed. The nucleation and growth during the hydrothermal synthesis were investigated by *in situ* synchrotron X-ray diffraction, providing insight into the underlying chemistry for the formation of these materials.

Two different titanium precursors were used to synthesize BT, one amorphous $TiO_2{\cdot}xH_2O$ precipitate (Ti-slurry), and one soluble titanium citric acid complex (Ti-CAsol), respectively. Both precursors yielded nanocrystalline BT particles. The complete reaction was found to be fast when the Ti-slurry was used, as nanocrystalline BT formed within a few seconds and the complete reaction took only ~15 s. This reaction was found to not be very dependent on temperature in the temperature range studied, and the kinetics suggested a nucleation and growth controlled mechanism (n = ~2.5), yielding crystallite sizes of ~15 nm. At high temperatures, the Ti-CAsol also yielded nanocrystalline BT (~13 nm) formed via a nucleation and growth controlled mechanism (n = 2). With decreasing temperature, the total reaction time increased significantly using the Ti-CAsol, from 2 to 200 min. A change from nucleation and growth controlled (n = 2) to a phase-boundary-controlled mechanism (n = 1) was observed with decreasing reaction temperature for the Ti-CAsol. The surfactant SDBS was observed to increase the crystallite size (~25 nm) in case of the Ti-slurry, while EG decreased the crystallite size (~10 nm). No significant effect was observed with the surfactants for the Ti-CAsol.

A new synthesis route was developed for SBN-based materials, where both the composition (*i.e.* Sr:Ba ratio) and morphology of the final material could be controlled.

Rietveld refinement and X-ray total scattering with PDF analysis revealed a close to linear increase in Sr-fraction in the final materials as a function of Sr-fraction in the precursor. All the experiments at subcritical conditions gave a Sr-fraction in the range 0.35 ± 0.1. Furthermore, the composition of the synthesized SBN could be controlled by changing the dielectric properties of the solvent. This was done by performing experiments at supercritical conditions, yielding a Sr-fraction of 0.6. At high temperature and high Sr-fractions in the precursor, cube-shaped particles with a size of ~500 nm were obtained. With a decrease in reaction temperature, a slight elongation of the cube-shaped particles were generally observed. Moreover, it was shown how the morphology of the final product could be tuned from cube- and rod-shaped particles to hollow-ended particles. This control of the final morphology was achieved by manipulating the supersaturation of the system, both with chemical control (*i.e.* Sr:Ba ratio in the precursor) and kinetic control (*i.e.* reaction temperature). The growth of the hollow-ended particles were described by a hopper-growth mechanism. From kinetics analysis a nucleation and growth controlled mechanism was observed for SBN (n = ~3). The changes in supersaturation, and thus changes in growth mechanism, could be explained based on chemical insight about the local structure of the amorphous Nb-acid precursor, being similar to the well-known Lindquist-ion ($[Nb_6O_{19}]^{8-}$). A trend of increasing solubility of salt complexes forming between the Lindquist-ion and alkaline earth metal-ions were observed going down the periodic table (*i.e.* solubility increases with decreasing size difference between anion and cation). A similar trend have been observed also for alkali metal ions and the Lindquist-ion, but not previously for alkaline earth metal ions.

7 Outlook

The present study adds to existing literature describing the formation of BT under hydrothermal conditions, by investigating two previously unstudied titanium precursors with *in situ* X-ray diffraction. For the results presented in this thesis, the low reaction temperature and short reaction times, especially using the Ti-slurry, is highly advantageous for large scale production of nanosized BT, as energy consumption is reduced. Furthermore, for large scale production, continuous flow synthesis is probably a more viable option than the conventional batch synthesis routes, and also here the highly reactive precursor described in this work will be beneficial. Lastly, it is shown how the size can be controlled by the addition of a surfactant, which is a key aspect in the synthesis of nanosized materials, as the size is directly linked to properties at the nanoscale.

A new hydrothermal synthesis route of SBN was developed, where tunability of both composition and morphology of the product were demonstrated. This is important since both of these parameters are known to affect the properties of the final material. Sr-fractions up to ~0.4 were achieved without forming secondary phases or using supercritical conditions. However, the experiment performed under supercritical conditions suggest that even higher Sr-fraction can be obtained, potentially without introducing secondary phases, by changing the dielectric properties of the solvent. This can for example be done using a mixed solvent (*e.g.* water-ethanol), providing even better control over the final composition. The work on SBN also highlights the importance of insight about the specific chemistry of the precursors, and how this together with classical and non-classical theories for nucleation and growth provides a tool box for the further development and control of the hydrothermal synthesis.

The high reaching goal of this work has been to gain fundamental and system independent understanding of the nucleation and growth during hydrothermal synthesis, with a special focus on the technologically important ferroelectric materials. As discussed in section 4.3, this is probably not an attainable goal for a PhD thesis, nor for the scientific community. However, we can hope for some predicating power and transferable knowledge between chemically similar materials, and with this in mind, this thesis provides valuable contributions. This is exemplified in this work, by the development a new synthesis route for the niobium-based SBN, aided by existing literature on other niobium-based materials. Now, after 30 years of *in situ* studies during hydrothermal synthesis, the literature has become extensive enough for some materials systems, that we can start harvesting some of the benefits when developing and designing synthesis routes. With this thesis the collective library for chemical insight into the hydrothermal synthesis have been expanded, and will aid future developments in using this synthesis route.

8 Papers and manuscript

Paper 1:

Grendal, O.G., Blichfeld, A. B., Skjærvø, S. L., van Beek, W., Selbach, S. M., Grande, T., Einarsrud, M.-A., Facile low temperature hydrothermal synthesis of $BaTiO_3$ nanoparticles studied by *in situ* X-ray diffraction, *Crystals* **8**, 253-264 (2018).
Reprinted under the Creative Commons Attribution License (CC BY 4.0).

Paper 2:

Grendal, O.G., Blichfeld, A. B., Vu, T. D., van Beek, W., Selbach, S. M., Grande, T., Einarsrud, M.-A., Composition and morphology tuning during hydrothermal synthesis of $Sr_xBa_{1-x}Nb_2O_6$ tetragonal tungsten bronzes studied by *in situ* X-ray diffraction, *CrystEngComm* **21**, 5922-5930 (2019).
Reprinted by permission of The Royal Society of Chemistry.

Manuscript 1:

Grendal, O.G., Nylund, I.-E., Blichfeld, A. B., Tominaka, S., Ohara, K., Selbach, S. M., Grande, T., Einarsrud, M.-A., Designed growth of $Sr_xBa_{1-x}Nb_2O_6$ hopper- and cube-shaped nanostructures by hydrothermal synthesis, submitted to *Chemistry: A European Journal* (January, 2020).

crystals

MDPI

Article

Facile Low Temperature Hydrothermal Synthesis of $BaTiO_3$ Nanoparticles Studied by In Situ X-ray Diffraction

Ola G. Grendal [1], Anders B. Blichfeld [1], Susanne L. Skjærvø [1], Wouter van Beek [2], Sverre M. Selbach [1], Tor Grande [1] and Mari-Ann Einarsrud [1,*]

[1] Department of Materials Science and Engineering, NTNU Norwegian University of Science and Technology, 7491 Trondheim, Norway; ola.g.grendal@ntnu.no (O.G.G.); anders.b.blichfeld@ntnu.no (A.B.B.); susanne.l.skjarvo@ntnu.no (S.L.S.); sverre.magnus.selbach@ntnu.no (S.M.S.); tor.grande@ntnu.no (T.G.)

[2] Swiss-Norwegian Beamlines at European Synchrotron Research Facility, 38043 Grenoble, France; wouter@esrf.fr

* Correspondence: mari-ann.einarsrud@ntnu.no; Tel.: +47-735-94-002

Received: 30 April 2018; Accepted: 15 June 2018; Published: 17 June 2018

Abstract: Ferroelectric materials are crucial for today's technological society and nanostructured ferroelectric materials are important for the downscaling of devices. Controlled and reproducible synthesis of these materials are, therefore, of immense importance. Hydrothermal synthesis is a well-established synthesis route, with a large parameter space for optimization, but a better understanding of nucleation and growth mechanisms is needed for full utilization and control. Here we use in situ X-ray diffraction to follow the nucleation and growth of $BaTiO_3$ formed by hydrothermal synthesis using two different titanium precursors, an amorphous titania precipitate slurry and a Ti-citric acid complex solution. Sequential Rietveld refinement was used to extract the time dependency of lattice parameters, crystallite size, strain, and atomic displacement parameters. Phase pure $BaTiO_3$ nanoparticles, 10–15 nm in size, were successfully synthesized at different temperatures (100, 125, and 150 °C) from both precursors after reaction times, ranging from a few seconds to several hours. The two precursors resulted in phase pure $BaTiO_3$ with similar final crystallite size. Finally, two different growth mechanisms were revealed, where the effect of surfactants present during hydrothermal synthesis is discussed as one of the key parameters.

Keywords: $BaTiO_3$; hydrothermal synthesis; in situ; X-ray diffraction; nanoparticles

1. Introduction

Nanostructured ferroelectric materials are central for further development of electronics and information technology [1]. To answer this demand, cheap, controllable, scalable, environmentally friendly, simple, and reproducible fabrication routes must be developed. Wet chemical methods [2], like hydrothermal syntheses, are among the most promising routes [3].

$BaTiO_3$ (BT) has been of technological interest for many years due to its ferroelectric properties below 125 °C (non-volatile ferroelectric memories), piezo- and pyroelectricity (sonar, detectors, bone implants), and high dielectric constant and low dielectric loss (capacitors, thermistors, transducers) [4]. A variety of precursors and solvents have been shown to yield BT under various hydrothermal conditions [5]. Different sizes and morphologies have been reported, including spherical nanoparticles [6], -rods [7], and -cubes [8]. Dutta and Gregg [9] reported a hydrothermal synthesis, giving 0.2–1 µm sized BT particles after reaction times of 24 h or longer. Precursors used were TiO_2 (anatase) particles and $BaCl_2$ or $Ba(OH)_2$ in water with NaOH as a mineralizer. The synthesized BT

particles were reported to be larger, with a larger tetragonality and a more faceted morphology using $BaCl_2$ as Ba-source compared with $Ba(OH)_2$. Cai et al. [8] described a synthesis using $Ba(NO_3)_2$ and titanium (IV) *n*-butoxide in a water-1-butanol mixture with KOH as a mineralizer. Reactions at 135 °C for 16 h gave cube-like BT particles, with a size of around 10 nm. The size of the nanoparticles could be controlled by the Ba:Ti ratio in the precursor solution. Li et al. [10] used $BaCl_2$ and $TiCl_4$ in a water-ethanol mixture with KOH as a mineralizer and obtained spherical BT nanoparticles after reactions at 230 °C for 12 h.

Obtaining insight into the nucleation and growth mechanism of the nanoparticles will facilitate control of the size and morphology of the final product, which is of great importance for the full utilization of the hydrothermal method. A few works have focused on describing the nucleation and growth mechanisms of BT from hydrothermal synthesis, often using the Johnson-Mehl-Avrami equation [11]:

$$f = 1 - \exp\left(-k(t - t_0)^n\right) \tag{1}$$

Here, f is the fractional extent of the reaction as a function of time (t) after the first appearance of the phase (t_0), k is a rate constant, and n is an exponent linked to the growth mechanism [11]. This model is derived for solid state reactions, but have also been successfully used for hydrothermal growth [12–14]. Ex situ studies are most often employed, where the reaction is quenched at various reaction times. Hertl [15] studied the hydrothermal reaction between TiO_2 and $Ba(OH)_2$, and suggested that the rate limiting factor was a topochemical reaction of Ba^{2+} with TiO_2 at the surface of TiO_2, with an activation energy of 105.5 kJ/mol. Similar conditions were investigated by Eckert et al. [16], who suggested two growth regimes: A dissolution-precipitation mechanism at the early stage and in situ transformation at a later stage. A limited number of data points makes it challenging to draw such conclusions as an initial nucleation and growth mechanism could occur before the dissolution-precipitation step [16]. Özen et al. [17] studied the formation of BT from a peroxo-hydroxide precursor (single source precursor for BT) in a NaOH solution. A clear change in the rate limiting step was reported as a function of temperature, but few data points make it challenging to deduce the mechanism. Still, a dissolution-precipitation mechanism was proposed. An increased reaction rate was observed with increasing temperature and an activation energy of 43.2 kJ/mol was reported.

The challenge in finding the growth mechanism from few data points and possible side effects of quenching can be overcome by following the reactions in real time through in situ experiments at synchrotron or neutron facilities. However, only a limited number of in situ studies of hydrothermal synthesis have been reported [18–20], with only two focusing on BT [21,22]. Walton et al. [21] followed the reaction between anatase and $Ba(OD)_2$ in D_2O by in situ neutron scattering. Here, a dissolution-precipitation mechanism was found as the rate limiting step, with an activation energy of 55 kJ/mol. Philippot et al. [22] used in situ X-ray diffraction to study the formation of BT from barium (II)- and titanium (IV)-isopropoxide in a water-ethanol mixture, with a time resolution of 5 s. Two growth regimes were suggested for the BT nanoparticles, an initial nucleation and growth limited mechanism with a high growth rate, followed by a dissolution-precipitation mechanism with a lower growth rate.

In this work, we present, for the first time, an in situ synchrotron X-ray diffraction study of a facile *aqueous* hydrothermal synthesis route to nanostructured BT using two different precursors, an amorphous titania precipitate slurry and a Ti-citric acid complex solution. Diffraction data with a time resolution down to 0.1 s at different temperatures (100, 125, and 150 °C) enabled the study of kinetics and growth in detail, demonstrating that the two precursors behave differently at low temperatures, but show similar characteristics at higher temperatures. From the amorphous titania precursor, nanocrystalline BT formed and stopped growing within 15 s at 150 °C, which, to the authors' knowledge, is the fastest that is reported in the literature for the hydrothermal synthesis of BT. Finally, the possible effect on the size and morphology of the nanoparticles by adding the surfactants, sodium dodecylbenzenesulfonate (SDBS) and ethylene glycol (EG), were investigated for the intermediate temperature.

2. Materials and Methods

2.1. Synthesis

The two different titanium precursors for the synthesis of the BT nanoparticles are described in the following. Titanium (IV) isopropoxide (TIP, Sigma-Aldrich, Oslo Norway, ≥97%) was mixed with distilled water under continuous stirring, forming a white amorphous Ti-OH precipitate with a Ti concentration of 0.3 M. Barium nitrate (Sigma-Aldrich, Oslo Norway, ≥99%), giving a 1:1 Ba:Ti-ratio, was then dissolved under continuous stirring, before the pH was raised to >14 by adding potassium hydroxide (KOH, Sigma-Aldrich, Oslo Norway, 80%). A slurry with a white precipitate was obtained. The KOH was mixed into the solution, while the solution was cooled in an ice-water bath. When used, both ethylene glycol (EG, Sigma-Aldrich, Oslo Norway, >99%) and sodium dodecylbenzenesulfonate (SDBS, Sigma-Aldrich, Oslo Norway, technical grade) were added in a 1:1 mole ratio with Ti before KOH. Experiments from this route will be referred to as *Ti-slurry* (from the titanium slurry used as the titanium source) experiments.

For the other titanium precursor, TIP was dissolved in a 1.5 M citric acid solution (CA, Sigma-Aldrich, Oslo Norway, ≥99%) at 60 °C under continuous stirring, making a clear 0.43 M Ti complex solution. The pH was then increased from around 1, to pH = 5–6 by adding aqueous ammonia (Sigma-Aldrich, Oslo Norway, 25 wt % solution). Barium nitrate (Sigma-Aldrich, Oslo Norway, ≥99%), giving a 1:1 Ba:Ti-ratio, was then dissolved under continuous stirring, forming a clear solution. The pH was raised to >14 by adding potassium hydroxide (KOH, Sigma-Aldrich, Oslo Norway, 80%), resulting in the formation of a white precipitate. As for the Ti-slurry experiments, the surfactants, EG and SDBS, were included before KOH when used and in a 1:1 mole ratio with Ti. Experiments from this route will be referred to as *Ti-CAsol* (from the titanium-CA solution used as a titanium source) experiments. Approximately 5 mL of precursor was prepared for each experiment, for both the Ti-slurry and Ti-CAsol. An overview of the synthesis parameters for the experiments conducted in this work are presented in Table 1.

Table 1. Overview of sample names, temperature, pressure, X-ray wavelength, and time resolution for the in situ X-ray diffraction experiments. Also, indicated is the surfactants used for each experiment and the final product.

Name [a]	Temperature [°C]	Pressure [bar]	EG	SDBS	Wavelength [b] [Å]	Time Resolution [c] [s]	Final Product
Ti-slurry-100	100	200	no	no	0.7242	0.1	BT
Ti-slurry-125	125	200	no	no	0.7242	0.1	BT
Ti-slurry-150	150	200	no	no	0.7242	0.1	BT
Ti-slurry-EG	125	200	yes	no	0.7242	0.1	BT
Ti-slurry-SDBS	125	200	no	yes	0.7762	0.1	BT
Ti-CAsol-100	100	200	no	no	0.7129	10	BT + BC
Ti-CAsol-125	125	200	no	no	0.7129	5	BT
Ti-CAsol-150	150	200	no	no	0.7129	5	BT
Ti-CAsol-EG	125	200	yes	no	0.7242	5	BT + BC
Ti-CAsol-SDBS	125	200	no	yes	0.7129	5	BT

[a] Ti-slurry and Ti-CAsol refers to the use of Ti-slurry and Ti-CAsol, respectively, for the titanium precursor. [b] Experiments conducted at different beam times, therefore, different wavelengths. [c] Time for collection of each 2D image file for the experiment. Exposure time was optimized for the different reaction speeds.

2.2. Characterization

The in situ X-ray diffraction experiments were performed at three different beam times using the Swiss-Norwegian Beamlines (BM01A) at the European Synchrotron and Radiation Facility (ESRF), Grenoble, France. The experiments were conducted in transmission mode, using the PILATUS@SNBL platform [23]. The experimental setup is described elsewhere [18,24,25]. In short, it consists of a single crystal sapphire capillary (1.15 ± 0.1 mm outer and 0.8 ± 0.08 mm inner diameter) that is pressurized with a high-pressure liquid chromatography (HPLC) pump and heated with a high temperature heat blower with nitrogen flow. The heat blower was heated to the desired set-point temperature and directed away from the capillary before being moved into position by a stepper motor. The set

point temperature was reached within 15 s. Heating profiles at selected temperatures are presented in Figure S1, with a description of the temperature calibration. The slurries were injected into the capillary quickly after preparation (1–2 min) to avoid $BaCO_3$ (BC) formation using a plastic syringe. All experiments were run until no changes were observed in the diffraction patterns (no change in intensity and/or peak width), varying from a few minutes to several hours.

All raw data frames were treated by masking parasitic regions (to remove shadow of beam stopper and diffraction spots from capillary) and integrated from 2D images to 1D diffractograms using *Bubble* (version 2017.10.23) [23]. The refinements were done using *TOPAS* (Bruker AXS version 5) in launch mode, with *jEdit* (version 4.3.1) as the text editor for writing macros for *TOPAS* [26]. The instrumental broadening was calibrated using a NIST 660a LaB_6 standard, fitted with the modified Thomson-Cox-Hastings pseudo-Voigt peak shape [27] and the "Simple Axial Model" supplied with *TOPAS*. For the refinements, zero error, scale factor, lattice parameter, Lorentzian isotropic size and strain parameter, isotropic thermal parameters for Ba and Ti, and a 25th order Chebyshev polynomial (to account for the broad background peak of water and solutes) were refined for each frame. The tetragonal unit cell of BT, being almost cubic, combined with the peak broadening from the nanosized BT made it impossible to differentiate between cubic and tetragonal space groups. The cubic space group (no. 221, $Pm\bar{3}m$) was, thus, chosen for describing BT in all experiments, using ICDD card #01-074-4539 as a reference.

3. Results

Typical color map plots for the Ti-slurry-150 and Ti-CAsol-150 experiments are presented in Figure 1a,b, respectively. For both experiments, BT forms directly from the amorphous precursor without intermediate phases and BT is the only phase appearing during the experiments. BT forms faster for the Ti-slurry (seconds) experiment than for the Ti-CAsol (minutes) experiment, which is a general trend for all reaction conditions and additives used.

The diffraction lines showed significant peak broadening, indicating nanosized crystallites. Anisotropic peak broadening and/or abnormal intensities were not observed, indicating nanosized spherical crystallites [25,28]. See Figure S2 for typical diffraction patterns and Rietveld refinements and Figure S3 for STEM images of Ti-CAsol-125 showing agglomerated spherical BT nanoparticles, with a size of <30 nm. A further discussion of the results using the two different precursors are provided in the following.

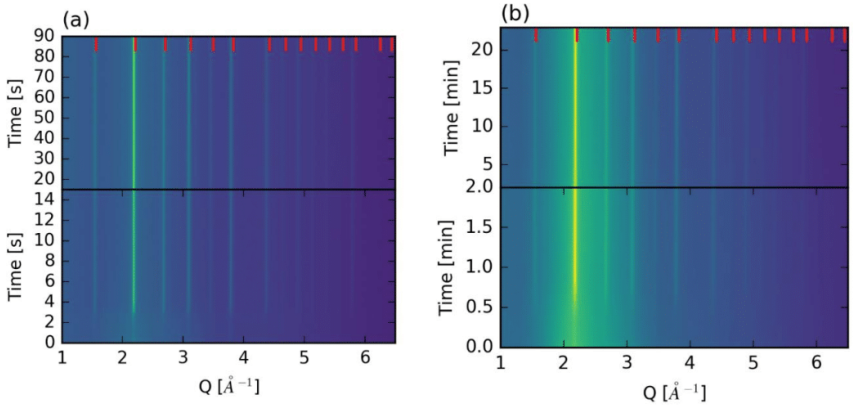

Figure 1. Color map plots showing the formation of $BaTiO_3$ at 150 °C and 200 bar (colors yellow-blue show intensity from high to low): (**a**) Ti-slurry-150 and (**b**) Ti-CAsol-150. Red markers show diffraction lines for bulk cubic $BaTiO_3$ at RT from ICDD card #01-074-4539, and the offset is an effect of temperature and finite-size effects. Notice the different time scales.

3.1. Ti-Slurry

Figure 2a–d shows the time resolved refined parameters for the Ti-slurry (scale factor, lattice parameter, crystallite size and strain) experiments at different temperatures. By increasing the reaction temperature, a small increase in the formation and growth rate is observed. The crystallite size stabilizes at around 15 nm after around 15 s at all three temperatures. The lattice parameter and strain are slightly decreasing, with an increasing reaction temperature from 4.0612(3) to 4.0587(2) Å and 1.27(7) $\times$ 10^{-3} to 0.94(3) $\times$ 10^{-3}, respectively, when increasing the temperature from 100 to 150 °C.

Comparing the experiments with EG or SDBS as surfactants at 125 °C, there is no influence on the reaction rate. However, EG gives a small decrease in crystallite size (8.7(2) nm), while the presence of SDBS almost doubles the crystallite size (25.0(7) nm). The strain is similar for both EG and SDBS, but the decrease in strain is significantly slower for the Ti-slurry-EG. The lattice parameter for BT prepared in the Ti-slurry-EG is larger than for the Ti-slurry-SDBS, which can be directly linked to the size difference. The time resolved refined parameters (scale factor, lattice parameter, crystallite size and strain) for Ti-slurry-EG and Ti-slurry-SDBS are presented in Figure 2e-h.

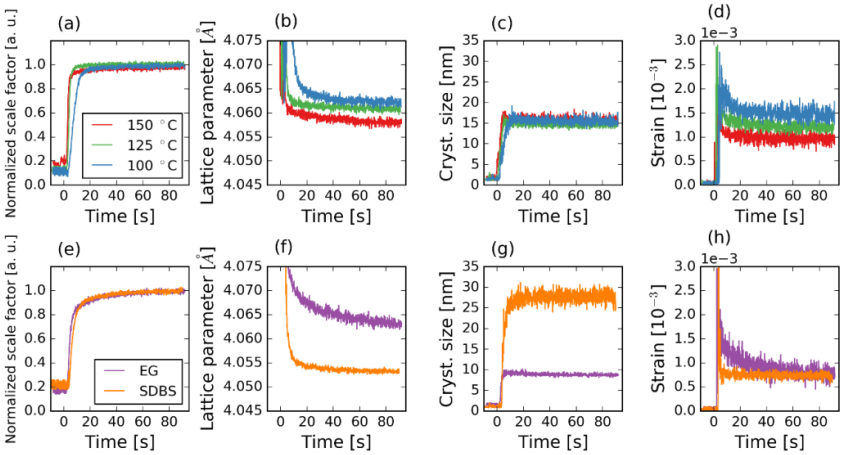

Figure 2. Time resolved refined values for the experiments with the Ti-slurry, showing scale factor (**a**,**e**), lattice parameter (**b**,**f**), crystallite size (**c**,**g**), and strain (**d**,**h**): (**a**–**d**) Ti-slurry-150, Ti-slurry-125, and Ti-slurry-100; (**d**–**g**) Ti-slurry-EG and Ti-slurry-SDBS at 125 °C. Scale factor is normalized to last value.

3.2. Ti-CAsol

The time resolved refined parameters (scale factor, lattice parameter, crystallite size, and strain) for the Ti-CAsol experiments at different temperatures are presented in Figure 3a–d. The three different temperatures yielded a significant difference in reaction rates, see scale factor in Figure 3a, where the amount of BT stabilized after 2, 10, and 200 min for reactions at 150, 125, and 100 °C, respectively. The final lattice parameter, crystallite size, and strain are not influenced significantly by the temperature, only the time for reaching the steady-state condition is influenced by temperature. The final values for Ti-CAsol-150 are 4.0502(2) Å, 12.5(2) nm, and 0.63(5) $\times$ 10^{-3} for the lattice parameter, crystallite size, and strain, respectively (the final values for Ti-CAsol-100 and Ti-CAsol-125 are found in Table S1). The final values for the lattice parameter are smaller for the Ti-CAsol compared to the Ti-slurry.

The surfactant SDBS (at 125 °C) does not have a significant effect on the reaction rate or the final product, as can be seen by comparing Ti-CAsol-125 (Figure 3a-d) with Ti-CAsol-SDBS (Figure 3e-h). In the case of using EG, BC is formed before BT, effectively delaying the formation and growth of BT. The final parameters for the BT phase, in the case of Ti-CAsol-EG, are comparable to that of Ti-CAsol-125, as can be seen in Table S1.

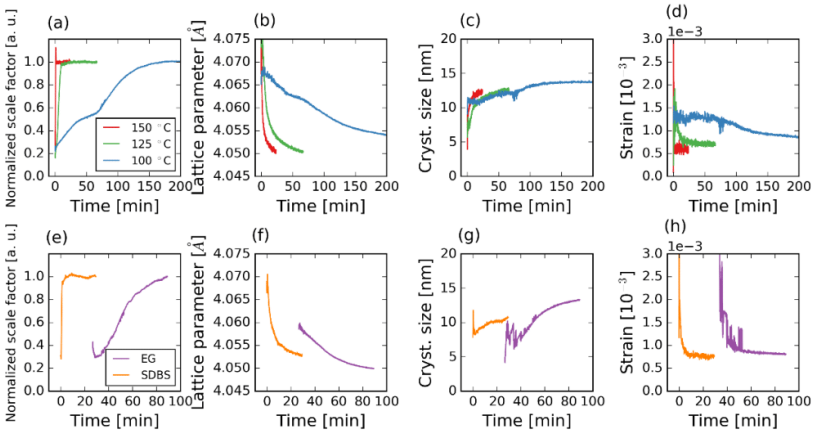

Figure 3. Time resolved refined values for the experiments with the Ti-CAsol, showing scale factor (**a**,**e**), lattice parameter (**b**,**f**), crystallite size (**c**,**g**), and strain (**d**,**h**): (**a**–**d**) Ti-CAsol-150, Ti-CAsol-125, and Ti-CAsol-100; (**e**–**h**) Ti-CAsol-EG and Ti-CAsol-SDBS at 125 °C. Scale factor is normalized to last value. Values for Ti-CAsol-EG are only plotted from around 20 min, since this is when BT formed.

3.3. Atomic Displacement Parameters

The isotropic Debye-Waller factor (B_{iso}) obtained from X-ray diffraction show the effect of the configurational static disorder and thermal vibration of atoms (dynamic disorder), and can give information about the ordering-disordering of a material [29]. The refined isotropic atomic displacement parameters for Ba and Ti (ADPs, B_{iso}) are presented in Figure 4a and b for Ti-slurry-150 and Ti-CAsol-150, respectively (ADPs for all experiments are presented in Figure S4, and Ti-CAsol-150 and Ti-slurry-150 are chosen here as representative examples). A fast reduction in the ADP for both Ba and Ti are observed at the early stage of the reaction, before the ADP stabilizes. This is a similar trend as is seen for the lattice parameter for both Ti-slurry-150 and Ti-CAsol-150. The ADP for Ti is higher than for Ba for both the Ti-slurry and Ti-CAsol experiments, which is consistent with similar works [22]. The main difference between Tisol-150 and Ti-CAsol-150 is the time scale, with Ti-slurry-150 showing a faster decrease and a shorter time for the ADPs to stabilize. The difference between the ADPs of Ti and Ba are smaller for the Ti-CAsol-150 than for Ti-slurry-150. A decrease in the final value for the ADP for Ti is observed with increasing temperature for both precursors. The opposite trend would be expected for a purely thermal effect, indicating less disordering, with increased reaction temperature. All refined values (scale factor, lattice parameter, size, strain, and B_{iso} for titanium and barium) for the last frame of all experiments are presented in Table S1.

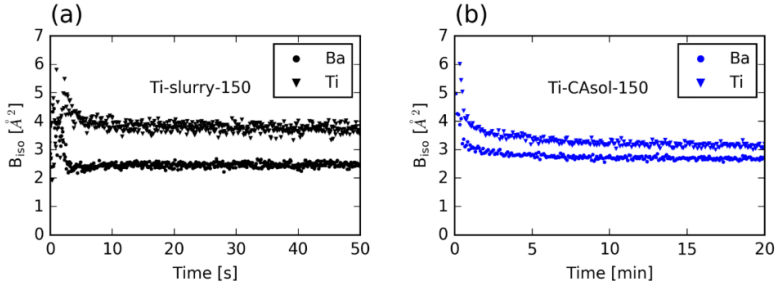

Figure 4. Isotropic atomic displacement parameters for Ba and Ti: (**a**) Ti-slurry-150 and (**b**) Ti-CAsol-150.

3.4. Kinetics of the Reactions

The scale factor of a phase is directly linked to the total amount of the corresponding phase. The scale factor can then be used to model the growth mechanism using Equation (1), with the normalized scale factor being the measure of the extent of the reaction [30]. Fits of Equation (1) to the scale factors are presented in Figure S5 and the refined values are summarized in Table 2. The Arrhenius plots for the Ti-slurry and Ti-CAsol experiments are presented in Figure 5a and the *n*-values from Equation (1) are plotted as a function of temperature in Figure 5b. The obtained activation energies are 22 and 41 kJ/mol for the Ti-CAsol and Ti-slurry, respectively (Table 2). The activation energy for the Ti-CAsol is approximately half that of the Ti-slurry, however, the uncertainty in the values is large.

The *n*-values for the Ti-slurry experiments fall into the same region for all temperatures (Figure 5b), showing a nucleation- and growth-controlled mechanism over the entire temperature range. The Ti-CAsol changes from a zero/first-order, or phase boundary-controlled mechanism, to a nucleation- and growth-controlled mechanism with increasing temperature.

Table 2. Fitted parameters for the growth of BT from in situ X-ray diffraction and the activation energy for the Ti-CAsol and Ti-slurry experiments.

Sample	k [s^{-1}]	n [a]	R^2 [a.u.]	E_a [kJ/mol]
Ti-slurry-100	0.0130(6)	2.1	0.99	
Ti-slurry-125	0.0126(6)	3.1	0.99	41
Ti-slurry-150	0.063(5)	2.3	0.97	
Ti-CAsol-100	0.00054(6)	0.9	0.97	
Ti-CAsol-125	0.00023(3)	1.5	0.99	22
Ti-CAsol-150	0.0013(4)	2.0	0.93	

[a] Values rounded to one decimal place.

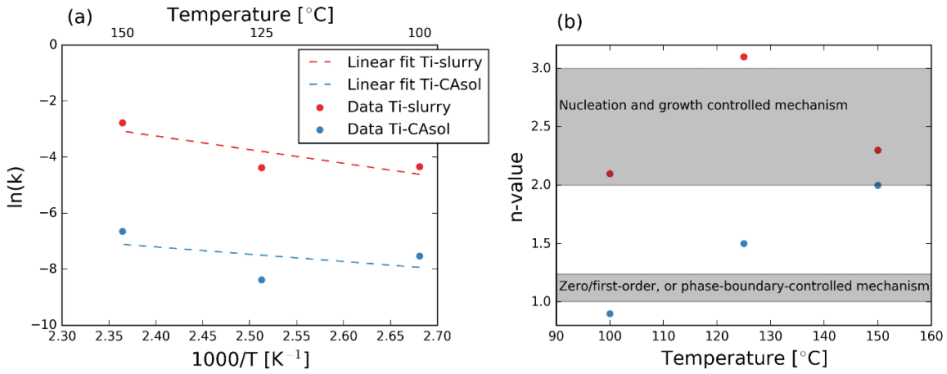

Figure 5. (**a**) Arrhenius plots for the Ti-slurry and Ti-CAsol with linear regression fits; (**b**) *n*-values plotted against temperature. Grey areas show physically meaningful values for *n*.

3.5. Phase Composition

All experiments yielded BT as the only or main phase. For Ti-CAsol-100, BT formed first followed by formation of BC, while BC formed before BT for the Ti-CAsol-EG. In both cases, BT was the main phase at the end of the experiment, with 88 and 95 wt % BT for Ti-CAsol-100 and Ti-CAsol-EG, respectively. No difference in the final results for the Ti-slurry experiments were observed with or without the mixing in ice bath. The only difference was the formation of BT immediately after adding KOH when not cooled, while BT formed during the experiments when mixing was done under cooling in an ice bath.

4. Discussion

Nanosized BT particles were successfully synthesized at a low temperature using two different titanium precursors and the reactions were followed in real time with in situ X-ray diffraction studies. The time resolved data demonstrated that, especially, the Ti-slurry precursor gives rapid BT formation compared to conventional autoclave synthesis (typical reaction times are in the range of hours and longer), but also compared with similar works [21,22]. The formation and growth of BT is finished in about 15 s for the Ti-slurry at 150 °C.

4.1. Kinetics

Comparing the results of the Ti-CAsol and the Ti-slurry shows that using citric acid to initially form a titanium-citric acid complex changes the reaction mechanisms. The reaction rate is higher for the Ti-slurry compared to the Ti-CAsol, which can be rationalized by an easier access to the Ti-atom. The *n*-values for the Ti-slurry indicate that it is the nucleation and growth that is the rate limiting step for all temperatures studied (see Figure 5b). On the other hand, the Ti-CAsol shows a nucleation and growth-controlled mechanism at 150 °C, but this changes into zero/first-order, or a phase boundary controlled mechanism, with decreasing temperature. In the works by Walton et al. [31], Eckert et al. [16], and Hertl [15], a *n* value of around 1 and a phase boundary mechanism as the rate limiting factor was reported, similar to the Ti-CAsol-100 in this work. The change to a nucleation and growth limiting mechanism, as seen in this work, with increasing temperature for the Ti-CAsol can be rationalized by an increased nucleation rate at higher temperatures. An increased nucleation rate is likely to be the reason the Ti-slurry behaving differently from the Ti-CAsol. We report here on different reaction mechanisms, depending on temperature and/or precursor, however, the final crystallite size is similar for all reactions (not including the experiments with surfactants). This could indicate that all reactions have a very high nucleation rate at the temperatures studied, which quickly depletes the precursors and limits further growth.

The activation energies calculated in this work are comparable to previously reported values of 105.5 [15], 43.2 [17], 55.1 [21], and 21 [32] kJ/mol. It should be noted here that direct comparison to the literature is difficult for kinetic studies, since these works cover different reaction conditions (temperatures, precursors, and solvents), which can, to some degree, explain the differences observed.

4.2. Refined Crystal Structure Parameters

It is clear from the refined values of size and strain that the peak broadening is mainly due to the size of the crystallites and not to any significant strain in the crystallites. Not many reports are found on Rietveld refinement of both size and strain on nanosized BT particles from wet chemical methods, since a wide Q-range is needed to differentiate between the two [33]. Size broadening is often assumed to be the dominant parameter and, thus, more often reported. Here, we show that this is the case by reporting small values of strain. BT, with a size of 30 nm, was prepared by Yan et al. from a high-gravity reactive precipitation method at 95 °C, with a refined strain value of 1.1×10^{-3}, which is comparable to the results in this work [34].

The lattice parameter evolution of BT for all experiments decreases initially before stabilization at around 4.05 Å, which is significantly higher than the bulk value for cubic BT at room temperature of 4.0094(2) Å [35] and 4.0126(2) Å at 150 °C [36]. The observed finite-size effect in lattice parameter is consistent with values observed in the literature of 4.03, 4.03, and 4.04 Å [21,22,34]. The large lattice parameter (4.05 Å compared to literature around 4.03–4.04 Å) seen in this work can be linked to the large disorder, as evident from the high B_{iso} values of titanium and barium. The values reported here (3–4 and 2–3 $Å^2$ at 150 °C for Ti and Ba, respectively) are higher than the values reported in similar works even at lower temperatures and similar crystallite sizes (2 and 1 $Å^2$ at 400 °C for Ti and Ba, respectively) [22]. This additional disorder can be the reason for the larger lattice parameter. The decreasing trend in B_{iso} for Ti in the Ti-slurry experiments with increasing temperature can also

explain the decrease in lattice parameter and strain observed. The difference between the strain and lattice parameters obtained for the Ti-slurry and Ti-CAsol experiments (values for Ti-CAsol are lower than of Ti-slurry) can be rationalized in the same way, with the difference in disorder (B_{iso} values of Ti-CAsol are lower than of Ti-slurry).

4.3. Effect of Surfactants

Almost a doubling of the crystallite size is observed when adding SDBS to the Ti-slurry, while a decrease is observed when adding EG. The differences observed for the lattice parameters is a direct effect of the different sizes, with the smaller sized Ti-slurry-EG giving a larger lattice parameter. The reaction rate seems to be unaffected by the presence of SDBS or EG. The main effect of the surfactants for the Ti-CAsol is that the presence of EG promotes the formation of BC, while only small changes are observed for the crystallite size and lattice parameter.

Hydrothermally synthesized $KNbO_3$ (KN) nanorods [37] and hierarchically nanostructured $PbTiO_3$ (PT) [38] have been reported when using SDBS as a surfactant (in combination with EG for PT). The results in this work do not suggest the formation of nanorods or hierarchical nanostructures, despite BT, KN, and PT all being perovskite oxides.

5. Conclusions

A thorough in situ X-ray diffraction investigation of a facile synthesis route of BT nanoparticles using two different titanium precursors was performed. Nanocrystalline BT (15 nm) forms within a few seconds or up to several hours, depending on the type of precursors and temperature. The relatively large lattice parameters (4.05 Å) are linked to significant disorder in the material, as evident from the large values of ADP of titanium and barium (3–4 and 2–3 $Å^2$ for Ti and Ba, respectively). Isotropic strain (1×10^{-3}) is shown to not be a significant contributor to the X-ray diffraction peak broadening. A kinetic study revealed that the two titanium precursors used behave similarly at high temperatures, but not at lower temperatures. This demonstrates the strength of in situ studies for understanding the nucleation and growth under hydrothermal conditions.

Supplementary Materials: The following are available online at http://www.mdpi.com/2073-4352/8/6/253/s1, Figure S1: Heating profiles for two different set-point temperatures (red (100 °C) and green (150 °C)). Blue data corresponds to 150 °C, but with the capillary moved 0.5 mm closer to the heat blower compared to the green data showing the robustness of this setup; Figure S2: Last frames of experiments Ti-CAsol-150 and Ti-slurry-150 showing typical refinements, with red markers showing diffraction lines of $BaTiO_3$ at RT from ICDD card #01-074-4539. Refined values (R-values, lattice parameter, size, strain and atomic displacement parameters) are reported in Table S1; Figure S3: SEM images of Ti-CAsol-125 at two different magnifications, showing agglomerated spherical $BaTiO_3$ nanoparticles with a size < 30 nm; Figure S4: Refined atomic displacement parameters for (a-b) Ti-slurry, and (c-d) Ti-CAsol experiments. (a) refined B_{iso} values for Ba; (b) refined B_{iso} values for Ti; (c) refined B_{iso} values for Ba; (d) refined B_{iso} values for Ti. Color-coding is as described in (a) for all panels; Figure S5: Normalized scale factor and fit to the Johnson-Mehl-Avrami equation for all samples used for the kinetic modeling; Table S1: Refined values (size, strain, lattice parameter, atomic displacement parameters for Ti and Ba and R-values) for the last frame from each experiment. Refinements were done using space group no. 221, $m\bar{3}m$, for $BaTiO_3$.

Author Contributions: O.G.G., S.M.S., T.G. and M.-A.E. conceived and designed the experiments; O.G.G., A.B.B., S.L.S. and W.v.B. performed the in situ X-ray diffraction experiments; O.G.G. performed the experiments and analyzed the data; O.G.G., and M-.A.E. wrote the paper with inputs from all the authors.

Funding: This research was funded by The Research Council of Norway grant numbers 250403 and 245936/F50".

Acknowledgments: Financial support from NTNU Norwegian University of Science and Technology and The Research Council of Norway under the Toppforsk program to the project (No 250403) "From Aqueous Solutions to oxide Thin films and hierarchical Structures" is gratefully acknowledged. The Research Council of Norway is acknowledged for the support to NTNU NanoLab through the Norwegian Micro and Nano-Fabrication Facility, NorFab, project number 245936/F50.

Conflicts of Interest: The authors declare no conflict of interest.

References

1. Varghese, J.; Whatmore, R.W.; Holmes, J.D. Ferroelectric nanoparticles, wires and tubes: Synthesis, characterisation and applications. *J. Mater. Chem. C* **2013**, *1*, 2618–2638. [CrossRef]
2. Villafuerte-Castrejon, M.E.; Moran, E.; Reyes-Montero, A.; Vivar-Ocampo, R.; Pena-Jimenez, J.A.; Rea-Lopez, S.O.; Pardo, L. Towards Lead-Free Piezoceramics: Facing a Synthesis Challenge. *Materials* **2016**, *9*, 27. [CrossRef] [PubMed]
3. Shandilya, M.; Rai, R.; Singh, J. Review: Hydrothermal technology for smart materials. *Adv. Appl. Ceram.* **2016**, *115*, 354–376. [CrossRef]
4. Gomes, M.A.; Lima, A.S.; Eguiluz, K.I.B.; Salazar-Banda, G.R. Wet chemical synthesis of rare earth-doped barium titanate nanoparticles. *J. Mater. Sci.* **2016**, *51*, 4709–4727. [CrossRef]
5. Modeshia, D.R.; Walton, R.I. Solvothermal synthesis of perovskites and pyrochlores: Crystallisation of functional oxides under mild conditions. *Chem. Soc. Rev.* **2010**, *39*, 4303–4325. [CrossRef] [PubMed]
6. Sun, W.; Pang, Y.; Li, J.; Ao, W. Particle Coarsening II: Growth Kinetics of Hydrothermal $BaTiO_3$. *Chem. Mater.* **2007**, *19*, 1772–1779. [CrossRef]
7. Inada, M.; Enomoto, N.; Hayashi, K.; Hojo, J.; Komarneni, S. Facile synthesis of nanorods of tetragonal barium titanate using ethylene glycol. *Ceram. Int.* **2015**, *41*, 5581–5587. [CrossRef]
8. Cai, W.; Rao, T.; Wang, A.; Hu, J.; Wang, J.; Zhong, J.; Xiang, W. A simple and controllable hydrothermal route for the synthesis of monodispersed cube-like barium titanate nanocrystals. *Ceram. Int.* **2015**, *41*, 4514–4522. [CrossRef]
9. Dutta, P.K.; Gregg, J.R. Hydrothermal synthesis of tetragonal barium titanate ($BaTiO_3$). *Chem. Mater.* **1992**, *4*, 843–846. [CrossRef]
10. Li, J.; Inukai, K.; Tsuruta, A.; Takahashi, Y.; Shin, W. Synthesis of highly disperse tetragonal $BaTiO_3$ nanoparticles with core-shell by a hydrothermal method. *J. Asian Ceram. Soc.* **2017**, *5*, 444–451. [CrossRef]
11. Avrami, M. Kinetics of Phase Change. I General Theory. *J. Chem. Phys.* **1939**, *7*, 1103–1112. [CrossRef]
12. Nørby, P.; Roelsgaard, M.; Søndergaard, M.; Iversen, B.B. Hydrothermal Synthesis of $CoSb_2O_4$: In Situ Powder X-ray Diffraction, Crystal Structure, and Electrochemical Properties. *Cryst. Growth Des.* **2016**, *16*, 834–841. [CrossRef]
13. Andersen, H.L.; Jensen, K.M.Ø.; Tyrsted, C.; Bøjesen, E.D.; Christensen, M. Size and Size Distribution Control of γ-Fe_2O_3 Nanocrystallites: An in Situ Study. *Cryst. Growth Des.* **2014**, *14*, 1307–1313. [CrossRef]
14. Eltzholtz, J.R.; Tyrsted, C.; Jensen, K.M.O.; Bremholm, M.; Christensen, M.; Becker-Christensen, J.; Iversen, B.B. Pulsed supercritical synthesis of anatase TiO_2 nanoparticles in a water-isopropanol mixture studied by in situ powder X-ray diffraction. *Nanoscale* **2013**, *5*, 2372–2378. [CrossRef] [PubMed]
15. Hertl, W. Kinetics of Barium Titanate Synthesis. *J. Am. Ceram. Soc.* **1988**, *71*, 879–883. [CrossRef]
16. Eckert, J.O.; Hung-Houston, C.C.; Gersten, B.L.; Lencka, M.M.; Riman, R.E. Kinetics and Mechanisms of Hydrothermal Synthesis of Barium Titanate. *J. Am. Ceram. Soc.* **1996**, *79*, 2929–2939. [CrossRef]
17. Özen, M.; Mertens, M.; Snijkers, F.; Cool, P. Hydrothermal synthesis and formation mechanism of tetragonal barium titanate in a highly concentrated alkaline solution. *Ceram. Int.* **2016**, *42*, 10967–10975. [CrossRef]
18. Becker, J.; Bremholm, M.; Tyrsted, C.; Pauw, B.; Jensen, K.M.O.; Eltzholt, J.; Christensen, M.; Iversen, B.B. Experimental setup for in situ X-ray SAXS/WAXS/PDF studies of the formation and growth of nanoparticles in near- and supercritical fluids. *J. Appl. Crystallogr.* **2010**, *43*, 729–736. [CrossRef]
19. Sun, Y.; Ren, Y. In Situ Synchrotron X-ray Techniques for Real-Time Probing of Colloidal Nanoparticle Synthesis. *Part. Part. Syst. Charact.* **2013**, *30*, 399–419. [CrossRef]
20. Jensen, K.M.; Tyrsted, C.; Bremholm, M.; Iversen, B.B. In situ studies of solvothermal synthesis of energy materials. *ChemSusChem* **2014**, *7*, 1594–1611. [CrossRef] [PubMed]
21. Walton, R.I.; Millange, F.; Smith, R.I.; Hansen, T.C.; O'Hare, D. Real time observation of the hydrothermal crystallization of barium titanate using in situ neutron powder diffraction. *J. Am. Chem. Soc.* **2001**, *123*, 12547–12555. [CrossRef] [PubMed]
22. Philippot, G.; Jensen, K.M.O.; Christensen, M.; Elissalde, C.; Maglione, M.; Iversen, B.B.; Aymonier, C. Coupling in situ synchrotron radiation with ex situ spectroscopy characterizations to study the formation of $Ba_{1-x}Sr_xTiO_3$ nanoparticles in supercritical fluids. *J. Supercrit. Fluids* **2014**, *87*, 111–117. [CrossRef]
23. Dyadkin, V.; Pattison, P.; Dmitriev, V.; Chernyshov, D. A new multipurpose diffractometer PILATUS@SNBL. *J. Synchrotron Radiat.* **2016**, *23*, 825–829. [CrossRef] [PubMed]

24. Skjærvø, S.L.; Wells, K.H.; Sommer, S.; Vu, T.-D.; Tolchard, J.R.; van Beek, W.; Grande, T.; Iversen, B.B.; Einarsrud, M.-A. Rationalization of Hydrothermal Synthesis of $NaNbO_3$ by Rapid in Situ Time-Resolved Synchrotron X-ray Diffraction. *Cryst. Growth Des.* **2018**, *18*, 770–774. [CrossRef]
25. Dalod, A.R.M.; Grendal, O.G.; Skjærvø, S.L.; Inzani, K.; Selbach, S.M.; Henriksen, L.; van Beek, W.; Grande, T.; Einarsrud, M.-A. Controlling Oriented Attachment and in Situ Functionalization of TiO_2 Nanoparticles During Hydrothermal Synthesis with APTES. *J. Phys. Chem. C* **2017**, *121*, 11897–11906. [CrossRef]
26. Evans, J.S.O. Advanced Input Files & Parametric Quantitative Analysis Using Topas. *Mater. Sci. Forum* **2010**, *650*, 1–9. [CrossRef]
27. Thompson, P.; Cox, D.E.; Hastings, J.B. Rietveld refinement of Debye-Scherrer synchrotron X-ray data from Al_2O_3. *J. Appl. Crystallogr.* **1987**, *20*, 79–83. [CrossRef]
28. Dalod, A.R.M.; Henriksen, L.; Grande, T.; Einarsrud, M.-A. Functionalized TiO_2 nanoparticles by single-step hydrothermal synthesis: The role of the silane coupling agents. *Beilstein J. Nanotechnol.* **2017**, *8*, 304–312. [CrossRef] [PubMed]
29. Yoshiasa, A.; Nakatani, T.; Nakatsuka, A.; Okube, M.; Sugiyama, K.; Mashimo, T. High-temperature single-crystal X-ray diffraction study of tetragonal and cubic perovskite-type $PbTiO_3$ phases. *Acta Crystallogr. Sect. B* **2016**, *72*, 381–388. [CrossRef] [PubMed]
30. Peterson, K.M.; Heaney, P.J.; Post, J.E. A kinetic analysis of the transformation from akaganeite to hematite: An in situ time-resolved X-ray diffraction study. *Chem. Geol.* **2016**, *444*, 27–36. [CrossRef]
31. Walton, R.I.; Norquist, A.; Smith, R.I.; O'Hare, D. Recent results from the in situ study of hydrothermal crystallisations using time-resolved X-ray and neutron diffraction methods. *Faraday Discuss.* **2002**, *122*, 331–341. [CrossRef]
32. Ovramenko, N.A.; Shevts, L.I.; Ovcharenko, F.D.; Kornilovich, B.Y. Kinetics of Hydrothermal Synthesis of Barium Metatitanate. *IzV. Akad. Nauk SSSR Neorg. Mater.* **1979**, *15*, 1982–1985.
33. Balzar, D.; Audebrand, N.; Daymond, M.R.; Fitch, A.; Hewat, A.; Langford, J.I.; Le Bail, A.; Louer, D.; Masson, O.; McCowan, C.N.; et al. Size-strain line-broadening analysis of the ceria round-robin sample. *J. Appl. Crystallogr.* **2004**, *37*, 911–924. [CrossRef]
34. Yan, T.; Shen, Z.-G.; Zhang, W.-W.; Chen, J.-F. Size dependence on the ferroelectric transition of nanosized $BaTiO_3$ particles. *Mater. Chem. Phys.* **2006**, *98*, 450–455. [CrossRef]
35. Aoyagi, S.; Kuroiwa, Y.; Sawada, A.; Yamashita, I.; Atake, T. Composite Structure of BaTiO3 Nanoparticle Investigated by SR X-ray Diffraction. *J. Phys. Soc. Jpn.* **2002**, *71*, 1218–1221. [CrossRef]
36. He, Y. Heat capacity, thermal conductivity, and thermal expansion of barium titanate-based ceramics. *Thermochim. Acta* **2004**, *419*, 135–141. [CrossRef]
37. Wang, G.Z.; Yu, Y.D.; Grande, T.; Einarsrud, M.A. Synthesis of $KNbO_3$ Nanorods by Hydrothermal Method. *J. Nanosci. Nanotechnol.* **2009**, *9*, 1465–1469. [CrossRef] [PubMed]
38. Wang, G.; Rørvik, P.M.; van Helvoort, A.T.J.; Holmestad, R.; Grande, T.; Einarsrud, M.-A. Self-Assembled Growth of $PbTiO_3$ Nanoparticles into Microspheres and Bur-like Structures. *Chem. Mater.* **2007**, *19*, 2213–2221. [CrossRef]

CrystEngComm

PAPER

View Article Online
View Journal

Cite this: DOI: 10.1039/c9ce01049a

Composition and morphology tuning during hydrothermal synthesis of $Sr_xBa_{1-x}Nb_2O_6$ tetragonal tungsten bronzes studied by *in situ* X-ray diffraction†

Ola G. Grendal,[a] Anders B. Blichfeld,[a] Tuong D. Vu,[a] Wouter van Beek,[b] Sverre M. Selbach,[a] Tor Grande[a] and Mari-Ann Einarsrud *[a]

Received 5th July 2019,
Accepted 6th September 2019

DOI: 10.1039/c9ce01049a

rsc.li/crystengcomm

Current interest in 1D ferroelectric materials calls for cheap, controllable, reproducible and environmentally friendly synthesis routes. Hydrothermal synthesis stands out as one of the most promising routes, but a thorough understanding of nucleation and growth mechanisms is needed for full utilization and control. Here, we present a new hydrothermal route for preparing $Sr_xBa_{1-x}Nb_2O_6$ (x = 0.32–0.82, SBN) tetragonal tungsten bronzes. The nucleation and growth of SBN were studied by a combination of *in situ* synchrotron X-ray diffraction and *ex situ* scanning electron microscopy (SEM). Based on the *in situ* X-ray diffraction data, a nucleation mechanism is proposed where an amorphous precursor consisting of clusters with a mix of edge- and corner-sharing NbO_6 octahedra undergoes gradual restructuring leading to more corner-sharing octahedra, before abrupt crystallization. For the first time, the Sr fraction in SBN was successfully tuned with a hydrothermal method, both by changing the Sr fraction in the precursor solutions and by changing the dielectric constant of the solvent. The morphology of SBN was successfully controlled by the synthesis temperature, where a low temperature (175 °C) resulted in rod-shaped particles (length ~1.5 μm and ~500 × 500 nm^2 cross section) and a higher temperature (300 °C) gave cube-shaped particles (~500 × 500 nm^2).

Introduction

Ferroelectric materials are an essential part of our technological society. In recent years, there has been increased interest in nanostructured,[1] especially one-dimensional (1D) nanostructured, ferroelectric materials.[2,3] These 1D materials are important for further development of *e.g.* non-volatile ferroelectric random-access memory (FeRAM), sensors and/or actuators in microelectromechanical systems (MEMS) and nanosized energy-harvesting devices and for fundamental research on finite-size effects on ferroelectric properties.[2,3] Cheap, controllable, reproducible and environmentally friendly synthesis routes are needed for these applications. Wet chemical methods,[4] especially hydrothermal synthesis, stand out as one of the most promising ways of producing 1D nanostructured ferroelectric materials.[2,5]

$Sr_xBa_{1-x}Nb_2O_6$ (x = 0.32–0.82, SBN) is a lead-free ferroelectric material with an unfilled tetragonal tungsten bronze (TTB) structure.[6–8] The behaviour of SBN can be tuned from normal ferroelectric to relaxor ferroelectric by

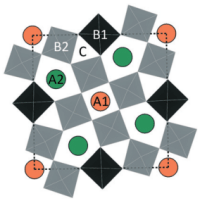

Fig. 1 Crystal structure of SBN seen along the *c* axis of the tetragonal cell. NbO_6 octahedra are indicated in black and grey (B1 and B2), the square A1 sites are orange, the pentagonal A2 sites are green and the triangular C sites are empty. One vacancy per unit cell, which is distributed on the A1- and A2-sites, is not shown. Figure made using VESTA.[24]

[a] *Department of Materials Science and Engineering, NTNU Norwegian University of Science and Technology, 7491 Trondheim, Norway. E-mail: mari-ann.einarsrud@ntnu.no*
[b] *Swiss-Norwegian Beamlines at European Synchrotron Research Facility, 38043 Grenoble, France*

† Electronic supplementary information (ESI) available: Figures showing selected temperature profiles. Typical input file and more details for the batch Rietveld refinement and representative fits. Validation of the Rietveld refinement model. Details about the TEM study. SEM images of all experiments. Summary of all refined values at the end of the experiments. Effect of the alkaline earth to niobium ratio on Rietveld refinements. See DOI: 10.1039/c9ce01049a

varying the Sr fraction,[9] and the Curie temperature (T_c) depends linearly on the Sr fraction and ranges from 60 to 230 °C.[10] In addition, SBN has good pyroelectric[11,12] and photorefractive properties.[13] Moreover, reduced SBN ($Sr_xBa_{1-x}Nb_2O_{6-\delta}$) is reported to have promising thermoelectric properties[14] and filled SBN ($Sr_xBa_{1.2-x}Nb_2O_6$) is reported to show low temperature superconductivity.[15] The crystal structure of SBN consists of corner-sharing NbO_6 octahedra forming triangular C-sites (empty in SBN), square A1-sites and pentagonal A2-sites[6,16] filled with a total of 5 alkaline earth atoms, and 1 vacancy, as shown in Fig. 1. The average structure is described by the *P4bm* space group, but a better understanding of the link between order/disorder, polarization and incommensurate tilting of NbO_6 octahedra in the structure is still being addressed.[16,17] The three species, ($(5 - x)Sr^{2+}$, xBa^{2+} and one vacancy) are distributed on a total of 6 sites per unit cell (2 A1- and 4 A2-sites), and one X-ray diffraction experiment is not sufficient to determine the occupancy of Ba^{2+}, Sr^{2+} and the vacancy on the two sites due to parameter correlations.[18] Therefore, it is often assumed that the larger Ba^{2+} can only occupy the larger A2-site, while Sr^{2+} can occupy both the A1- and A2-sites when doing Rietveld refinements,[6,19,20] but recently the possibility of cation vacancy disorder has been addressed with simulations[21,22] and experimentally.[23]

Several methods have been used to prepare SBN,[25] where the Czochralski technique is the most common for growing large single crystal SBN and for utilizing the optical properties of SBN.[7,9,26] SBN is also routinely made by solid-state synthesis using $BaCO_3$ or $Ba(NO_3)_2$, $SrCO_3$ and Nb_2O_5 and calcining at temperatures from 1200 to 1400 °C.[10,19,23] Other synthesis routes are also described, like combustion synthesis,[27] molten salt synthesis,[28] the urea method[29] and hydrothermal synthesis.[30] All these methods have one or several of the following drawbacks; high temperature, slow, involving the use of hydrofluoric acid in precursor preparation, or issues with reproducibility.

In this work, we present a new hydrothermal route for producing SBN studied with *in situ* synchrotron X-ray diffraction. The *in situ* experiments allow optimization of synthesis parameters, such as the reaction temperature and Sr fraction in the precursor, to suppress the formation of secondary phases. It is demonstrated for the first time that the composition (ratio between Sr and Ba) of SBN can be controlled with the hydrothermal method, and rod-, tube-, and cube-shaped particles were obtained for different reaction conditions.

Experimental

Synthesis

Nominal composition $Sr_xBa_{1-x}Nb_2O_6$ (x = 0.2–0.6) was prepared from strontium nitrate (Sigma-Aldrich, Oslo, Norway, 99.995%), barium nitrate (Sigma-Aldrich, Oslo, Norway, 99.999%) and niobium acid. The niobium acid was prepared by dissolving approximately 70 g of ammonium niobate(v) oxalate hydrate (Sigma-Aldrich, Oslo, Norway, 99.99%) in 700 mL distilled water under continuous stirring at 50 °C for 3–5 h until a clear solution was obtained. Then the pH was increased to 11 with addition of aqueous ammonia solution (Sigma-Aldrich, Oslo, Norway, 25 wt% solution) to precipitate niobium acid, forming a milky white dispersion/slurry. This mixture was stirred at room temperature (RT) for several days. The dispersion was centrifuged (11 300*g*/10 000 rpm for 15 min) and the collected precipitates were re-dispersed in 1 wt% ammonia solution. This centrifugation procedure was repeated 3 times to remove oxalate ions. After the final centrifugation, the precipitate was collected and re-dispersed in 125 mL 1 wt% ammonia solution, giving a final dispersion with pH 11. The niobium content of the niobium acid was standardized using thermogravimetric analysis at 800 °C. For each experiment, 5 mL of precursor was prepared by first weighing out niobium acid giving a final Nb concentration of 0.25 M. The pH was adjusted to 12.4 with 25 wt% ammonia solution (around 1.5 mL added), before dissolving stoichiometric amounts of strontium and barium nitrates (amounts varies with x). Finally, distilled water was added to give a total volume of 5 mL. An overview of the synthesis parameters for the experiments conducted is presented in Table 1.

Characterization

In situ X-ray diffraction experiments were performed at two different beam times at the Swiss-Norwegian Beamlines (BM01), European Synchrotron and Radiation Facility (ESRF), Grenoble, France. The experiments were conducted in transmission mode, using the PILATUS@SNBL platform.[31] The experimental setup is described elsewhere.[32–34] In short, the setup consists of a single crystal sapphire capillary (1.15 ± 0.1 mm outer and 0.8 ± 0.08 mm inner diameter, Crytur, Turnov, Czech Republic) which is pressurized with a high-pressure liquid chromatography (HPLC) pump (Shimadzu LC-10ADVP, Shimadzu Corporation, Kyoto, Japan). Heating was carried out with a high (max ~750 °C) temperature heat blower (Leister LE Mini 800, Kaegiswil, Switzerland) with a nitrogen flow. The heat blower was heated to the desired set-point temperature while being directed away from the capillary before being moved into position using a step motor. The set point temperature was reached within ~20 s. Heating profiles at selected temperatures are presented in Fig. S1 in the ESI,† with a description of the temperature calibration. The precursor slurry was injected into the capillary using a plastic syringe. All experiments were run until no more changes were observed in the diffraction patterns (in intensity and/or peak width).

All raw data frames were masked for parasitic regions (to remove shadow of the beam stop and diffraction spots from the single crystal capillary) and integrated from 2D images to 1D diffractograms using Bubble (version 2017.10.23).[31] The sequential batch refinements were performed using TOPAS (Bruker AXS version 5) in launch mode, with jEdit (version

Table 1 Overview of the experiment names, temperature, pressure, X-ray wavelength, time resolution and approximate experiment time for the *in situ* X-ray diffraction experiments; also, indicated is the final product

Name[a]	Temperature [°C]	Pressure [bar]	Wavelength[b] [Å]	Time resolution[c] [s]	Approx. total time of experiment [h]	Final product
SBN60_T300	300	200	0.77624	5	0.9	SBN, Pyro
SBN60_T225	225	200	0.77624	5	2.3	SBN, Pyro, Uknw
SBN60_T200	200	200	0.77445	5	3.7	SBN, Pyro
SBN50_T400	400	200	0.77624	5	1.3	SBN, Pyro
SBN50_T300	300	200	0.77624	5	0.7	SBN, Pyro
SBN50_T225	225	200	0.77624	5	2.1	SBN, Pyro, Uknw
SBN50_T200	200	200	0.77624	5	3.6	SBN, Uknw
SBN50_T175	175	200	0.77624	10	10.4	SBN, Uknw
SBN40_T300	300	200	0.77624	5	0.6	SBN
SBN40_T225	225	200	0.77624	5	1.3	SBN
SBN40_T200	200	200	0.77445	5	2.4	SBN
SBN30_T300	300	200	0.77445	5	0.6	SBN
SBN30_T225	225	200	0.77445	5	1.4	SBN
SBN30_T200	200	200	0.77445	5	2.6	SBN
SBN20_T300	300	200	0.77445	5	0.5	SBN
SBN20_T225	225	200	0.77445	5	2.2	SBN
SBN20_T200	200	200	0.77445	5	4.1	SBN
SBN50_supercrit	400	250	0.77624	2	3.0	SBN, Uknw

[a] The nomenclature is SBN*XX*_T*YYY*, where *XX* refers to the Sr mole fraction in the precursor times 100 and *YYY* is the reaction temperature. [b] Experiments were conducted at two different beam times, therefore, different wavelengths. [c] Exposure time for each 2D frame for the experiment. Exposure time was optimized for the different reaction rates.

4.3.1) as the text editor for writing macros for TOPAS.[35] The instrumental broadening was calibrated using a NIST 660a LaB_6 standard, fitted with the modified Thompson–Cox–Hastings pseudo-Voigt peak shape[36] provided within TOPAS. A typical starting model (input-file in TOPAS) and a detailed description of the model used for the refinements are shown in the ESI,† in addition to a typical graphical representation of a Rietveld refinement in Fig. S2.† To validate the refined values for the Sr fraction, a reference using a data set of SBN made by solid-state synthesis provided by Aamlid *et al.* was used.[23] A full description of this calibration is presented in the ESI,† with the Rietveld refinement profiles in Fig. S3.† In short, the results show that the extracted lattice parameters follow what is expected for the given nominal compositions, and that the extracted Sr fractions show the expected trend, but the nominal Sr fraction is underestimated. The nominal Sr fraction is more underestimated for high Sr fractions, as seen in Fig. S4.† Based on this, the Sr fractions presented in this work can be used to show relative differences between the experiments but are not considered to reflect the true Sr fractions. In this work, it is assumed that stoichiometric SBN is formed during the hydrothermal synthesis ($Sr_xBa_{1-x}Nb_2O_6$), and is not a filled or reduced version. This has not been verified, and the possibility of non-stoichiometry is briefly discussed.

After the *in situ* diffraction experiments, the samples were collected for *ex situ* scanning electron microscopy (SEM) imaging. An in-lens cold field emission S(T)EM Hitachi S-5500 with an acceleration voltage of 7 keV was used, and secondary electrons were detected. The samples were prepared by dropping a diluted aqueous dispersion of the collected samples onto an aluminium sample holder, which was then dried for 6–7 h at RT. The nature of the experimental setup makes it impossible to separate completely SBN from the precursor, so both the unreacted amorphous precursor and crystalline products were observed.

Results

Phase purity and phase development

Phase pure SBN was obtained for all reaction temperatures in the case of SBN20, SBN30 and SBN40, as presented in Table 1 and shown in Fig. 2(a). In the case of SBN50 and SBN60, two secondary phases were observed, a pyrochlore phase (referred to as Pyro) and a phase that has not been identified (referred to as Uknw), in addition to SBN. The Pyro phase was shown to be Sr-rich compared to SBN by transmission electron microscopy (TEM, description and experimental details in the ESI†). A Pawley fit[37] of the diffractogram of the Pyro phase using the cubic space group $Fd\bar{3}m$ gave a lattice parameter of ~10.55 Å, which was also used further in the Rietveld refinements. Here, the lattice parameter was refined for the last frame, and then kept fixed for the batch refinement. No space group was found for the Uknw phase and single peak phases with fixed positions were used (positions fixed to refined values from the last frame). Satisfactory Rietveld refinement could not be achieved with all the phases present and a quantitative analysis was not possible, but the general trends based on the relative intensities are the increasing amount of secondary phases with increasing Sr fraction in the precursor and with increasing temperature. In all experiments where SBN and Pyro were formed, SBN always formed prior to the Pyro phase before the amount of both phases increased and then

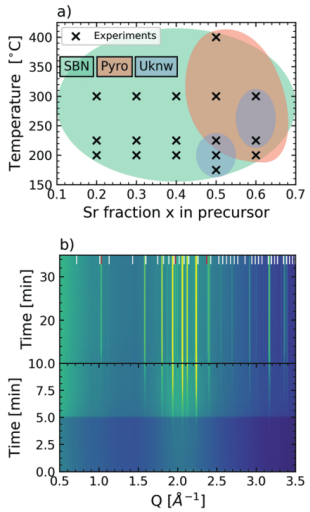

Fig. 2 "Phase formation diagram" as a function of Sr fraction x in the precursor and temperature (a), with crosses indicating experiments in this work. Phase pure SBN is indicated in green (9 experiments), a mixture of SBN and Pyro in orange (3 experiments) and a mixture of SBN and Uknw in blue (2 experiments). The overlapping green, orange and blue indicate a mix of SBN, Pyro and Uknw (3 experiments). Contour plot (b) of SBN50_T300 showing formation of SBN and Pyro from an amorphous precursor without any intermediate phases. White bars show theoretical *hkl* values for SBN at RT, and red bars show the three most intense *hkl* values for Pyro. For this particular experiment, SBN formed after ~3 min and Pyro after ~10 min.

stabilized. In the experiments where SBN and the Uknw phase were formed, the Uknw phase always formed first before the amount of both phases increased simultaneously before stabilizing. The amounts of neither Pyro nor the Uknw phase decreased due to formation of SBN.

The formation of SBN from the amorphous precursor proceeded without crystalline intermediates as shown in Fig. 2(b). The only exception was the experiments where the Uknw phase was formed. A temperature-dependent incubation period ranging from a few minutes at high temperatures to ~2 h at the lowest temperature is observed before crystallization in all experiments. After the incubation period, the formation and growth of SBN was seemingly fast. This is based on attempts at refining crystallite sizes on the first frames right after SBN formation giving values in the range of 50–100 nm (indicating rapid growth).

Reaction kinetics

The Johnson–Mehl–Avrami (JMA) equation, eqn (1), was derived for modelling the kinetics of solid state reactions,[38] but has also been utilized for kinetic studies of hydrothermal reactions.[39–41] In the JMA equation, f is the fractional extent of the reaction as a function of time (t) after the first appearance of the phase, k is a rate constant and n is an exponent linked to the growth mechanism.[38] Plotting $\ln(k)$ against the inverse of temperature gives a straight line (assuming that the model describes the reaction sufficiently well) with a slope that gives the activation energy of the reaction.

$$f = 1 - \exp(-kt^n) \quad (1)$$

In Fig. 3(a), $\ln(k)$ is plotted as a function of inverse temperature, and n values are presented in Fig. 3(b). The values (k and n) are obtained by fitting the JMA equation to the time resolved normalized scale factors, which can be used as a measure of the extent of the reaction (f).[42] The $\ln(k)$ values are clustered together, but they do not form straight lines for the individual sets of experiments (SBN20, SBN30, *etc.*), thus activation energies are not possible to extract, and the origin of this is hypothesized in the discussion section. The n values are between 2 and 3.5 indicating a nucleation- and growth controlled-mechanism for all conditions investigated in this work, providing valuable insight into the growth mechanism of SBN under hydrothermal conditions.

Crystal structure information from Rietveld refinement

The refined Sr fraction in SBN at the end of the experiments is presented in Fig. 4 as a function of reaction temperature and Sr fraction x in the precursor. No clear trends were observed as a function of temperature, although a small decrease in the Sr fraction with increasing temperature can be recognized. For all temperatures and Sr fractions in the precursors, the refined Sr fraction is found to be around 0.35 ± 0.1, except for SBN50_supercrit, which stands out with a Sr fraction x from the refinement of 0.6. With increasing Sr fraction in the precursors, a close to linear increase in the refined Sr fraction is observed for Sr fractions of 0.2 to 0.5, followed by a decrease going from 0.5 to 0.6. The linear increase does not follow a 1 : 1 relationship between the Sr fraction in the precursor and the Sr fraction from the Rietveld refinement.

The a- and c-lattice parameters from the Rietveld refinements at the end of the experiment are plotted against

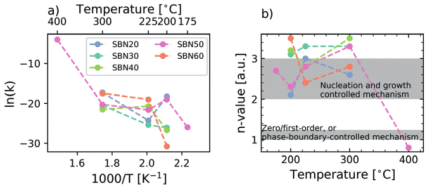

Fig. 3 Arrhenius plot (a) and n values (b) obtained from fitting the JMA equation to the time resolved normalized scale factors.

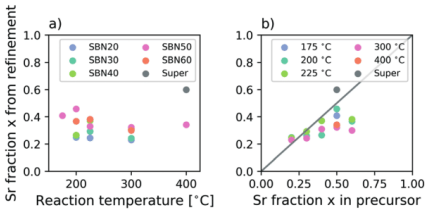

Fig. 4 Sr fraction x from the Rietveld refinement at the end of the experiments as a function of reaction temperature (a) and Sr fraction x in the precursor (b). Gray line in (b) indicates a 1:1 relationship between Sr fraction x in the precursor and from the refinement.

the reaction temperature and the Sr fraction in the precursor as shown in Fig. S6 in the ESI.† No clear overall trend as a function of reaction temperature is observed. A minor decrease in a and a small increase in c as a function of temperature is observed for each data set. The refined a lattice parameter increases while c decreases as a function of Sr fraction in the precursor in the range of 0.2 to 0.5.

Disorder and/or non-stoichiometry

Nonphysical atomic displacement parameters (ADPs, B_{iso} values equal to 0) for the A1-site resulted from refinements for some of the experiments as presented in Fig. 5(a), where the B_{iso} of the A1-site is plotted against the Sr fraction. The B_{iso} value for the A1-site was constrained to be positive or 0 during the refinements. If the B_{iso} value was refined without this constraint, the value would return negative for the cases where the B_{iso} now equals 0. The nonphysical B_{iso} values only occur for the experiments with the lowest refined Sr fractions. The fractional occupancy of Sr on the A1-site is presented in Fig. 5(b). The Sr occupancy on the A1-site is perfectly linear and follows the upper limit for Sr occupancy as restricted by the Rietveld refinement up to a Sr fraction of ~0.4. All refined parameters and R values at the end of all experiments in this work are presented in Table S2 in the ESI.†

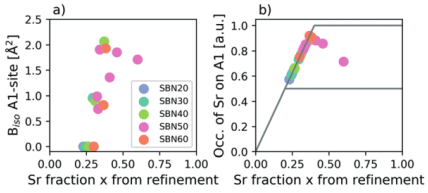

Fig. 5 B_{iso} for the A1-site (a) and fractional occupancy of Sr on the A1-site (b) as a function of Sr fraction from the Rietveld refinement. Grey lines show the minimum and maximum occupancy of Sr on the A1-site given the Rietveld refinement. For Sr fractions lower than 0.2, the minimum and maximum Sr occupancies on the A1-site are identical since Ba occupies all A2-sites (follows from the assumption that Sr + Ba = 5, and all Ba is locked to the A2-site).

Size and morphology of SBN

The SEM images of SBN50 at different reaction temperatures are presented in Fig. 6. Rod-shaped particles with a length of ~1.5 μm and a ~500 × 500 nm^2 cross section are observed for SBN50_T175. With increasing temperature, the aspect ratio decreases, and for SBN50_T300, SBN50_T400 and SBN50_supercrit, only cube-shaped SBN is observed (~500 × 500 nm^2). A decrease in the aspect ratio with increasing reaction temperature is also observed for the other compositions except for SBN20, as seen in Fig. S7 in the ESI.† In Fig. 7, the SEM images of SBN formed at 300 °C with varying Sr fractions are presented. Here, cube-shaped SBN with a similar size (500 × 500 nm^2) is observed for all Sr fractions except for SBN20_T300. For SBN20_T300, tubes with a rectangular cross section are observed.

In some of the SEM images, smaller bipyramids are observed (especially visible in SBN60_T300 and SBN50_T225), which is the Pyro phase. The Pyro phase forming bipyramids was determined by TEM (see the ESI†). No features in the SEM images could be ascribed to the Uknw phase. From the *in situ* diffraction experiments, the Uknw phase appeared as strong spots on the detector (not full diffraction cones on the 2D detector, which indicates large and few crystallites), which can explain why it has not been found in the SEM images.

Discussion

Phase pure SBN particles were successfully synthesized with the new hydrothermal route presented in this work. This work demonstrates that the morphology of SBN can be modified by varying the reaction temperature, and that the composition of the final SBN can be tuned with the Sr fraction in the precursor and the dielectric constant of the solvent, through changes in temperature and pressure.

Nucleation and growth of SBN

The time-dependent X-ray diffraction results show that a temperature-dependent incubation period is needed before the nucleation of SBN occurs, and that the first observed crystallites are relatively large (~50 nm) and hence the growth rate is fast. Similar characteristics have been reported for the formation of WO_3 under hydrothermal conditions by Saha *et al.*[43] WO_3, with the archetype *P6/mmm* crystal structure for tungsten bronzes (TBs), has a crystal structure strongly related to SBN. The amorphous precursor consisting of clusters with a mix of corner- and edge-sharing WO_6 octahedra was demonstrated by *in situ* X-ray total scattering with pair distribution function (PDF) analysis. When heat was applied, a gradual decrease in the signature of the edge-sharing octahedra was observed with a simultaneous increase in the signature of the corner-sharing octahedra, which are the only building blocks in TBs. Once most octahedra were corner-sharing, abrupt formation of crystalline particles was observed. Based on the results presented in this work and the similarities to the work of Saha *et al.*, a related formation

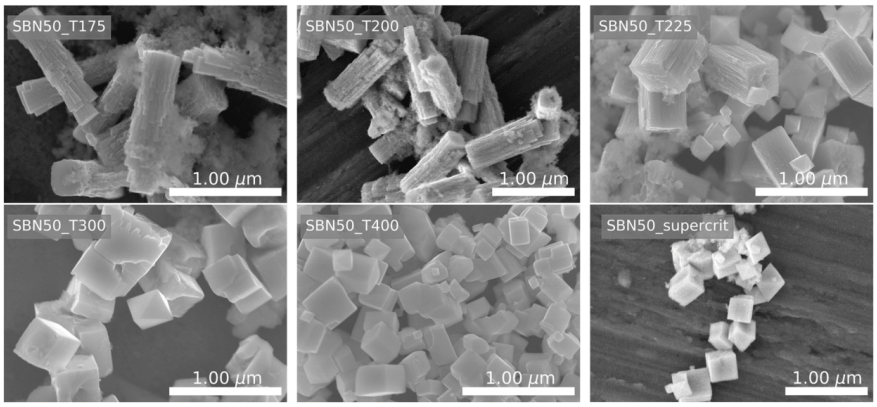

Fig. 6 SEM images of SBN particles made with a Sr fraction x in the precursor of 0.5 at different reaction temperatures: SBN50_T175, SBN50_T200, SBN50_T225, SBN50_T300, SBN50_T400 and SBN50_supercrit.

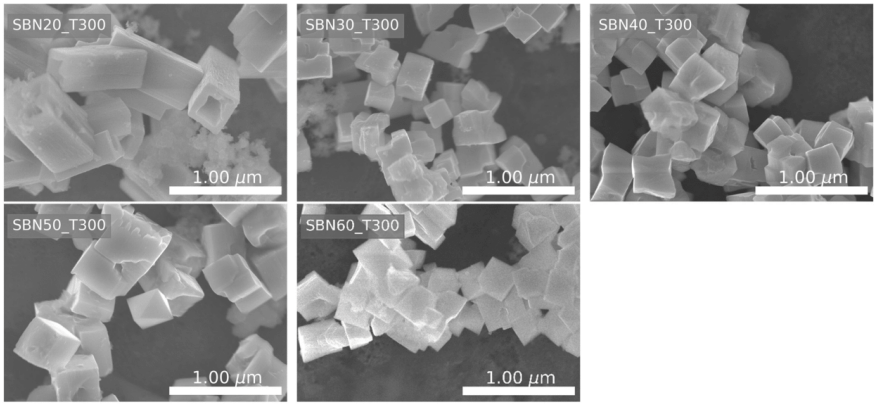

Fig. 7 SEM images of SBN particles made at a reaction temperature of 300 °C with different Sr fractions x in the precursor: SBN20_T300, SBN30_T300, SBN40_T300, SBN50_T300 and SBN60_T300.

mechanism is proposed for SBN under hydrothermal conditions, schematically shown in Fig. 8. The precursor consists of clusters with corner- and edge-sharing NbO_6 octahedra and alkaline earth ions in solution. With increasing temperature, gradual reorientation of the octahedra occurs, before abrupt crystallization. With increasing degree of corner-sharing octahedra, the Nb–O network becomes increasingly negatively charged (fewer shared oxygen), thus increasing the driving force for the alkaline earth ions to enter the clusters/structure by the need for charge compensation. Sr^{2+} and Ba^{2+} ions are thus proposed to enter the clusters during the reorientation of the octahedra. A similar formation scheme has also been proposed for $K_xNa_{1-x}NbO_3$ (KNN) under hydrothermal conditions, but then with a crystalline intermediate with edge-sharing NbO_6 octahedra transforming into the corner-sharing perovskite structure of KNN.[44] The proposed formation mechanism for SBN has not been verified by X-ray total scattering and PDF analysis as in the case of WO_3.

After the nucleation of SBN, the growth rate is fast. The final shape of the particles is cubes with dimensions of ~500 × 500 × 500 nm^3 at higher temperatures (SBN50_T300) and rods ~1.5 μm long with a ~500 × 500 nm^2 cross section at lower temperatures (SBN50_T175). Here, we propose that the lower nucleation rate at lower temperatures leads to the formation of relatively few crystallites, which, when combined with a longer reaction time, will give good conditions for growth into the most favourable morphology

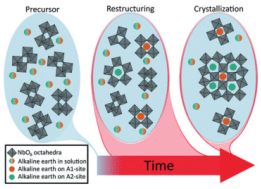

Fig. 8 Proposed reaction scheme for the nucleation of SBN. Initially the amorphous precursor consists of clusters with a mix of edge- and corner-sharing NbO_6 octahedra. With heat, the clusters undergo continuous and gradual restructuring leading to more corner-sharing octahedra, before abrupt crystallization occurs. Alkaline earth ions are believed to enter the clusters/structure continuously during this process.

for SBN. Hydrothermally synthesized SBN has been reported to form rods,[30] and from the solid-state synthesis of SBN, abnormal grain growth is known, leading to large anisometric grains.[25] In addition, the anisometric unit cell is likely to promote 1D growth, which for example is the case of the tungsten oxide $K_{0.4}WO_3$ forming long whiskers under hydrothermal synthesis[45] and the proposed Wulff construction of WO_3 having the shape of hexagonal rods.[46] The rod-shaped particles at lower temperatures are therefore assumed to be the preferred shape, or the Wulff construction, of SBN, grown by monomer/cluster addition in its preferred direction (*c*-direction). With increasing temperature, the nucleation rate increases, leading to faster depletion of the precursor and a shorter reaction time. This hinders SBN from reaching its preferred shape of rods, giving cubes with a similar cross section to the rods. For even higher temperatures, a small decrease in the size of the SBN cubes is observed, which is also linked to the higher nucleation rate and faster depletion of the precursor, and thus less growth. This is further supported by the reported *n* values, showing a nucleation- and growth-controlled mechanism. A more thorough parameter study on what governs the formation of rods, cubes and tubes is in progress.

The different sizes, morphologies and secondary phases formed throughout the experiments presented here are likely to explain why the Arrhenius plots do not show straight lines, and no activation energies can be obtained. The JMA model assumes among other things growth of spherical particles, which is not the case in the current work.

Sr fraction and microstructure from the Rietveld refinement

The Sr fraction in SBN increases close to linearly with the Sr fraction in the precursor in the range from 0.2 to 0.5, with a drop in the Sr fraction from 0.5 to 0.6. The linear increase is expected, and the drop between 0.5 and 0.6 is explained with the increasing amount of the Sr-rich Pyro phase at higher Sr fractions. The linear increase is not 1 : 1, which can be an effect of the different solubilities of $Ba(NO_3)_2$ and $Sr(NO_3)_2$,[47] where $Sr(NO_3)_2$ is more soluble in water and therefore to a larger degree remains in solution. It can also be an artefact of the model used for the Rietveld refinements, where we showed with reference to the solid-state synthesis samples that the Sr fraction is underestimated, especially at higher Sr fractions.

The experiment SBN50_supercrit gave a higher Sr fraction of 0.6 from the Rietveld refinement compared to the other experiments (around 0.35 ± 0.1). As water becomes supercritical, the dielectric constant drops significantly and changes the solvent properties.[5] Both $Ba(NO_3)_2$ and $Sr(NO_3)_2$ are only slightly soluble in ethanol at RT,[47] which has a comparable dielectric constant to water at 400 °C and 250 bar (supercritical conditions). Thus, the solubility of both $Ba(NO_3)_2$ and $Sr(NO_3)_2$ will be close to zero for SBN50_supercrit. The smaller Sr^{2+} can more easily enter the SBN structure, explaining why the increased Sr fraction is observed under supercritical conditions. To fully control the Sr fraction without introducing secondary phases, changing the dielectric constant of the solvent, either by going supercritical or by having a mixed solvent, looks promising based on the present work.

In the literature, it is reported that both the *a* and *c* parameters decrease with increasing Sr fraction at RT.[20] The *c* parameter in this work thus follows the expected trend with respect to both the Sr fraction in the precursor and the Sr fraction from the refinement, while *a* shows the opposite trend. No good explanations are found for this discrepancy other than the possibility of incorporation of hydroxyl groups in the structure. Hydroxyl groups have been shown to lie perpendicular to the *c*-axis in the SBN structure,[48,49] thus influencing the *a* parameter more than the *c* parameter.

Disorder and/or non-stoichiometry

B_{iso} values equal to 0 (negative if not constrained in the refinement) for the A1 site indicate a very low electron density on this site. Similarly, the Sr occupancy on the A1 site strictly following the upper limit for low Sr fractions also seems to indicate that the Rietveld refinement algorithm tries to maximize the electron density on the A1 site by increasing the Sr occupancy on the A1-site. The very low electron density on the A1 site might show that the real system contains some degree of disorder, for example, Ba on the A1 site, which is not accounted for by the model used, or that the total amount of Sr and Ba is actually higher than 5. To check this hypothesis, the last frame of SBN30_T300 was refined with varying total amounts of Sr and Ba; see the ESI† for a full description. These results point towards better overall fits and more physically sound values when increasing the total amount of Sr and Ba. A similar investigation was conducted for the effect of disorder by placing some Ba on the A1-site. With increasing amount of Ba on the A1-site, the overall fits became better, and more physically sound values were obtained. These results do not provide enough evidence with respect to disorder *vs.* non-stoichiometry but highlight the complexity of SBN and that our Rietveld refinement model

does not capture all features of SBN synthesized under the hydrothermal conditions used in this work.

Conclusion

A hydrothermal synthesis route for SBN was developed, enabled by a thorough *in situ* X-ray diffraction investigation. A formation mechanism for SBN is proposed, where the precursor consists of clusters of corner- and edge-sharing octahedra that gradually restructure into more corner-sharing clusters, before abrupt crystallization. We have, for the first time, tuned the Sr fraction in SBN (from 0.25 to 0.6) by hydrothermal synthesis, both by changing the Sr fraction x in the precursor, and by changing the dielectric constant of the solvent. Tuning the Sr fraction under synthesis has great potential since the Sr content is important for tailoring the properties of SBN. Furthermore, it is shown how the size and morphology of the SBN particles can be controlled by the reaction temperature and/or the Sr fraction in the precursor, with rod-, tube- and cube-shaped particles observed. Based on the morphologies observed, a possible growth mechanism is described.

Conflicts of interest

There are no conflicts to declare.

Acknowledgements

Solveig Stubmo Aamlid, MSc. is acknowledged for fruitful discussions on the Rietveld refinements of SBN. Financial support from NTNU Norwegian University of Science and Technology and The Research Council of Norway under the Toppforsk program to the project (No. 250403) "From aqueous solutions to oxide thin films and hierarchical structures" is gratefully acknowledged. The Research Council of Norway is acknowledged for the support to NTNU NanoLab through the Norwegian Micro and Nano-Fabrication Facility, NorFab, project number 245936/F50 and the Norwegian Center for Transmission Electron Microscopy, NORTEM (197405/F50). We are grateful to the Swiss-Norwegian Beamlines (SNBL) BM01 at the European Synchrotron Radiation Facility (ESRF, Grenoble, France) for granting access time to the CRG beamlines.

References

1 J. Varghese, R. W. Whatmore and J. D. Holmes, *J. Mater. Chem. C*, 2013, **1**, 2618–2638.
2 P. M. Rørvik, T. Grande and M.-A. Einarsrud, *Adv. Mater.*, 2011, **23**, 4007–4034.
3 L. Liang, X. Kang, Y. Sang and H. Liu, *Adv. Sci.*, 2016, **3**, 1500358.
4 M. E. Villafuerte-Castrejon, E. Moran, A. Reyes-Montero, R. Vivar-Ocampo, J. A. Pena-Jimenez, S. O. Rea-Lopez and L. Pardo, *Materials*, 2016, **9**, 27.
5 M.-A. Einarsrud and T. Grande, *Chem. Soc. Rev.*, 2014, **43**, 2187–2199.
6 P. B. Jamieson, S. C. Abrahams and J. L. Bernstein, *J. Chem. Phys.*, 1968, **48**, 5048–5057.
7 M. Ulex, R. Pankrath and K. Betzler, *J. Cryst. Growth*, 2004, **271**, 128–133.
8 X. Zhu, M. Fu, M. C. Stennett, P. M. Vilarinho, I. Levin, C. A. Randall, J. Gardner, F. D. Morrison and I. M. Reaney, *Chem. Mater.*, 2015, **27**, 3250–3261.
9 T. Lukasiewicz, M. A. Swirkowicz, J. Dec, W. Hofman and W. Szyrski, *J. Cryst. Growth*, 2008, **310**, 1464–1469.
10 J. Zhang, G. Wang, F. Gao, C. Mao, F. Cao and X. Dong, *Ceram. Int.*, 2013, **39**, 1971–1976.
11 A. M. Glass, *J. Appl. Phys.*, 1969, **40**, 4699–4713.
12 H. Tang, X.-G. Tang, M.-D. Li, Q.-X. Liu and Y.-P. Jiang, *J. Alloys Compd.*, 2019, **791**, 1038–1045.
13 M. D. Ewbank, R. R. Neurgaonkar, W. K. Cory and J. Feinberg, *J. Appl. Phys.*, 1987, **62**, 374–380.
14 S. Lee, R. H. T. Wilke, S. Trolier-McKinstry, S. Zhang and C. A. Randall, *Appl. Phys. Lett.*, 2010, **96**, 031910.
15 T. Kolodiazhnyi, H. Sakurai, M. Isobe, Y. Matsushita, S. Forbes, Y. Mozharivskyj, T. J. S. Munsie, G. M. Luke, M. Gurak and D. R. Clarke, *Phys. Rev. B: Condens. Matter Mater. Phys.*, 2015, **92**, 214508.
16 M. Paściak, P. Ondrejkovic, J. Kulda, P. Vaněk, J. Drahokoupil, G. Steciuk, L. Palatinus, T. R. Welberry, H. E. Fischer, J. Hlinka and E. Buixaderas, *Phys. Rev. B*, 2019, **99**, 104102.
17 P. Y. Vanina, S. B. Vakhrushev, A. A. Naberezhnov and A. A. Bosak, *J. Phys.: Condens. Matter*, 2019, **31**, 175401.
18 C. Heremans, B. J. Wuensch, J. K. Stalick and E. Prince, *J. Solid State Chem.*, 1995, **117**, 108–121.
19 J. G. Carrio, Y. P. Mascarenhas, W. Yelon, I. A. Santos, D. Garcia and J. A. Eiras, *Mater. Res.*, 2002, **5**, 57–62.
20 S. Podlozhenov, H. A. Graetsch, J. Schneider, M. Ulex, M. Wohlecke and K. Betzler, *Acta Crystallogr., Sect. B: Struct. Sci.*, 2006, **62**, 960–965.
21 G. H. Olsen, S. M. Selbach and T. Grande, *Phys. Chem. Chem. Phys.*, 2015, **17**, 30343–30351.
22 G. H. Olsen, U. Aschauer, N. A. Spaldin, S. M. Selbach and T. Grande, *Phys. Rev. B*, 2016, **93**, 180101.
23 S. S. Aamlid, S. M. Selbach and T. Grande, *Materials*, 2019, **12**, 1156.
24 K. Momma and F. Izumi, *J. Appl. Crystallogr.*, 2011, **44**, 1272–1276.
25 A. R. Kulkarni and P. K. Patro, *Trans. Indian Ceram. Soc.*, 2010, **69**, 135–146.
26 J. Schefer, D. Schaniel, V. Petříček, T. Woike, A. Cousson and M. Wöhlecke, *Z. Kristallogr. - Cryst. Mater.*, 2008, **223**, 399.
27 P. K. Patro, A. R. Kulkarni and C. S. Harendranath, *Mater. Res. Bull.*, 2003, **38**, 249–259.
28 C. Duran, G. L. Messing and S. Trolier-McKinstry, *Mater. Res. Bull.*, 2004, **39**, 1679–1689.
29 G.-H. Chen, J.-T. Liu, H.-R. Xu, C.-R. Zhou, M.-H. Jiang and X.-Y. Liu, *J. Mater. Sci.: Mater. Electron.*, 2011, **22**, 915–919.
30 A. Xia, Q. Ding, H.-Y. Miao and G.-Q. Tan, *Electrodeposition Compos. Mater.*, 2007, **26**, 37.

31 V. Dyadkin, P. Pattison, V. Dmitriev and D. Chernyshov, *J. Synchrotron Radiat.*, 2016, **23**, 825–829.

32 J. Becker, M. Bremholm, C. Tyrsted, B. Pauw, K. M. O. Jensen, J. Eltzholt, M. Christensen and B. B. Iversen, *J. Appl. Crystallogr.*, 2010, **43**, 729–736.

33 S. L. Skjærvø, K. H. Wells, S. Sommer, T.-D. Vu, J. R. Tolchard, W. van Beek, T. Grande, B. B. Iversen and M.-A. Einarsrud, *Cryst. Growth Des.*, 2018, **18**, 770–774.

34 A. R. M. Dalod, O. G. Grendal, S. L. Skjærvø, K. Inzani, S. M. Selbach, L. Henriksen, W. van Beek, T. Grande and M.-A. Einarsrud, *J. Phys. Chem. C*, 2017, **121**, 11897–11906.

35 J. S. O. Evans, *Mater. Sci. Forum*, 2010, **650**, 1–9.

36 P. Thompson, D. E. Cox and J. B. Hastings, *J. Appl. Crystallogr.*, 1987, **20**, 79–83.

37 G. Pawley, *J. Appl. Crystallogr.*, 1981, **14**, 357–361.

38 M. Avrami, *J. Chem. Phys.*, 1939, **7**, 1103–1112.

39 P. Nørby, M. Roelsgaard, M. Søndergaard and B. B. Iversen, *Cryst. Growth Des.*, 2016, **16**, 834–841.

40 H. L. Andersen, K. M. Ø. Jensen, C. Tyrsted, E. D. Bøjesen and M. Christensen, *Cryst. Growth Des.*, 2014, **14**, 1307–1313.

41 J. R. Eltzholtz, C. Tyrsted, K. M. O. Jensen, M. Bremholm, M. Christensen, J. Becker-Christensen and B. B. Iversen, *Nanoscale*, 2013, **5**, 2372–2378.

42 K. M. Peterson, P. J. Heaney and J. E. Post, *Chem. Geol.*, 2016, **444**, 27–36.

43 D. Saha, K. M. Ø. Jensen, C. Tyrsted, E. D. Bøjesen, A. H. Mamakhel, A.-C. Dippel, M. Christensen and B. B. Iversen, *Angew. Chem., Int. Ed.*, 2014, **53**, 3667–3670.

44 S. L. Skjærvø, K. H. Wells, W. van Beek, T. Grande and M.-A. Einarsrud, *CrystEngComm*, 2018, **20**, 6795–6802.

45 X.-G. Yang, C. Li, M.-S. Mo, J.-H. Zhan, W.-C. Yu, Y. Yan and Y.-T. Qian, *J. Cryst. Growth*, 2003, **249**, 594–599.

46 T. Lee, Y. Lee, W. Jang and A. Soon, *J. Mater. Chem. A*, 2016, **4**, 11498–11506.

47 *CRC Handbook of Chemistry and Physics*, ed. J. R. Rumble, CRC Press/Taylor & Francis, Boca Raton, Florida, USA, 99th edn (Internet Version), 2018.

48 S. Hunsche, A. Gröne, G. Greten, S. Kapphan, R. Pankrath and J. Seglins, *Phys. Status Solidi A*, 1995, **148**, 629–634.

49 M. Lee, H. S. Lee and R. S. Feigelson, *J. Appl. Phys.*, 1998, **84**, 1558–1560.

Controlled growth of $Sr_xBa_{1-x}Nb_2O_6$ hopper- and cube-shaped nanostructures by hydrothermal synthesis

Ola Gjønnes Grendal

Abstract

Controlling the shape and size of nanostructured materials have been a topic of interest in the field of material science for decades. In this work, the ferroelectric material $Sr_xBa_{1-x}Nb_2O_6$ (x = 0.32–0.82, SBN) was prepared by hydrothermal synthesis, and the morphology is controllably changed from cube-shaped to hollow-ended structures based on a fundamental understanding of the precursor chemistry. Synchrotron X-ray total scattering and PDF analysis were used to reveal the structure of the Nb-acid precursor, showing Lindquist-like motifs. The changing growth mechanism, from layer-by-layer growth forming cubes to hopper-growth yielding hollow-ended structures, is attributed to differences in supersaturation. Transmission electron microscopy revealed an inhomogeneous composition along the length of the hollow-ended particles, which is explained by preferential formation of the high entropy composition, SBN33, at the initial stages of particle nucleation and growth.

Appendix A

Temperature calibration and heating profiles for the *in situ* setup

Temperature calibrations of the *in situ* setup was conducted at each beam time by placing a K-type thermocouple inside the capillary. The capillary was filled with water and pressurized to 100 bar during the calibrations. A tight seal around the inserted thermocouple was obtained by graphite ferrules and Swagelok fittings. A straight Swagelok connection was used for easy insertion of the thermocouple. The thermocouple was used to correlate the temperature inside the capillary with the set-point temperature on the PID controller used to control the temperature of the heat blower. The heat blower was heated to the desired set-point temperature aimed away from the capillary and moved into position with a step motor. The temperature calibration was done in steps of 50 °C, and full heating profiles were measured as shown in Figure A.1. The set-point temperature is reached ~20 s after the onset of the heating. The capillary was cooled to room temperature between each measurement.

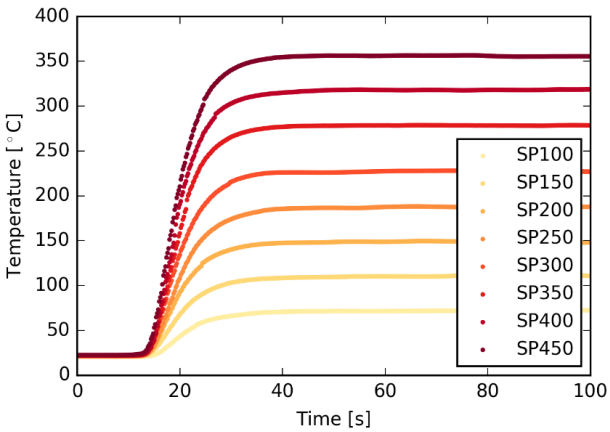

Figure A.1: Heating profiles for the *in situ* setup measured with a thermocouple inside a water filled and pressurized single crystal sapphire capillary.

Appendix B

Effect of capillary material on the *in situ* experiments of $Sr_xBa_{1-x}Nb_2O_6$

After the failed attempt to collect *in situ* X-ray total scattering for PDF analysis during the hydrothermal synthesis of $Sr_xBa_{1-x}Nb_2O_6$ (SBN), a couple of control experiments were conducted. To investigate the effect of capillary material (single crystal sapphire and fused silica) on the synthesis of SBN, the *in situ* setup was assembled in a fume hood in our home lab. Two experiments were performed, one using a sapphire capillary, and one using a fused silica capillary. Both reactions were run for 1 h at 300 °C. The same precursor slurry, prepared as described in section 3.2.1, with a Sr fraction of 0.4 was used for both experiments. After the experiments, the capillaries were broken in two halves, right in the middle, and the product only from the heat affected area of the capillary was collected. The collected slurries were characterized with XRD (as described in section 3.2.2) without further treatment. XRD presented in Figure B.1 shows the clear effect of the capillary material, where the reaction in fused silica gave only an amorphous product, while in the sapphire capillary crystalline SBN was formed. It is clear that the formation of SBN is suppressed in the fused silica capillary.

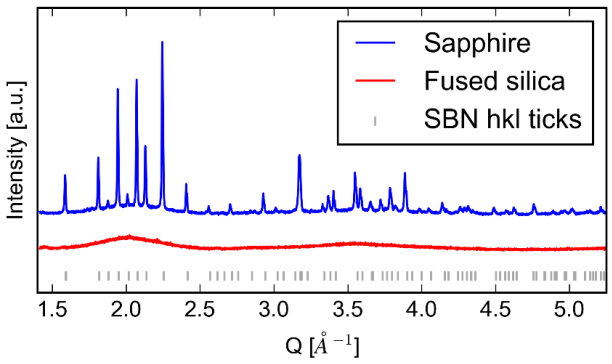

Figure B.1: XRD of experiments conducted with the *in situ* setup, showing crystalline SBN using a single crystal sapphire capillary (blue) and amorphous product using a fused silica capillary (red).

Appendix C

Supplementary information for the papers and manuscript

Supplementary information Paper 1:

Grendal, O.G., Blichfeld, A. B., Skjærvø, S. L., van Beek, W., Selbach, S. M., Grande, T., Einarsrud, M.-A., Facile low temperature hydrothermal synthesis of $BaTiO_3$ nanoparticles studied by *in situ* X-ray diffraction, *Crystals* **8**, 253-264 (2018).

Supplementary information Paper 2:

Grendal, O.G., Blichfeld, A. B., Vu, T. D., van Beek, W., Selbach, S. M., Grande, T., Einarsrud, M.-A., Composition and morphology tuning during hydrothermal synthesis of $Sr_xBa_{1-x}Nb_2O_6$ tetragonal tungsten bronzes studied by *in situ* X-ray diffraction, *CrystEngComm* **21**, 5922-5930 (2019).

Supplementary information Manuscript 1:

Grendal, O.G., Nylund, I.-E., Blichfeld, A. B., Tominaka, S., Ohara, K., Selbach, S. M., Grande, T., Einarsrud, M.-A., Designed growth of $Sr_xBa_{1-x}Nb_2O_6$ hopper- and cube-shaped nanostructures by hydrothermal synthesis, submitted to *Chemistry: A European Journal* (January 2020).

Supplementary Materials

Facile Low Temperature Hydrothermal Synthesis of $BaTiO_3$ Nanoparticles Studied by In Situ X-ray Diffraction

Ola G. Grendal [1], Anders B. Blichfeld [1], Susanne L. Skjærvø [1], Wouter van Beek [2], Sverre M. Selbach [1], Tor Grande [1] and Mari-Ann Einarsrud [1,*]

[1] Department of Materials Science and Engineering, NTNU Norwegian University of Science and Technology, 7491 Trondheim, Norway; ola.g.grendal@ntnu.no (O.G.G.); anders.b.blichfeld@ntnu.no (A.B.B.); susanne.l.skjarvo@ntnu.no (S.L.S.); selbach@ntnu.no (S.M.S.); grande@ntnu.no (T.G.)

[2] Swiss-Norwegian Beamlines at European Synchrotron Research Facility, 38043 Grenoble, France; wouter@esrf.fr (W.B.)

* Correspondence: mari-ann.einarsrud@ntnu.no; Tel.: +47-735-94-002

Selected temperature profiles

Temperature profiles during heating of the capillary were measured with a thermocouple placed inside the sapphire capillary, while the capillary was filled with water and pressurized to 100 bar. Temperature profiles were measured in 50 °C intervals from room temperature (RT) to 400 °C (referring to the set-point temperature of the heat blower). The measured values were then used to calibrate the set-point temperature of the heat blower with the actual temperature inside the capillary.

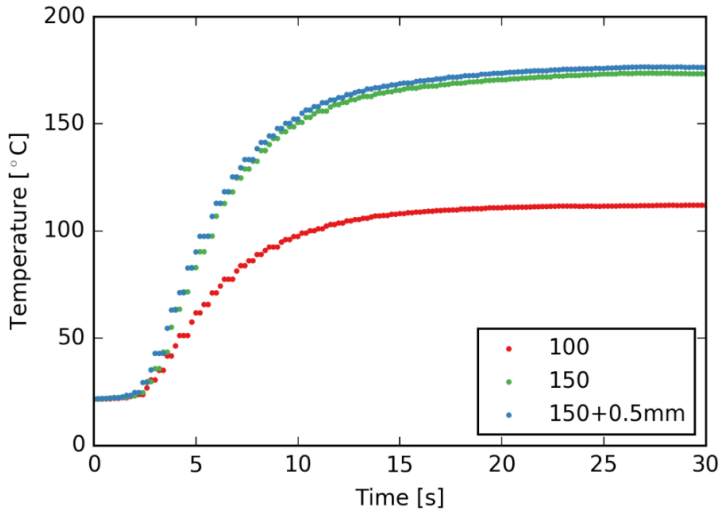

Figure S1: Heating profiles for two different set-point temperatures (red (100 °C) and green (150 °C)). Blue data corresponds to 150 °C, but with the capillary moved 0.5 mm closer to the heat blower compared to the green data showing the robustness of this setup.

Typical Rietveld refinements

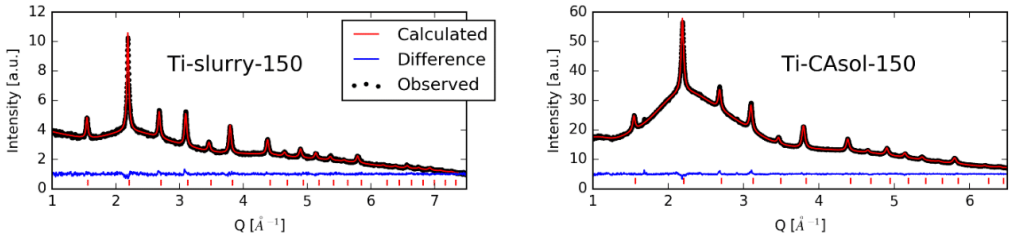

Figure S2: Last frames of experiments Ti-slurry-150 and Ti-CAsol-150 showing typical refinements, with red markers showing diffraction lines of $BaTiO_3$ at RT from ICDD card #01-074-4539. Refined values (R-values, lattice parameter, size, strain and atomic displacement parameters) are reported in Table S1.

SEM images of Ti-CAsol-125

The Ti-CAsol-125 sample was collected after the *in situ* experiment and washed with distilled water several times before SEM imaging. SEM images were recorded on an in-lens cold field emission Hitachi S-5500 S(T)EM. Secondary electrons at 7 kV were detected. The sample was prepared by letting a diluted dispersion of particles in distilled water dry on the aluminum sample holder (for approximately 12 h). No further sample preparation was done.

The nature of the *in situ* setup makes collection of the sample challenging, and it is close to impossible to be sure that the collected sample is free of unreacted precursor (it is not believed that the washing done here would remove the unreacted amorphous precursor, as it is not water soluble). The particle size is determined to be around 30 nm or less. Higher resolution images would be needed for more accurate determination of particle size, together with an improved *in situ* setup allowing for collection of the sample without any unreacted precursor.

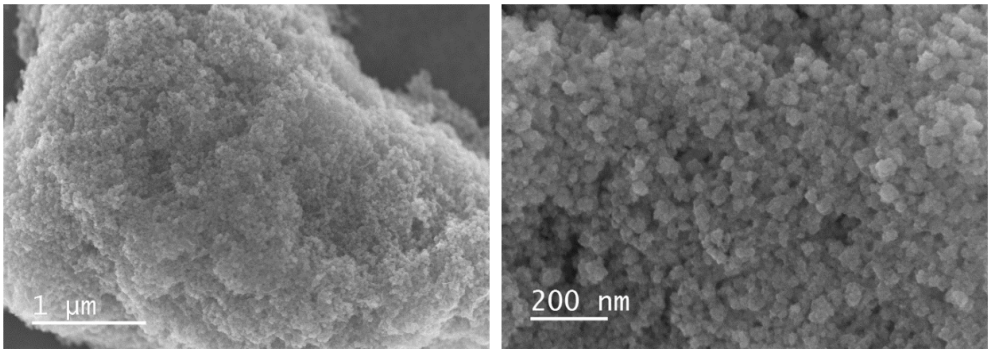

(a) (b)

Figure S3: SEM images of Ti-CAsol-125 at different magnifications, showing agglomerated spherical $BaTiO_3$ nanoparticles with a size of 30 nm or less (a) 30x magnification, (b) 100x magnification.

Time resolved atomic displacement parameters for Ti and Ba for all experiments

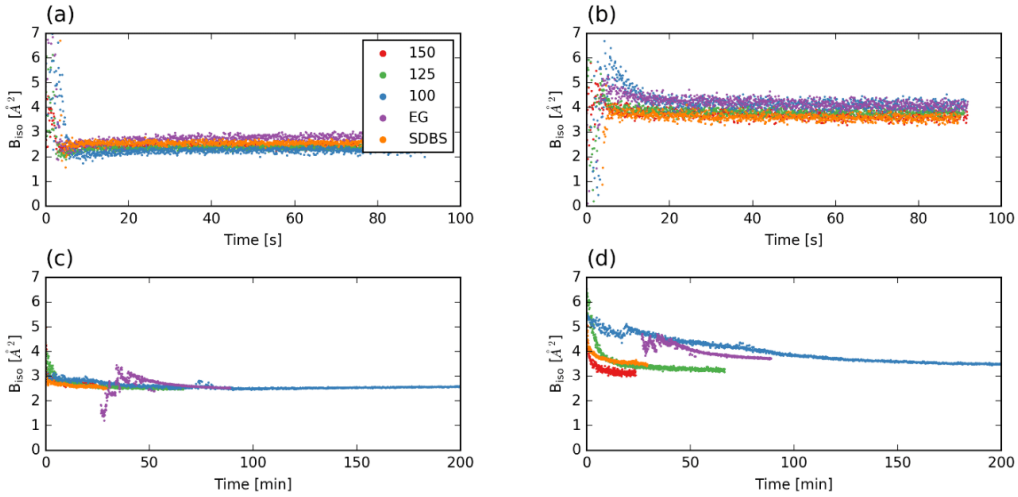

Figure S4: Refined atomic displacement parameters for (a-b) Ti-slurry, and (c-d) Ti-CAsol experiments. (a) refined B_{iso} values for Ba; (b) refined B_{iso} values for Ti; (c) refined B_{iso} values for Ba; (d) refined B_{iso} values for Ti. Color-coding is as described in (a) for all panels.

Fits of the Johnson-Mehl-Avrami equation to the normalized scale factors

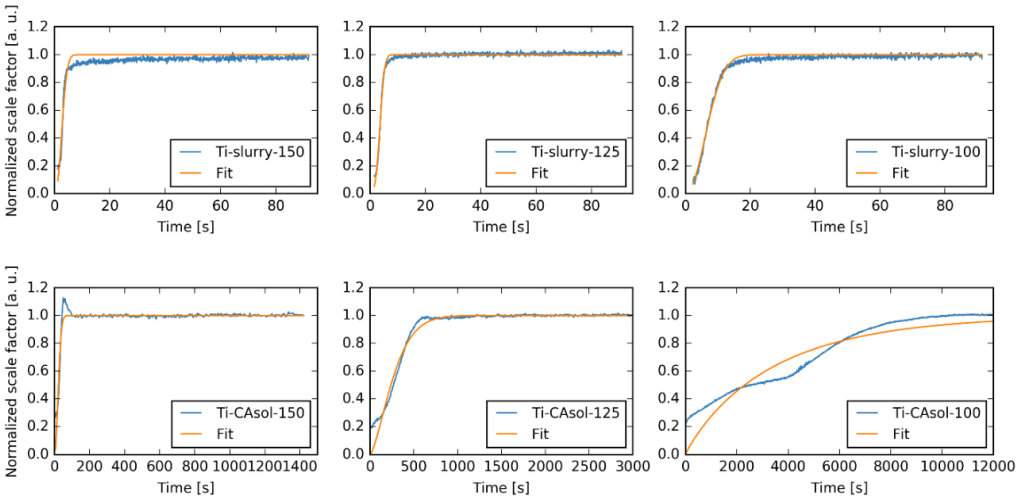

Figure S5: Normalized scale factor and fits with the Johnson-Mehl-Avrami equation for all samples used for the kinetic modeling.

Summary of the final refined values for all experiments

Isotropic Lorentzian strain and size parameter, lattice parameter, and B_{iso} for Ti and Ba for $BaTiO_3$ were refined. Scale factor was refined for $BaCO_3$ (for Ti-CAsol-100 and Ti-CAsol_EG) for the batch refinement, keeping size and lattice parameters fixed to the values refined in the last frame (the frame with most $BaCO_3$).

Table S1: Refined values (size, strain, lattice parameter, atomic displacement parameters for Ti and Ba and R-values, R_{bragg} is for $BaTiO_3$) for the last frame from each experiment. Refinements were done using space group no. 221, $Pm\bar{3}m$, for $BaTiO_3$.

Sample	Crystallite size [nm]	Strain [10^{-3}]	Lattice parameter [Å]	Ti B_{iso} [Å^2]	Ba B_{iso} [Å^2]	R_{wp} [a.u.]	R_{bragg} [a.u.]	Amount $BaCO_3$ [wt %]
Ti-slurry-100	14.3(4)	1.27(7)	4.0612(3)	3.99(9)	2.39(6)	2.14	0.99	0
Ti-slurry-125	15.0(4)	1.25(6)	4.0603(3)	3.78(8)	2.31(5)	1.89	1.02	0
Ti-slurry-150	15.6(2)	0.94(3)	4.0587(2)	3.73(5)	2.49(3)	1.01	0.96	0
Ti-slurry-EG	8.7(2)	0.76(8)	4.0632(4)	4.23(8)	2.82(6)	1.99	0.76	0
Ti-slurry-SDBS	25.0(7)	0.60(4)	4.0531(2)	3.67(7)	2.59(4)	1.99	1.27	0
Ti-CAsol-100	13.9(3)	0.86(5)	4.0540(2)	3.48(6)	2.56(4)	1.80	1.13	12
Ti-CAsol-125	12.6(1)	0.67(3)	4.0505(1)	3.29(4)	2.54(3)	1.20	0.97	0
Ti-CAsol-150	12.5(2)	0.63(5)	4.0507(2)	3.04(6)	2.72(4)	0.90	0.67	0
Ti-CAsol-EG	13.4(2)	0.84(4)	4.0504(2)	3.68(5)	2.53(3)	1.30	0.93	5
Ti-CAsol_SDBS	10.7(1)	0.76(4)	4.0530(2)	3.48(5)	2.51(3)	1.30	0.70	0

Electronic Supplementary Information

Stoichiometry and morphology tuning of $Sr_xBa_{1-x}Nb_2O_6$ tetragonal tungsten bronzes; an in situ hydrothermal synthesis X-ray diffraction study

Ola G. Grendal [1], Anders B. Blichfeld [1], Tuong D. Vu [1], Wouter van Beek, [2] Sverre M. Selbach [1], Tor Grande [1] and Mari-Ann Einarsrud [1,*]

[1] Department of Materials Science and Engineering, NTNU Norwegian University of Science and Technology, 7491 Trondheim, Norway.
[2] Swiss-Norwegian Beamlines at European Synchrotron Research Facility, 38043 Grenoble, France.
* Correspondence: mari-ann.einarsrud@ntnu.no; Tel.: +47-735-94-002

Selected temperature profiles

Temperature profiles during heating of the capillary were measured with a thermocouple placed inside the sapphire capillary, while the capillary was filled with water and pressurized to 100 bar. Temperature profiles were measured in 50 °C intervals 100 to 400 °C (referring to the set-point temperature of the heat blower). The measured values were then used to calibrate the set-point temperature of the heat blower with the actual temperature inside the capillary.

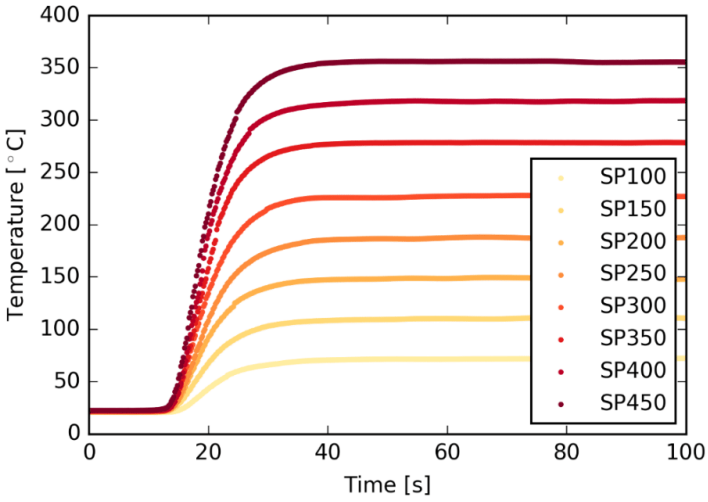

Figure S1: Heating profiles for various set-point temperatures (100 – 450 °C). For all set-point temperatures a steady state is reached after about 20 s.

Typical input file used for the batch Rietveld refinement in *TOPAS*

For the sequential refinements the following parameters where refined for SBN: scale factor, two lattice parameters (a and c in the tetragonal cell), Lorentzian and Gaussian strain parameter, isotropic atomic displacement parameter (APD, B_{iso}) for both the niobium and the alkaline earth sites (4 in total), Sr fraction, Sr occupancy on the A1-site and 3 atomic position parameters (in total 14 structural parameters). The 3 atomic position parameters were the x and y positions for the B2- and A1-site respectively (only one parameter is needed for the A1-site due to symmetry constraints). Sr was allowed to occupy the A1- and A2-sites, while Ba was locked to the A2-sites while keeping the stoichiometry (the sum of Ba and Sr equal to 5 plus 1 vacancy) and having physically meaningful occupancies (non-negative and not higher than 1). The background was fitted with a 35th order Chebyshev polynomial to account for the broad background peak of water and solutes for each frame. Zero-shift error was refined for the last frame for each experiment, and then kept fixed for the batch refinement. Atomic positions and B_{iso} values for all oxygen atoms were kept fixed to RT neutron data from Carrio et al. [1]. Because of the temperature being higher than, or close to the reported T_c for SBN for all experiments, the centrosymmetric space group (no. 127, *P4/mbm*) was used for all refinements instead of the reported non-centrosymmetric space group (no. 100, *P4bm*) stable at RT.

Below is a typical input-file for *TOPAS* used in this work, showing what equations and constraints are used for the different parameters. A "summarized" version of the input-file is presented in Table S1, and a typical graphical representation of a Rietveld refinement is presented in Figure S2.

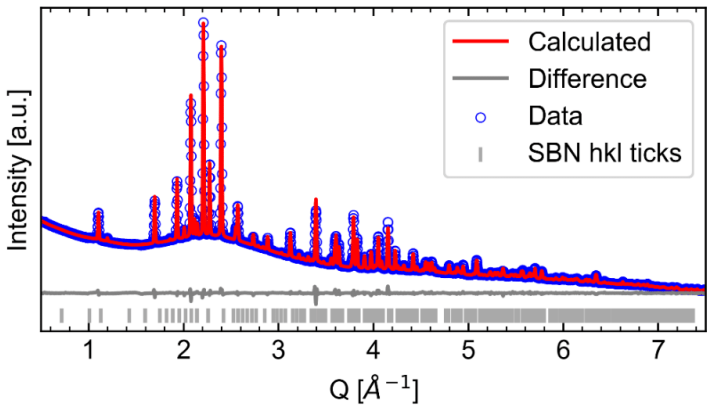

Figure S2: Representative graphical representation of a Rietveld refinement, presented with SBN50_T300 at the end of experiment.

```
r_exp  0.0255204487 r_exp_dash  0.127019401 r_wp  1.96483467 r_wp_dash  9.77929996 r_p  0.943879931
r_p_dash  9.91316111 weighted_Durbin_Watson  0.267602062 gof  76.9906006

iters 100000

xdd "IN_FILE.xye"

r_exp  0.0255204487 r_exp_dash  0.127019401 r_wp  1.96483467 r_wp_dash  9.77929996 r_p  0.943879931
r_p_dash  9.91316111 weighted_Durbin_Watson  0.267602062 gof  76.9906006

x_calculation_step 0.01

'35th order Chebychev
```

```
bkg @  22599.4817`_28.5226096 -20712.2473`_53.3728287  1593.86128`_51.3664193 -
233.598229`_49.7733623  251.054531`_48.0132791 -1755.78153`_46.9298452  2685.7828`_46.1299153 -
898.431397`_45.0653321 -683.825704`_44.2134599  1284.87657`_43.7297047 -409.724229`_43.2107424 -
555.518095`_42.4263143  589.952675`_42.0875049 -144.851875`_41.3547231 -225.389735`_40.8036582
317.795294`_40.4192511 -107.279117`_39.9558045  76.0631089`_39.3158164  142.786448`_39.0693042
12.5318361`_38.460597  18.3369476`_38.1103801  78.7237282`_37.559452  48.0405916`_37.1906964 -
3.35622708`_36.2257427 -17.0849808`_35.9528332  95.0641312`_35.110942 -24.0283942`_34.7009036
6.4279789`_33.1029892 -32.3078696`_32.356327  4.36366726`_30.2236073 -22.5049771`_29.6072912 -
14.1927031`_26.7415948  8.22815171`_25.0805855  21.8396967`_19.287633 -20.3509081`_15.112047

start_X  3

finish_X  51

no_LIMIT_warnings

do_errors

Zero_Error(!zero ,-0.00549`_0.00032)

lam ymin_on_ymax 0.001 la 1.0 lo 0.77445 lh 0.1

LP_Factor( 90) 'change the LP correction  or lh value if required

str

        e0_from_Strain( 0.00063`_0.00001, sgc, 0.23848`_0.00481, slc, 0.08791`_0.00518) 'defines and refines
the values e0, name for Strain_G, value, name for Strain_L, value

        prm !e0_SBN =Voigt_FWHM_GL(CeV_or_0(sgc, sgv), CeV_or_0(slc, slv)) .25 Pi/360; :  0.00063`_0.00001
'calculates the e0 using a macro in topas.inc

        r_bragg r_b_SBN  1.11129852

        phase_MAC  22.296247`_0.0920996971

        phase_name "SBN"

        MVW( 1995.992`_2.409, 626.224`_0.024, 100.000`_0.000)

        scale scale_SBN  0.000309860911`_1.918e-006

        space_group P4/mbm

        Phase_LAC_1_on_cm( 118.00760`_0.62990)

        Phase_Density_g_on_cm3( 5.29271`_0.00639)

        Tetragonal(a_SBN  12.564880`_0.000213 min=12.45; max=12.60;, c_SBN  3.966552`_0.000076
min=3.955; max=3.98;)

        site Nb1 num_posns  2 occ Nb  1 beq b_Nb1  3.12544`_0.08979 min 0 max 7 x  0 y  0.5 z 0

        site Nb2 num_posns  8 occ Nb  1 beq b_Nb2  2.21513`_0.04540 min 0 max 7 x = 0.07529+xNb2; y =
0.21097+yNb2; z 0

        site A1 num_posns  2 x  0  y  0 z 0.5

                occ Sr  SrA1  0.92471`_0.01099 min = 1/2; max = Sr/2; beq b_A1  2.30362`_0.15923 min 0
max 7

        site A2 num_posns  4       x xA2 = 0.17097+disp;      y yA2 = 0.67097+disp;      z  0.5

                occ Sr  SrA2 =     (Sr-2*SrA1)/4; :  0.03903`_0.01330 beq b_A2  4.38415`_0.10159 min 0 max 7

                occ Ba  BaA2 =     Ba/4; :  0.74862`_0.01212 beq b_Ba2 = b_A2;

        site O1   num_posns  8 occ O   1 beq   1.90   x  0.3413          y  0.0055          z  0.0

        site O2   num_posns  8 occ O   1 beq   1.93   x  0.1413          y  0.0647          z  0.0

        site O3   num_posns  4 occ O   1 beq   0.13   x  0.2817          y  0.7817          z  0.0

        site O4   num_posns  2 occ O   1 beq   3.85   x  0               y  0.5             z  0.5
```

```
        site O5   num_posns  8 occ O   1 beq   2.88   x  0.2965          y  0.4175          z  0.5
        prm Sr  2.00554`_0.04846 min 1 max  4
        prm Ba = 5-Sr; :  2.99446`_0.04846
        prm disp  0.00229`_0.00017 min -0.01 max  0.01
        prm xNb2 -0.00090`_0.00014 min -0.01 max  0.01 'Dispplacment in x-direction for Nb2-site
        prm yNb2  0.00254`_0.00015 min -0.01 max  0.01 'Displcament in y-direction for Nb2-siter
        prm !sumA1 = SrA1; :  0.92471`_0.01099 'Total occupancy on A1 site
        prm !sumA2 = BaA2+SrA2; :  0.78765`_0.00549 'Total occupancy on A2 site
        prm !vac_A1 = (1-sumA1)*2; :  0.15059`_0.02197 'Fraction vacancy on A1
        prm !vac_A2 = (1-sumA2)*4; :  0.84941`_0.02197 'Fraction vacancy on A2
        prm !sum_vac = vac_A1+vac_A2; :  1.00000`_0.00000 'Total vacancy
        prm !sum_Ba = 4*BaA2; :  2.99446`_0.04846 'Total Ba
        prm !sum_Sr = 2*SrA1+4*SrA2; :  2.00554`_0.04846 'Total Sr
        prm !ratio_Sr = sum_Sr/(sum_Sr+sum_Ba); :  0.40111`_0.00969 'Amount of Sr in formula SrxBa1-xNb2O6
   TCHZ_Peak_Type(, -0.45497, ,-0.01050, , -0.45190, , 0.45791, , 0.00012, , 0.00182)
Out_X_Yobs_Ycalc_Difference("IN_FILE.txt")
        out "SBN_50_T300_P200.txt" append
        Out(Get (r_wp), "%.5e")
        Out(Get (r_exp), "%15.5e")
        Out(Get (gof), "%15.5e")
        Out(r_b_SBN, "%15.5e")
        Out(scale_SBN, "%15.5e", "%15.5e")
        Out(a_SBN, "%15.5e", "%15.5e")
        Out(c_SBN, "%15.5e", "%15.5e")
        Out(e0_SBN, "%15.5e", "%15.5e")
        Out(b_Nb1, "%15.5e", "%15.5e")
        Out(b_Nb2, "%15.5e", "%15.5e")
        Out(xNb2, "%15.5e", "%15.5e")
        Out(yNb2, "%15.5e", "%15.5e")
        Out(b_A1, "%15.5e", "%15.5e")
        Out(b_A2, "%15.5e", "%15.5e")
        Out(disp, "%15.5e", "%15.5e")
        Out(vac_A1, "%15.5e", "%15.5e")
        Out(sumA1, "%15.5e", "%15.5e")
        Out(sumA2, "%15.5e", "%15.5e")
        Out(ratio_Sr, "%15.5e", "%15.5e")
        Out(scale_pyro, "%15.5e")
        Out(zero, "%15.5e\n")
```

Table S1. Overview of refined parameters from the Rietveld batch refinements and as preparation for the batch refinements respectively. Also included is a comment on what constraints or restrictions have been used for the different refinements.

Parameter	Prep refinement	Batch refinement	Comment
Zero error	Refined	Fixed	Fixed to value at end of experiment
Scale factor	Refined	Refined	
a [Å]	Refined	Refined	
c [Å]	Refined	Refined	
Gaussian and Lorentzian strain	Refined	Refined	
Sr fraction [a.u.]	Refined	Refined	
Sr occupancy A1 [a.u.]	Refined	Refined	
Sr occupancy A2 [a.u.]	Calculated	Calculated	Assuming unfilled TTB
Ba fraction [a.u.]	Calculated		Assuming Ba = 1 - Sr
Ba occupancy A1	Locked to 0		
Ba occupancy A2	Calculated		Assuming unfilled TTB
Nb2 atomic positions (x and y)	Refined	Refined	2 parameters
A1 atomic positions (x and y)	Refined	Refined	1 parameter (symmetry constraint)
O positions	Fixed	Fixed	Fixed to neutron data
O thermal parameters	Fixed	Fixed	Fixed to neutron data
Total parameters refined	15	14	

Validation of the Rietveld refinement model

$Sr_xBa_{1-x}Nb_2O_6$ (SBN100*x) was prepared by Aamlid et al. [2] by solid-state synthesis at 1400 °C with four different nominal compositions (SBN25_T800, SBN33_T800, SBN50_T800 and SBN61_T800) and synchrotron X-ray powder diffraction data was collected at SNBL, ESRF (λ = 0.77624 Å). Details of synthesis and X-ray diffraction measurements conditions are found in [2]. The Rietveld refinement model described in the main text was used on this data set to verify that especially the refined Sr fraction values can be trusted. Figure S3 shows the Rietveld refinements, and in Figure S4 the refined lattice parameters (a and c) are plotted as a function of refined Sr fraction (diamonds) and nominal Sr fraction (upside down triangle) and compared to literature values. The results show that the refined Sr fraction definitely can be trusted (refined lattice parameters as a function of refined Sr fraction fits well with literature). It is also observed that the refined Sr fractions are seemingly underestimating the nominal Sr fraction (this is assumed to be the real Sr fraction, since the samples are made by solid-state synthesis), as is seen by the better fit of the lattice parameters with literature when plotted versus the nominal Sr fraction.

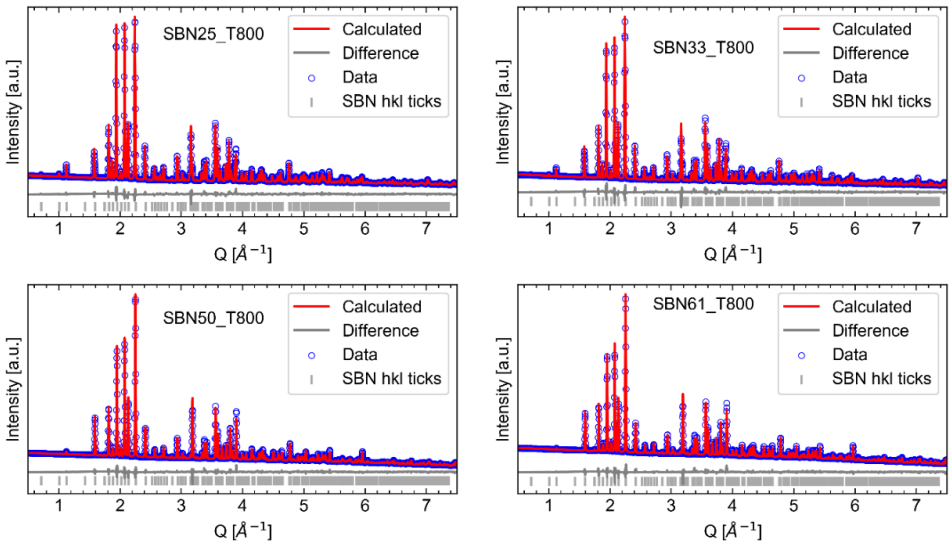

Figure S3: Rietveld refinement of SBN25_T800, SBN33_T800, SBN50_T800 and SBN61_T800 showing data (blue circles), calculated (red) and the difference between data and calculated (grey). Grey bars show theoretical hkl positions of the SBN diffraction lines.

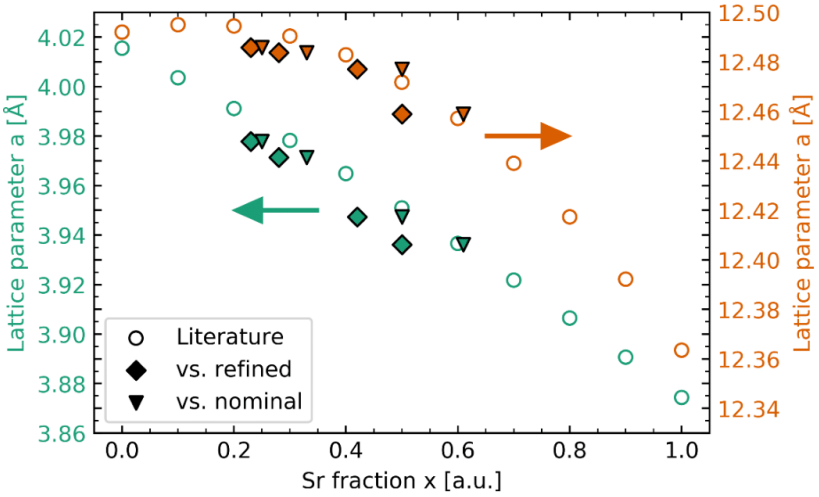

Figure S4: Refined lattice parameters for SBN (a and c) plotted versus refined Sr fraction (diamonds) and nominal Sr fraction (triangles). Indicated with open symbols are literature values for the a and c parameters at room temperature obtained from Podlozhenov et al. [3].

TEM study of observed rods and bipyramids from hydrothermal synthesis of SBN

A hydrothermal reaction was done in a conventional steel autoclave with a PTFE liner with a filling factor of 70 %. The reaction was performed at 250 °C for 48 h and a Sr fraction of 0.5 in the precursor. The X-ray diffraction pattern showed SBN as the main phase with traces of the Pyro phase. By scanning electron microscopy (SEM) a mixture of rods and bipyramids were observed. It was assumed that SBN had formed rods, while the Pyro phase formed bipyramids. To verify this transmission electron microscopy (TEM) with a combination of imaging, electron diffraction and energy-dispersive X-ray spectroscopy (EDX) were used.

A JEOL JEM-2100 TEM equipped with an Oxford X-max80 EDX-detector was used, with an acceleration voltage of 200 kV. The sample was prepared by dropping a diluted acetone-dispersion of the sample on a carbon coated copper TEM grid and let dry it dry for approximately 10 min.

The results show that the rods are in fact SBN, and that the bipyramids are Pyro. Also, it shows that the Pyro phase is Sr rich compared with the SBN rods.

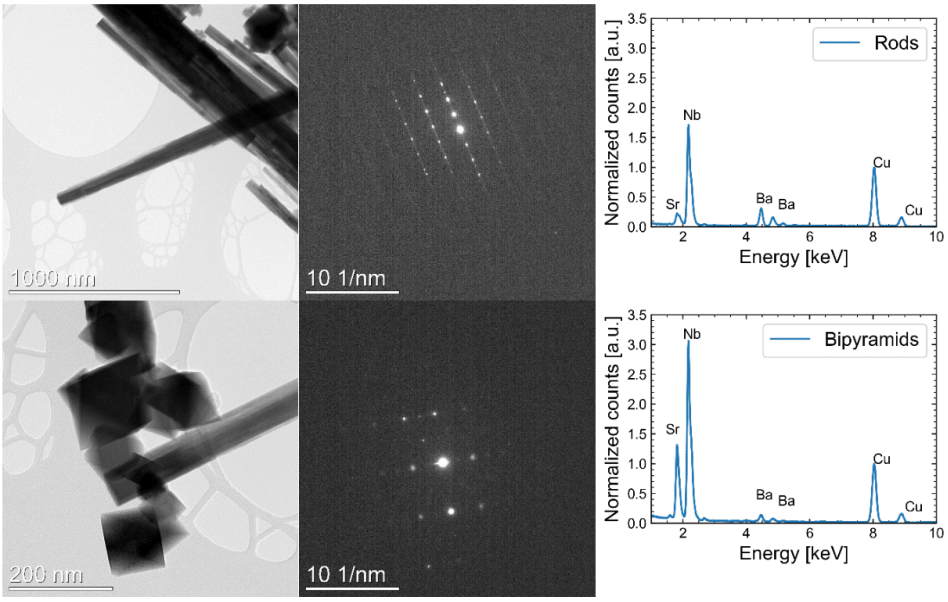

Figure S6: TEM images, electron diffraction and EDX for the observed rods (top row) and bipyramids (bottom row). EDX data are normalized to the most intense Cu-peak which is coming from the sample holder and is thus assumed to be comparable for the two EDX patterns.

Morphology development as a function of temperature and Sr fraction

Decreasing reaction time gives in general an increase in aspect ratio. At lower temperatures more compositions show signs of hollow cubes or rods, while SBN have tube shaped particles for all temperatures.

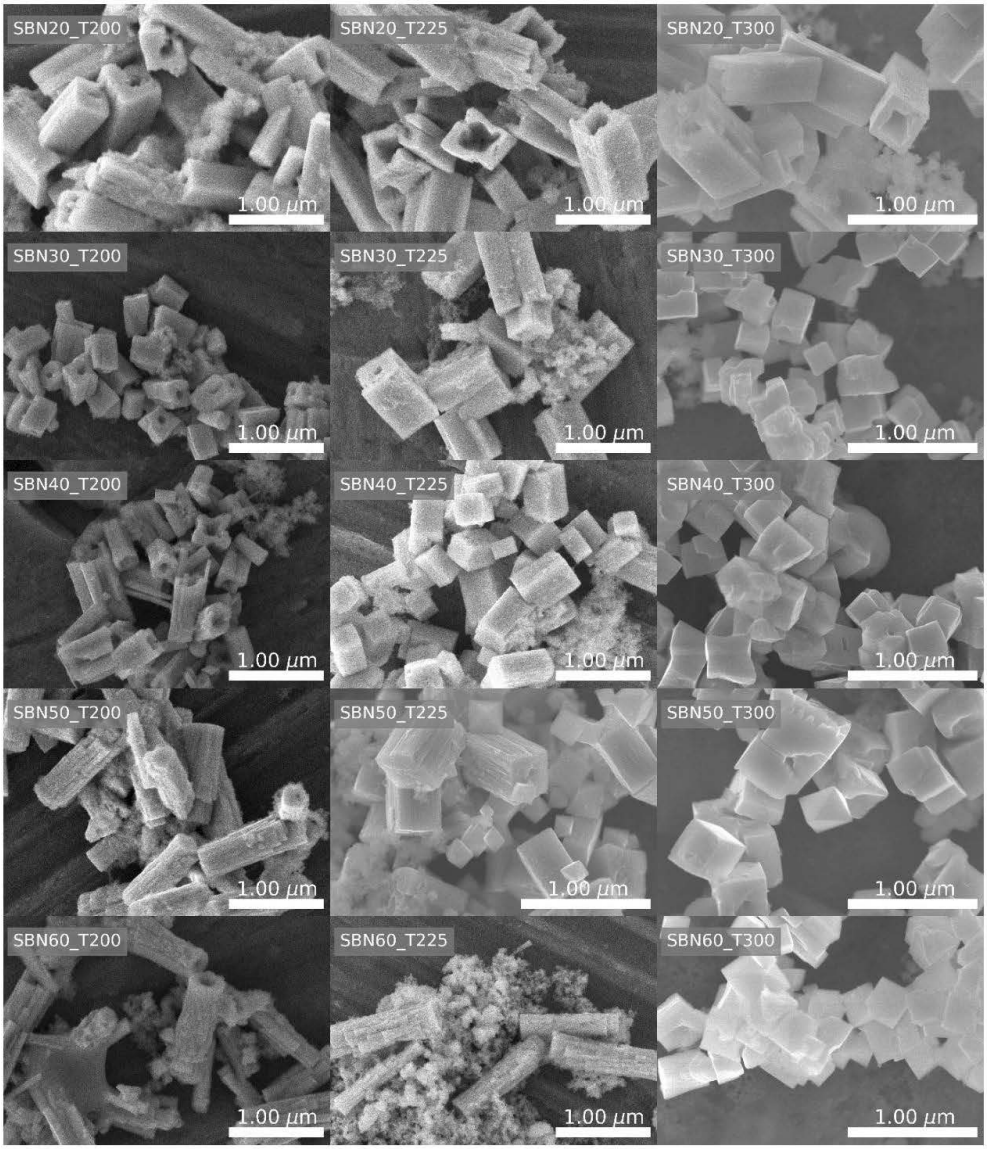

Figure S7: SEM images of all compositions (SBN20-60) with reaction temperatures of 200, 225 and 300 °C.

Summary of the final refined values for all experiments

Scale factor, isotropic Lorentzian and Guassian strain, lattice parameter, Sr fraction, Sr occupancy on A1-site, B_{iso} for the Nb1-, Nb2-, A1- and A2-site, and two atomic position parameters for the Nb2-site (x and y) and one for the A1-site for SBN were refined. Scale factor was refined for Pyro (with Pawley fit) and Uknw (with single peak phases) when present for the batch refinement, keeping lattice parameters (Pyro) and peak positions (Uknw) fixed to the values refined in the last frame.

Table S2: Refined values (strain, lattice parameter a and c, Sr fraction, Sr occupancy on A1-site, atomic displacement parameters for Nb1, Nb2, A1 and A2, atomic position parameters, R_{wp} and R_{bragg}) for the last frame from each experiment. Estimated standard deviations from *TOPAS* are given, where for example 1.5(1) equals 1.5 ± 0.1.

Sample	Strain [10^{-3}]	Lattice parameter a [Å]	Lattice parameter c [Å]	Sr fraction x [a.u.]	Sr occ A1 [a.u.]	Biso Nb1 [Å²]	Biso Nb2 [Å²]	x Nb2-site
SBN60_T300	0.76(2)	12.5672(2)	3.9651(1)	0.30(1)	0.75(1)	2.9(1)	2.0(1)	0.0751(2)
SBN60_T225	0.70(4)	12.5664(2)	3.9659(1)	0.38(2)	0.91(2)	3.3(2)	2.0(1)	0.0746(3)
SBN60_T200	0.75(5)	12.5537(3)	3.9633(2)	0.37(2)	0.92(3)	2.9(2)	2.3(1)	0.0744(4)
SBN50_T400	0.77(2)	12.5607(1)	3.9647(1)	0.34(1)	0.85(1)	2.4(1)	1.9(1)	0.0740(2)
SBN50_T300	0.66(1)	12.5635(1)	3.9659(1)	0.32(1)	0.81(1)	3.0(1)	2.13(5)	0.0746(2)
SBN50_T225	0.71(2)	12.5692(2)	3.9621(1)	0.33(1)	0.82(1)	3.4(1)	1.9(1)	0.0747(2)
SBN50_T200	0.71(2)	12.5644(2)	3.9710(1)	0.46(1)	0.86(1)	3.6(1)	2.2(1)	0.0730(2)
SBN50_T175	0.61(2)	12.5639(1)	3.9737(1)	0.41(1)	0.88(1)	3.7(1)	2.1(1)	0.0739(2)
SBN40_T300	0.60(1)	12.5637(1)	3.9693(1)	0.31(1)	0.77(1)	3.2(1)	2.18(4)	0.0740(1)
SBN40_T225	0.66(2)	12.5655(1)	3.9676(1)	0.37(1)	0.89(1)	3.4(1)	2.0(1)	0.0733(2)
SBN40_T200	0.62(2)	12.5689(1)	3.9590(1)	0.27(1)	0.66(1)	3.5(1)	2.3(1)	0.0745(2)
SBN30_T300	0.44(1)	12.5559(1)	3.9773(1)	0.24(1)	0.61(1)	3.3(1)	2.50(5)	0.0742(1)
SBN30_T225	0.55(1)	12.5583(1)	3.9749(1)	0.29(1)	0.73(1)	3.3(1)	2.4(1)	0.0736(2)
SBN30_T200	0.59(1)	12.5634(1)	3.9649(1)	0.26(1)	0.65(1)	3.4(1)	2.3(1)	0.0742(1)
SBN20_T300	0.78(2)	12.5422(2)	3.9909(1)	0.23(1)	0.57(1)	2.9(1)	2.3(1)	0.0736(2)
SBN20_T225	0.83(3)	12.5533(2)	3.9852(1)	0.24(2)	0.61(2)	3.0(2)	2.3(1)	0.0737(3)
SBN20_T200	0.73(3)	12.5638(2)	3.9826(1)	0.25(2)	0.62(2)	2.8(2)	2.7(1)	0.0743(3)
SBN50_supercrit	0.96(5)	12.5397(3)	3.9718(2)	0.60(2)	0.72(2)	3.1(2)	2.0(1)	0.0723(3)

Table S2 continued:

Sample	y Nb-site2	Biso A1-site [Å²]	Biso A2-site [Å²]	x A1-site	y A1-site	Occ vacancy A1 [a.u.]	R_{wp} [%]	R_{bragg} [%]	Beam time
SBN60_T300	0.2139(2)	0.0(2)	4.3(1)	0.1728(2)	0.6728(2)	0.50(2)	1.29	0.93	Feb
SBN60_T225	0.2132(3)	1.9(3)	4.3(2)	0.1736(4)	0.6736(4)	0.19(4)	1.63	0.83	Feb
SBN60_T200	0.2147(4)	0.8(4)	3.2(2)	0.1725(4)	0.6725(4)	0.16(1)	4.16	2.13	Oct
SBN50_T400	0.2131(2)	1.9(2)	3.8(1)	0.1732(2)	0.6732(2)	0.29(2)	1.63	0.85	Feb
SBN50_T300	0.2135(2)	1.0(2)	4.3(1)	0.1730(2)	0.6730(2)	0.39(2)	1.66	1.09	Feb
SBN50_T225	0.2132(3)	0.7(2)	4.7(1)	0.1720(3)	0.6720(3)	0.35(3)	2.25	1.35	Feb
SBN50_T200	0.2128(2)	1.8(2)	4.3(1)	0.1744(2)	0.6744(2)	0.29(3)	2.14	1.89	Feb
SBN50_T175	0.2126(2)	1.4(2)	3.7(1)	0.1739(2)	0.6739(2)	0.23(2)	1.67	1.23	Feb
SBN40_T300	0.2133(1)	0.9(1)	4.3(1)	0.1731(1)	0.6731(1)	0.45(2)	1.94	1.61	Feb
SBN40_T225	0.2132(2)	2.1(2)	4.4(1)	0.1736(2)	0.6736(2)	0.23(3)	1.90	1.47	Feb
SBN40_T200	0.2144(2)	0.0(2)	4.7(1)	0.1725(2)	0.6725(2)	0.67(2)	3.12	3.05	Oct
SBN30_T300	0.2130(1)	0.0(2)	4.3(1)	0.1729(1)	0.6729(1)	0.79(2)	2.37	2.35	Oct
SBN30_T225	0.2132(2)	1.0(2)	4.3(1)	0.1735(2)	0.6735(2)	0.53(2)	2.43	1.75	Oct
SBN30_T200	0.2134(2)	0.0(2)	4.5(1)	0.1727(1)	0.6727(1)	0.70(2)	4.15	3.31	Oct
SBN20_T300	0.2109(2)	0.0(3)	3.9(1)	0.1734(2)	0.6734(1)	0.85(2)	2.95	1.80	Oct
SBN20_T225	0.2169(3)	0.0(3)	4.3(1)	0.1732(3)	0.6732(3)	0.78(3)	6.74	3.62	Oct
SBN20_T200	0.2130(3)	0.0(3)	4.0(1)	0.1730(3)	0.6730(3)	0.76(3)	5.77	3.63	Oct
3N50_supercrit	0.2092(3)	1.7(4)	2.8(2)	0.1732(3)	0.6732(3)	0.57(4)	4.56	2.95	Feb

Effect of changing the alkaline earth to niobium ratio in the Rietveld refinement

To determine the effect of non-stoichiometry (having the sum of alkaline earth higher or lower than the stoichiometric value of 5) on the Rietveld refinement, the last frame of SBN30_T300 was refined with varying amounts of alkaline earth (4.5 – 5.6). No other changes were done compared to the other refinements explained in the main text.

The results show that the B_{iso} value of the A1-site is 0 (nonphysical) for a total sum of 5 and less, and flattens out at 2.3 Å^2 for values higher than 5.4. Both R-values, R_{wp} and R_{bragg} decrease (which indicates an improved fit to the experimental data) with an increasing amount of Sr plus Ba. These results point towards a higher amount of alkaline earth than the stoichiometric value of 5 for the formed SBN.

Hypothetical charge compensation for an alkaline earth amount > 5 could be oxygen interstitials or free/itinerant electrons. Interstitial oxygen is unlikely, just as for perovskites, since the anion sublattice is close packed. Itinerant electrons have been suggested at the charge compensation in $Sr_{1.2-x}Ba_xNb_2O_6$ (filled SBN, with 6 alkali earth) made by under reducing conditions [4].

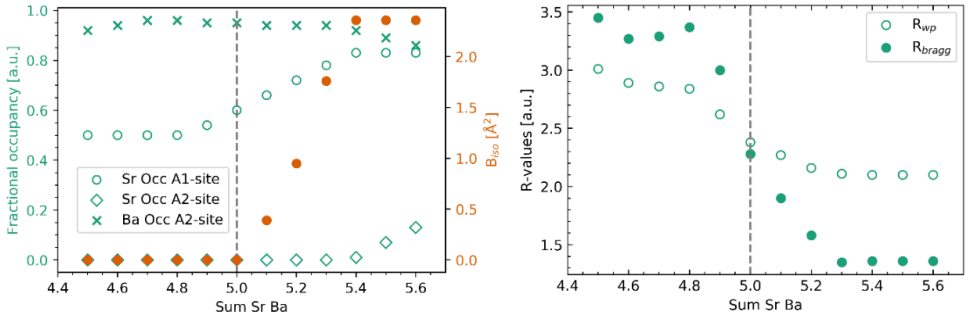

Figure S8: Refined values for Sr occupancy on the A1- and A2-sites, Ba occupancy on the A2-site and B_{iso} value for the A1-site (left) and the corresponding R_{wp} and R_{bragg} values as a function of sum of amount of alkaline earth included in the Rietveld refinement. Grey line indicates the stoichiometric amount for the sum of alkaline earth.

References

1. Carrio, J.G.; Mascarenhas, Y.P.; Yelon, W.; Santos, I.A.; Garcia, D.; Eiras, J.A. Structure Refinement of (Sr,Ba)Nb_2O_6 Ceramic Powder from Neutron and X-Rays Diffraction Data. *Mater. Res.* **2002**, *5*, 57-62.
2. Aamlid, S.S.; Selbach, M.S.; Grande, T. The Effect of Cation Disorder on Ferroelectric Properties of $Sr_xBa_{1-x}Nb_2O_6$ Tungsten Bronzes. *Materials* **2019**, *12*; doi:10.3390/ma12071156.
3. Podlozhenov, S.; Graetsch, H.A.; Schneider, J.; Ulex, M.; Wohlecke, M.; Betzler, K. Structure of strontium barium niobate $Sr_xBa_{1-x}Nb_2O_6$ (SBN) in the composition range 0.32 <= x <= 0.82. *Acta Crystallogr. Sect. B* **2006**, *62*, 960-965; doi:doi:10.1107/S0108768106038869.
4. Kolodiazhnyi, T.; Sakurai, H.; Isobe, M.; Matsushita, Y.; Forbes, S.; Mozharivskyj, Y.; Munsie, T.J.S.; Luke, G.M.; Gurak, M.; Clarke, D.R. Superconductivity and crystal structural origins of the metal-insulator transition in $Ba_{6-x}Sr_xNb_{10}O_{30}$ tetragonal tungsten bronzes. *Phys. Rev. B* **2015**, *92*, 214508; doi:10.1103/PhysRevB.92.214508.

Supplementary Information

Controlled growth of $Sr_xBa_{1-x}Nb_2O_6$ hopper- and cube-shaped nanostructures by hydrothermal synthesis

Ola G. Grendal [1], Inger-Emma Nylund [1], Anders B. Blichfeld [1], Satoshi Tominaka [2], Koji Ohara [3], Sverre M. Selbach [1], Tor Grande [1] and Mari-Ann Einarsrud [1,*]

[1] Department of Materials Science and Engineering, NTNU Norwegian University of Science and Technology, 7491 Trondheim, Norway; ola.g.grendal@ntnu.no (O.G.G.); anders.b.blichfeld@ntnu.no (A.B.B.); selbach@ntnu.no (S.M.S.); grande@ntnu.no (T.G.)

[2] International Center for Materials Nanoarchitectonics (WPI-MANA), National Institute for Materials Science (NIMS), 1-1 Namiki, Tsukuba, Ibaraki 305-0044, Japan; tominaka.satoshi@nims.go.jp (S.T.)

[3] Research and Utilization Division, Japan Synchrotron Radiation Research Institute, 1-1-1 Kouto, Hyogo 679-5198, Japan; ohara@spring8.or.jp (K.O.)

* Correspondence: mari-ann.einarsrud@ntnu.no; Tel.: +47-735-94-002

Comparison between SBN40_T300_1h (*in situ*) and SBN40_T300_in (coil)

The main differences between the coil and *in situ* setup is the heating rate (higher for the *in situ* setup) and the reaction time, which is optimized for each *in situ* experiment to maximize the allocated beam time. Comparing the XRD patterns and SEM images for SBN40_T300 from both the coil (SBN40_T300_1h) and *in situ* (SBN40_T300_in) setups in Figure S1 and S2 respectively, similar results are obtained, at least for similar reaction times, despite the difference in heating rate.

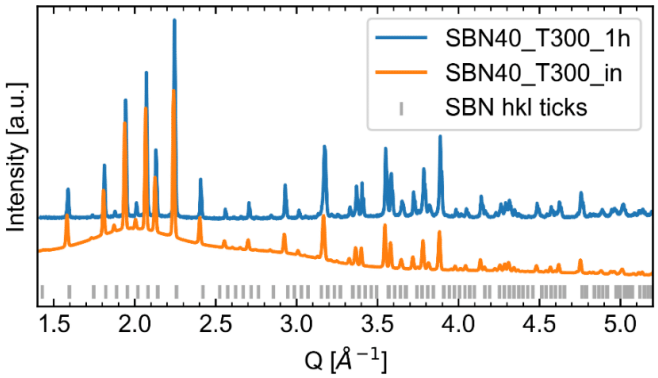

Figure S1: XRD of SBN40_T300_1h and SBN40_T300_0.6h from the coil and *in situ* setup respectively. Both are phase pure SBN. The broad feature observed for SBN40_T300_0.6h is due to scattering from solvent and solutes.

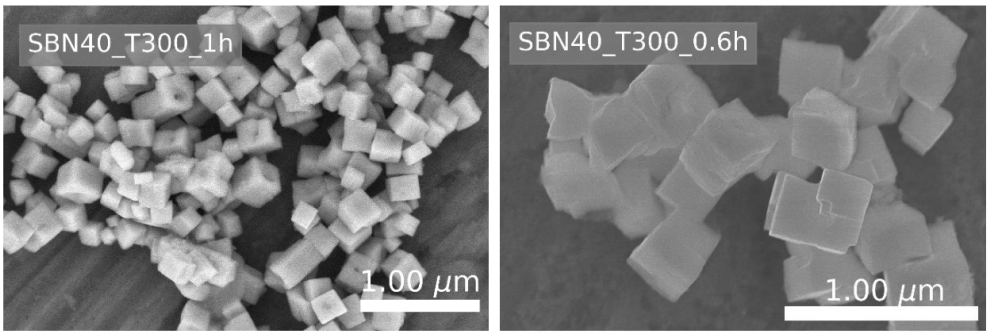

Figure S2: SEM images of SBN40_T300_1h and SBN40_T300_0.6h from the coil and *in situ* setup, respectively. Both setups give cube shaped particles with a cross-sections of ~ 500 x 500 nm^2.

XRD patterns and PDF data for the coil synthesis experiments of SBN

In Figure S3 XRD patterns of the products synthesized using the coil are presented. The XRD patterns show phase pure SBN. For SBN40_T200_1h, the two broad features show the presence of amorphous material because the reaction is not complete after 1 h at 200 °C. The PDF data fitted with a structural model of SBN for all the fully crystalline materials are presented in Figure S4.

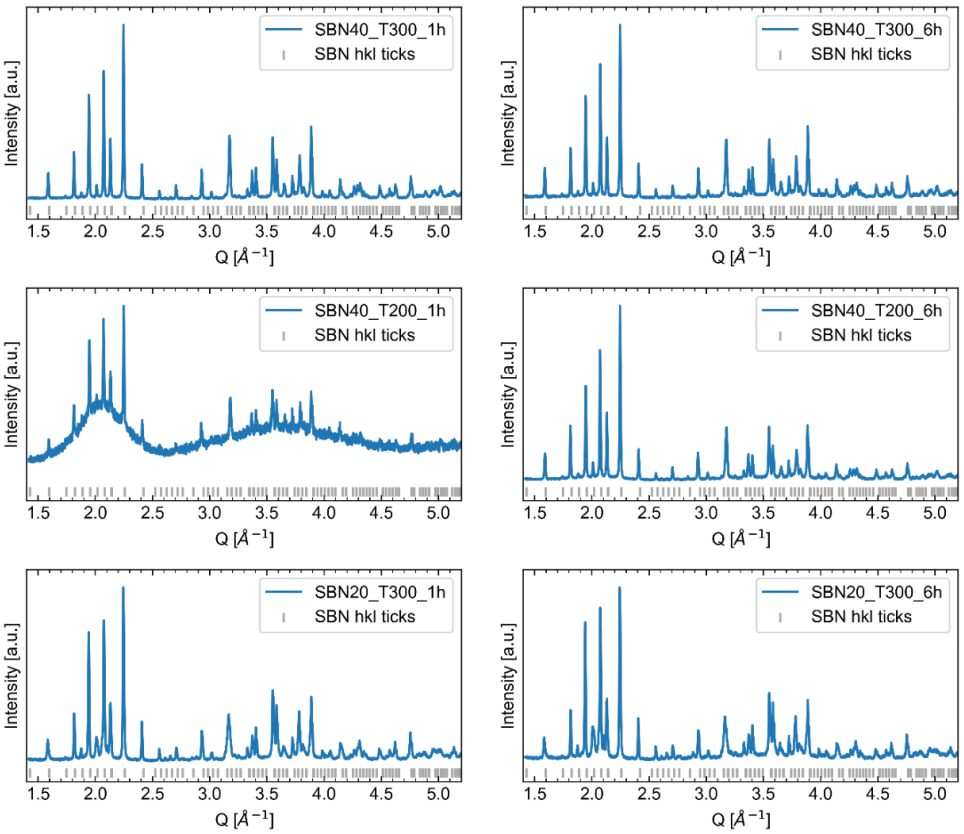

Figure S3: XRD patterns of the products from the coil experiments conducted. All the XRD patterns show phase pure SBN, with SBN40_T200_1h also having two broad features due to amorphous material.

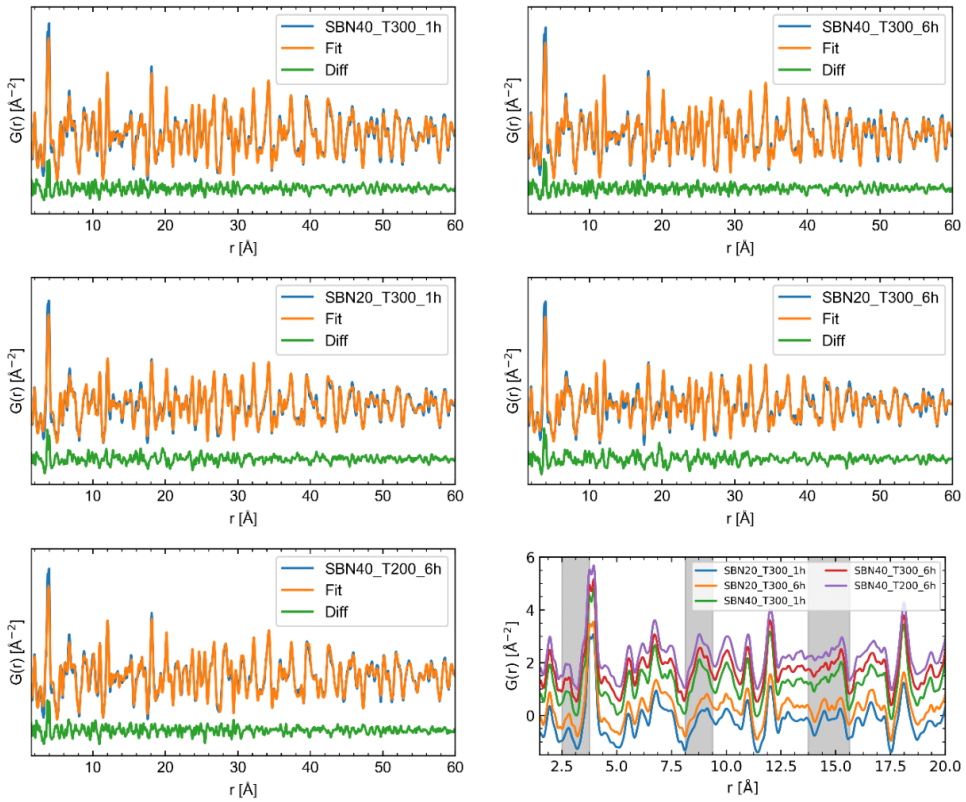

Figure S4: PDF data fitted with a structural model of SBN for the coil syntheses where only crystalline material were formed. Data is plotted in blue, fit to the data in orange and the difference in green. A zoom in on the low r-region (1.5 -20 Å) with gray areas indicting the most prominent differences in the local structure between SBN20 and SBN40 experiments are also presented.

The structural model used for SBN is as described in [1]. The only difference to this work is the use of the non-centrosymmetric (no. 100, P4bm) instead of the centrosymmetric unit cell (no. 127 P4/mbm). For the refinements scale factor, two lattice parameters (a and c in the tetragonal cell), a spherical size parameter, isotropic APD for both niobium and alkaline earth sites (4 in total), Sr fraction, Sr occupancy on the A1-site and three atomic position parameters (in total 14 structural parameters). The three atomic position parameters were the x and y parameter for the B2- and A1-sites, respectively (only one needed for the A1-site due to symmetry constraints). The structure reported by Carrio et al. [2] was used as a starting point, and also locking all non-refined ADP (e.g. oxygen) values to the ones obtained with neutron diffraction. Sr was allowed to occupy both A1- and A2-sites while Ba was locked to the A2-site, all while keeping physical meaningful occupancies (e.g. not negative or higher than 1) and the sum of Sr and Ba equal to 5 for a unit cell.

Bright field (BF) TEM and crystallographic orientation of hollow-ended SBN nanostructures

TEM BF images are presented in Figure S5 and HAADF-STEM and electron diffraction pattern and in Figure S6. Since the two diffraction patterns are taken along two different zone axis, we show that this arises from a relative tilt between the two particles, and not any differences in the crystallographic direction in the particles. Assuming the particle with the [110] zone axis is viewed normal to a facet, we would assume a box-function for the intensity across the particle (bottom schematic in Figure S6 e)), which is what we see in Figure S6 c). Assuming the particle with the [210] zone axis is slightly rotated around its long axis, we would expect an intensity profile as schematically shown at the top of Figure S6 e), which is what we see for the particle in Figure S6 a). From the intensity profile, the angle of tilt can be calculated by combining the following equations when assuming a square cross section, where θ is the tilt angle, and a, b, and c are as shown in Figure S6 f);

$$b = c - 2a * \sin(\theta)$$

$$c = a * \sin(\theta) + a * \cos(\theta)$$

From the values shown in Figure S6 e), θ = 17.6°, which is in good agreement with the theoretical angle of 18.4° between the [110] and [210] direction.

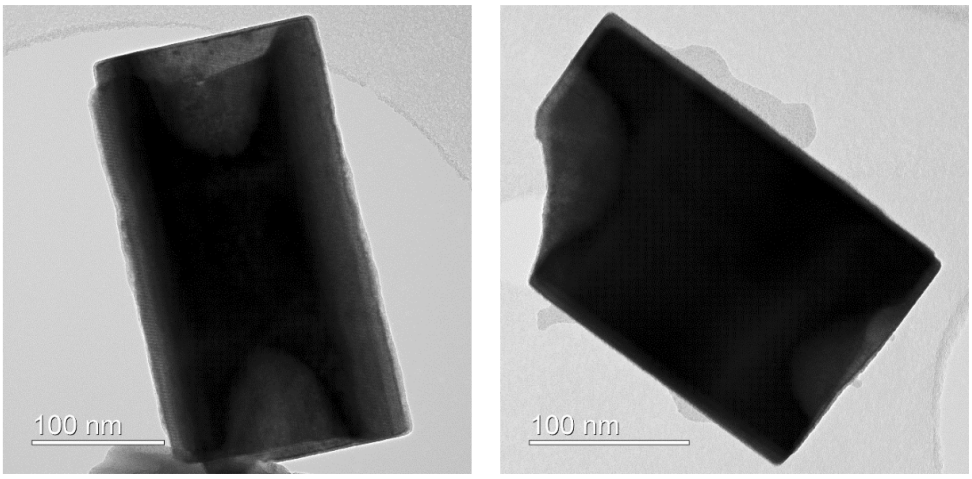

Figure S5: Bright field TEM of the two particles from SBN20_T300_1h characterized with HAADF-STEM and EDS.

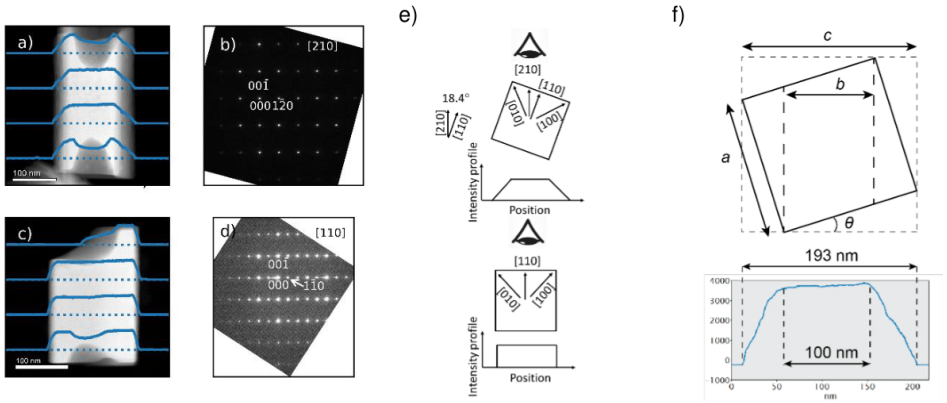

Figure S6: a) and c) HAADF-STEM images of two hollow ended rods from SBN20_T300_1h with blue lines showing the intensity profiles along the blue dashed lines. b) and d) Indexed electron diffraction patterns for the rods are presented in a) and d) respectively. e) Relationship between the [110] and [210]-zone axis, with hypothetical intensity profiles with the [001]-direction pointing into the plane. f) schematic showing how the tilt angle between the two rods were calculated and the determination of values for *b* and *c* from one intensity profile.

References

[1] O. G. Grendal, A. B. Blichfeld, T. D. Vu, W. van Beek, S. M. Selbach, T. Grande, M.-A. Einarsrud, *CrystEngComm* **2019**, *21*, 5922-5930.

[2] J. G. Carrio, Y. P. Mascarenhas, W. Yelon, I. A. Santos, D. Garcia, J. A. Eiras, *Mater. Res* **2002**, *5*, 57-62.